A&A 643, A113 (2020)
https://doi.org/10.1051/0004-6361/202037669

Astronomy & Astrophysics

Observational constraints on the optical and near-infrared emission from the neutron star–black hole binary merger candidate S190814bv⋆

K. Ackley[1], L. Amati[2], C. Barbieri[3,4,5], F. E. Bauer[6,7,8], S. Benetti[9], M. G. Bernardini[3], K. Bhirombhakdi[10], M. T. Botticella[11], M. Branchesi[12,13], E. Brocato[14,15], S. H. Bruun[16], M. Bulla[17], S. Campana[3], E. Cappellaro[9], A. J. Castro-Tirado[18], K. C. Chambers[19], S. Chaty[20,21], T.-W. Chen[22,23], R. Ciolfi[9,24], A. Coleiro[20], C. M. Copperwheat[25], S. Covino[3], R. Cutter[26], F. D'Ammando[27], P. D'Avanzo[3], G. De Cesare[2], V. D'Elia[14,28], M. Della Valle[11], L. Denneau[19], M. De Pasquale[29], V. S. Dhillon[30,31], M. J. Dyer[30], N. Elias-Rosa[9,32], P. A. Evans[33], R. A. J. Eyles-Ferris[33], A. Fiore[9,34], M. Fraser[35], A. S. Fruchter[10], J. P. U. Fynbo[36,37], L. Galbany[38], C. Gall[16], D. K. Galloway[1], F. I. Getman[11], G. Ghirlanda[3], J. H. Gillanders[39], A. Gomboc[40], B. P. Gompertz[26], C. González-Fernández[41], S. González-Gaitán[42], A. Grado[11], G. Greco[43,44], M. Gromadzki[45], P. J. Groot[46,47,48,49], C. P. Gutiérrez[50], T. Heikkilä[51], K. E. Heintz[52], J. Hjorth[16], Y.-D. Hu[18,38], M. E. Huber[19], C. Inserra[53], L. Izzo[16], J. Japelj[54], A. Jerkstrand[22], Z. P. Jin[55], P. G. Jonker[46,56], E. Kankare[51], D. A. Kann[18], M. Kennedy[57], S. Kim[6,58], S. Klose[59], E. C. Kool[22], R. Kotak[51], H. Kuncarayakti[51,60], G. P. Lamb[33], G. Leloudas[61], A. J. Levan[26,46,⋆⋆], F. Longo[62], T. B. Lowe[19], J. D. Lyman[26], E. Magnier[19], K. Maguire[63], E. Maiorano[2], I. Mandel[1,64], M. Mapelli[34], S. Mattila[51], O. R. McBrien[39], A. Melandri[3], M. J. Michałowski[65], B. Milvang-Jensen[36,37], S. Moran[51], L. Nicastro[2], M. Nicholl[64], A. Nicuesa Guelbenzu[59], L. Nuttal[66], S. R. Oates[26,64], P. T. O'Brien[33], F. Onori[67], E. Palazzi[2], B. Patricelli[14,68,69], A. Perego[70], M. A. P. Torres[31,56,71], D. A. Perley[25], E. Pian[2], G. Pignata[7,72], S. Piranomonte[14], S. Poshyachinda[73], A. Possenti[74,75], M. L. Pumo[9,76,77], J. Quirola-Vásquez[6,7], F. Ragosta[11,78,79], G. Ramsay[80], A. Rau[23], A. Rest[10,81], T. M. Reynolds[51], S. S. Rosetti[33], A. Rossi[2], S. Rosswog[22], N. B. Sabha[82], A. Sagués Carracedo[83], O. S. Salafia[3,4], L. Salmon[35], R. Salvaterra[84], S. Savaglio[85], L. Sbordone[86], P. Schady[87], P. Schipani[11], A. S. B. Schultz[19], T. Schweyer[22,23], S. J. Smartt[39], K. W. Smith[39], M. Smith[50], J. Sollerman[22], S. Srivastav[39], E. R. Stanway[26], R. L. C. Starling[33], D. Steeghs[26], G. Stratta[2,44], C. W. Stubbs[88], N. R. Tanvir[33], V. Testa[14], E. Thrane[1], J. L. Tonry[19], M. Turatto[9], K. Ulaczyk[26,45], A. J. van der Horst[89,90], S. D. Vergani[91], N. A. Walton[41], D. Watson[36,37], K. Wiersema[26,33], K. Wiik[51], Ł. Wyrzykowski[45], S. Yang[22], S.-X. Yi[46], and D. R. Young[39]

(Affiliations can be found after the references)

Received 5 February 2020 / Accepted 18 June 2020

ABSTRACT

Context. Gravitational wave (GW) astronomy has rapidly reached maturity, becoming a fundamental observing window for modern astrophysics. The coalescences of a few tens of black hole (BH) binaries have been detected, while the number of events possibly including a neutron star (NS) is still limited to a few. On 2019 August 14, the LIGO and Virgo interferometers detected a high-significance event labelled S190814bv. A preliminary analysis of the GW data suggests that the event was likely due to the merger of a compact binary system formed by a BH and a NS.
Aims. In this paper, we present our extensive search campaign aimed at uncovering the potential optical and near infrared electromagnetic counterpart of S190814bv. We found no convincing electromagnetic counterpart in our data. We therefore use our non-detection to place limits on the properties of the putative outflows that could have been produced by the binary during and after the merger.
Methods. Thanks to the three-detector observation of S190814bv, and given the characteristics of the signal, the LIGO and Virgo Collaborations delivered a relatively narrow localisation in low latency – a 50% (90%) credible area of 5 deg^2 (23 deg^2) – despite the relatively large distance of 267 ± 52 Mpc. ElectromagNetic counterparts of GRAvitational wave sources at the VEry Large Telescope collaboration members carried out an intensive multi-epoch, multi-instrument observational campaign to identify the possible optical and near infrared counterpart of the event. In addition, the ATLAS, GOTO, GRAWITA-VST, Pan-STARRS, and VINROUGE projects also carried out a search on this event. In this paper, we describe the combined observational campaign of these groups.
Results. Our observations allow us to place limits on the presence of any counterpart and discuss the implications for the kilonova (KN), which was possibly generated by this NS–BH merger, and for the strategy of future searches. The typical depth of our wide-field observations, which cover most of the projected sky localisation probability (up to 99.8%, depending on the night and filter considered), is $r \sim 22$ (resp. $K \sim 21$) in the optical (resp. near infrared). We reach deeper limits in a subset of our galaxy-targeted observations, which cover a total ∼50% of the

⋆ Full Table 3 is only available at the CDS via anonymous ftp to cdsarc.u-strasbg.fr (130.79.128.5) or via http://cdsarc.u-strasbg.fr/viz-bin/cat/J/A+A/643/A113

⋆⋆ Corresponding author: A. J. Levan, e-mail: a.levan@astro.ru.nl

galaxy-mass-weighted localisation probability. Altogether, our observations allow us to exclude a KN with large ejecta mass $M \gtrsim 0.1\,M_{\odot}$ to a high (>90%) confidence, and we can exclude much smaller masses in a sub-sample of our observations. This disfavours the tidal disruption of the neutron star during the merger.

Conclusions. Despite the sensitive instruments involved in the campaign, given the distance of S190814bv, we could not reach sufficiently deep limits to constrain a KN comparable in luminosity to AT 2017gfo on a large fraction of the localisation probability. This suggests that future (likely common) events at a few hundred megaparsecs will be detected only by large facilities with both a high sensitivity and large field of view. Galaxy-targeted observations can reach the needed depth over a relevant portion of the localisation probability with a smaller investment of resources, but the number of galaxies to be targeted in order to get a fairly complete coverage is large, even in the case of a localisation as good as that of this event.

Key words. gravitational waves – stars: neutron – supernovae: general

1. Introduction

The discovery of the binary black hole (BH) merger event GW150914 (Abbott et al. 2016) was a major landmark in the history of physics. It was the first detection of gravitational waves (GWs) and the beginning of GW astronomy. The detection of the first confirmed binary neutron star (NS) merger, GW170817 (Abbott et al. 2017a), and the subsequent discovery of its electromagnetic (EM) counterparts – the short GRB 170817A (Abbott et al. 2017b; Goldstein et al. 2017; Savchenko et al. 2017) and the UV, optical, and IR transient AT2017gfo (Coulter et al. 2017a; Lipunov et al. 2017; Tanvir et al. 2017; Soares-Santos et al. 2017; Valenti et al. 2017) – was a second major breakthrough, and marked the beginning of multi-messenger astrophysics with GWs (Abbott et al. 2017c).

The subsequent investigation of GW170817 convincingly linked NS–NS mergers with short duration gamma-ray bursts (e.g. Lyman et al. 2018; Dobie et al. 2018; Mooley et al. 2018; Lazzati et al. 2018; Resmi et al. 2018; Ghirlanda et al. 2019; Lamb et al. 2019a; Margutti et al. 2018; Nynka et al. 2018; Troja et al. 2018a; D'Avanzo et al. 2018) – a link for which the evidence had been accumulating for some time (Fong & Berger 2013; Tanvir et al. 2013; Berger et al. 2013; Jin et al. 2016). In addition, the identification of its host galaxy, NGC 4993 (see Levan et al. 2017), and an assessment of its cosmological recession velocity (Hjorth et al. 2017) permitted the first measurement of a cosmological parameter (the Hubble constant) using the GW distance measurement, thanks to the "standard siren" nature of compact object binaries (Abbott et al. 2017d). The optical and near-infrared (NIR) monitoring campaigns of the transient also unveiled, for the first time, the developing kilonova (KN) emission (Arcavi et al. 2017a; Chornock et al. 2017; Covino et al. 2017; Cowperthwaite et al. 2017; Drout et al. 2017; Evans et al. 2017; Kasliwal et al. 2017; McCully et al. 2017; Nicholl et al. 2017; Pian et al. 2017; Shappee et al. 2017; Smartt et al. 2017; Tanvir et al. 2017) due to the production and decay of r-process elements (e.g. Metzger et al. 2010; Kasen et al. 2017), demonstrating that NS–NS mergers are indeed a major source of these elements (Gall et al. 2017; Watson et al. 2019), as previously suggested (Lattimer et al. 1977; Eichler et al. 1989; Li & Paczyński 1998; Freiburghaus et al. 1999).

Following the success of the GW170817 follow-up campaign, considerable effort has been expended in mounting similar campaigns with the aim of discovering and characterising the counterparts of new GW events. To optimise the science return of the demanding observations of GW counterparts, a large fraction of the GW and EM community in member states of the European Southern Observatory (ESO) has gathered together to form the ElectromagNetic counterparts of GRAvitational wave sources at the VEry Large Telescope (ENGRAVE) consortium[1]. This paper introduces the collaboration and our first major campaign to search for an EM counterpart to a GW source, the NS–BH event merger candidate S190814bv, reported during the O3 run of the LIGO Scientific Collaboration and the Virgo Collaboration (LVC)[2].

S190814bv was detected by the LVC on 2019 Aug 14 21:10:39.01 UT (MJD 58709.88240; The LIGO Scientific Collaboration and the Virgo Collaboration 2019a), and an alert was issued on 2019 Aug 14 21:31:40 UT (MJD 58709.89699), approximately 21 min after the merger. The source was localised to a 50% credible region of 133 deg^2 in the initial report (90% credible region of 772 deg^2), which was reduced to 5 deg^2 at 50% and 23 deg^2 at 90% half a day later (The LIGO Scientific Collaboration and the Virgo Collaboration 2019b) making this the best-localised candidate GW event so far. The source distance (as inferred directly from the GW observations) is 267 ± 52 Mpc. The estimated False-Alarm Rate (FAR) is extremely low, at 2.033×10^{-33} Hz (1 per 1.559×10^{25} years).

Preliminary parameter estimation (Veitch et al. 2015) indicated that the lighter object had a mass $M_2 < 3\,M_{\odot}$, while the heavier object had a mass $M_1 > 5\,M_{\odot}$, making this a NS–BH candidate according to the LVC classification criteria. The same preliminary analysis pointed to a negligible probability of any disrupted material remaining outside the final compact object (given by the parameter `HasRemnant` <1%), implying that in this case an EM counterpart was unlikely. We note that the classification of one of the components as a NS is based solely on the mass being $<3\,M_{\odot}$ and that a low mass BH is not ruled out by such low-latency classification.

No γ-ray, X-ray, or neutrino signal could be connected to the event (Molkov et al. 2019; Kocevksi 2019; Ohno et al. 2019; Pilia et al. 2019a,b; Sugizaki et al. 2019; Palmer et al. 2019; Evans et al. 2019; Cai et al. 2019; Svinkin et al. 2019; IceCube Collaboration 2019; Ageron et al. 2019; Alvarez-Muniz et al. 2019). The relatively small localisation region led to a world-wide follow-up effort with optical and NIR telescopes (e.g. Gomez et al. 2019a; Andreoni et al. 2020; Dobie et al. 2019; Watson et al. 2020; Antier et al. 2020; Vieira et al. 2020). The ENGRAVE collaboration activated its search programmes to try to discover, or set limits on, an EM counterpart to S190814bv. ENGRAVE members ran wide-field searches for EM counterparts and the ATLAS, GOTO, GRAWITA-VST, Pan-STARRS, and VINROUGE projects also triggered their searches on this event. No promising EM counterpart was detected. In this paper we combine our ENGRAVE ESO/Very Large Telescope (VLT) data, a number of other narrow-field facilities, and the wide-field programmes to report the combined results of our search for a counterpart (Sects. 2 and 3). We place limits on the presence of a counterpart (Sect. 3.6), and discuss the implications of these limits for NS–BH mergers and future searches (Sect. 4). Unless otherwise specified, errors are given at 68% confidence level (1σ), upper limits are given at 3σ, and magnitudes are in the AB system. When needed, we assume a flat FLRW cosmology with $H_0 = 70\,\mathrm{km\,s^{-1}\,Mpc^{-1}}$ and $\Omega_\mathrm{m} = 0.3$.

[1] http://www.engrave-eso.org/

[2] https://gracedb.ligo.org/superevents/public/O3/

2. Wide-field survey observations and results

We employed two different approaches to search for an optical or NIR counterpart to S190814bv. A number of wide-field facilities (with Field of View, FoV, of 1 deg^2 or more) were used to tile the LVC GW sky localization probability maps (skymap) with the aim of covering as much of the 2D probability of S190814bv localisation as possible. These telescopes (with apertures of 0.4 m–4 m) were situated in La Palma, Chile and Hawaii, giving a spread of latitude and temporal coverage. The second approach was to target specific galaxies in the 3D sky region with larger aperture (2 m–8 m) telescopes and smaller FoV cameras. In the next subsections we summarise the search for transients with the different facilities.

2.1. The search for transients with GOTO

The Gravitational wave Optical Transient Observer (GOTO[3]) is a robotic array of wide-field optical telescopes sited at the Roque de los Muchachos Observatory in La Palma. It is operated by the University of Warwick on behalf of an international collaboration. The hardware is modular in design and optimised to autonomously respond to GW events, being able to cover large areas of sky quickly. At the time of S190814bv, GOTO was equipped with 4 active unit telescopes, each having an aperture of 40 cm at $f/2.5$ and featuring a 50-megapixel CCD detector. This corresponds to a plate-scale of $1\farcs25\,\mathrm{pix}^{-1}$ and a FoV of 5.9 deg^2 per camera. Observations of the S190814bv error box were automatically scheduled on the basis of a ranked tiling pattern derived from the available skymaps (Dyer et al. 2018; Gompertz et al. 2020a). Each tile was observed using sequences of 60 s or 90 s exposures with the GOTO-*L* filter, which is a wide filter covering 400–700 nm (slightly wider than Sloan g+r combined). The bulk of the final localisation probability, as given by the `LALInference` skymap (`LALInference.v1.fits`), was covered in 8 observable tiles (Fig. 1), with 89.6% probability covered over the timespan MJD = 58710.091–58710.230 (5.09–8.34 h after the GW event). Additional observations were obtained the following night, which covered 94.1%. The Moon was closer to the relevant tiles during this second night, affecting the zeropoints achieved in the exposures sets. Most tiles were observed multiple times (see Table B.2), though observing conditions were not optimal, given the presence of the Moon nearby and poor weather. The probability regions were also close to GOTO's lower declination limit, meaning some of the GW probability region could not be observed. Individual exposures are median combined in groups of 3–6 subsequent images and reached 5σ limiting magnitudes covering $V = 17.4$–19.1 mag. These are derived by photometrically calibrating our photometry to AAVSO Photometric All-Sky Survey (APASS[4]) stars using the V band.

Raw GOTO images are transferred from La Palma to the Warwick data centre in real-time and processing begins minutes after acquisition using the GOTOphoto pipeline (GOTO collaboration, in prep.). Image-level processing includes detector corrections, astrometry tied to *Gaia* and photometric zeropoints using a large number of field stars. Difference imaging was performed on the median exposures using recent survey observations as reference. Source candidates were initially filtered using a trained classifier and cross-matched against a variety of catalogues, including the Minor Planet Center (MPC)[5] and Pan-STARRS1 3π survey (Chambers et al. 2016). The classifier employs a random forest algorithm based on image features, largely following the procedure of Bloom et al. (2012). It was trained using an injected source data-set. Human vetting was performed on the resulting candidates using a web-based marshall interface. No viable optical counterpart candidates could be associated with S190814bv (Ackley et al. 2019).

2.2. The search for transients with the VST

The VLT Survey Telescope (VST; Capaccioli & Schipani 2011) is a 2.6 m facility located at Cerro Paranal, Chile, and managed by ESO. The telescope is equipped with OmegaCam (Kuijken 2011), a 268-megapixel camera with a FoV of 1×1 deg^2 and a resolution of $0\farcs21\,\mathrm{pix}^{-1}$. The filter set includes Sloan *ugriz* filters. The telescope is operated in service mode. The GW trigger follow-up is performed using Guaranteed Time allocated to the Italian VST and OmegaCam Consortium.

The monitoring of the S190814bv sky area started on MJD 58710.36 (Grado et al. 2019a,b; Yang et al. 2019). For each pointing and epoch we obtained three dithered exposures for a total exposure time of 135 s. The pointings were visited up to five times during a period of two weeks (see Table B.2). All exposures were obtained using the r filter.

On the first night we imaged 15 deg^2, covering 53.6% of the localisation probability of the preliminary `BAYESTAR` skymap (which was the only map available at that time), and 60.7% of the final `LALInference` skymap probability. Starting from the second epoch we revised the pointing list to optimise the sky coverage for the updated `LALInference` skymap. The survey area increased to 23 deg^2 covering a maximum of 87.7% of the localisation probability, as shown in Fig. 1.

Details of the image processing and candidate detection are given in Brocato et al. (2018) and Grado et al. (2020). The area identified by the skymap is not fully covered by VST archive observations, hence we used both Pan-STARRS1 (Chambers et al. 2016) and DECam (Abbott et al. 2018a) archive images as templates for the comparison. To select the candidates, we applied a random-forest machine learning algorithm trained on previous search instances (Yang 2018) and then visually inspected the candidates with the highest score. We detected a number of transients from which we removed objects detected only at one epoch and/or associated with stellar sources in the template images. The final list includes 27 transients (reported in Table 2). Out of these, 21 objects were already discovered by other surveys and had been registered on the on the Transient Name Server (TNS)[6]. In Table 2 we include also three transients reported in TNS by other groups that are detected on our images but are below the detection threshold of our search and were therefore not independently detected in our search.

All of these candidates show a slow evolution in the two weeks of the observing campaign ($\Delta m < 1$ mag between the first and last detection). Therefore we tentatively exclude that any of them are associated with the GW event (see Sect. 4.4 and Appendix C for more details on the rejected candidates). The limiting magnitudes of the stacked images were estimated by means of artificial star experiments. The limiting magnitude for each pointing, defined as the magnitude at which 50% of the artificial stars are recovered, is reported in Table B.2. The limits are shallower in the first epoch because of a high background due to full Moon.

[3] https://goto-observatory.org
[4] https://www.aavso.org/apass
[5] https://minorplanetcenter.net/cgi-bin/checkmp.cgi
[6] https://wis-tns.weizmann.ac.il/

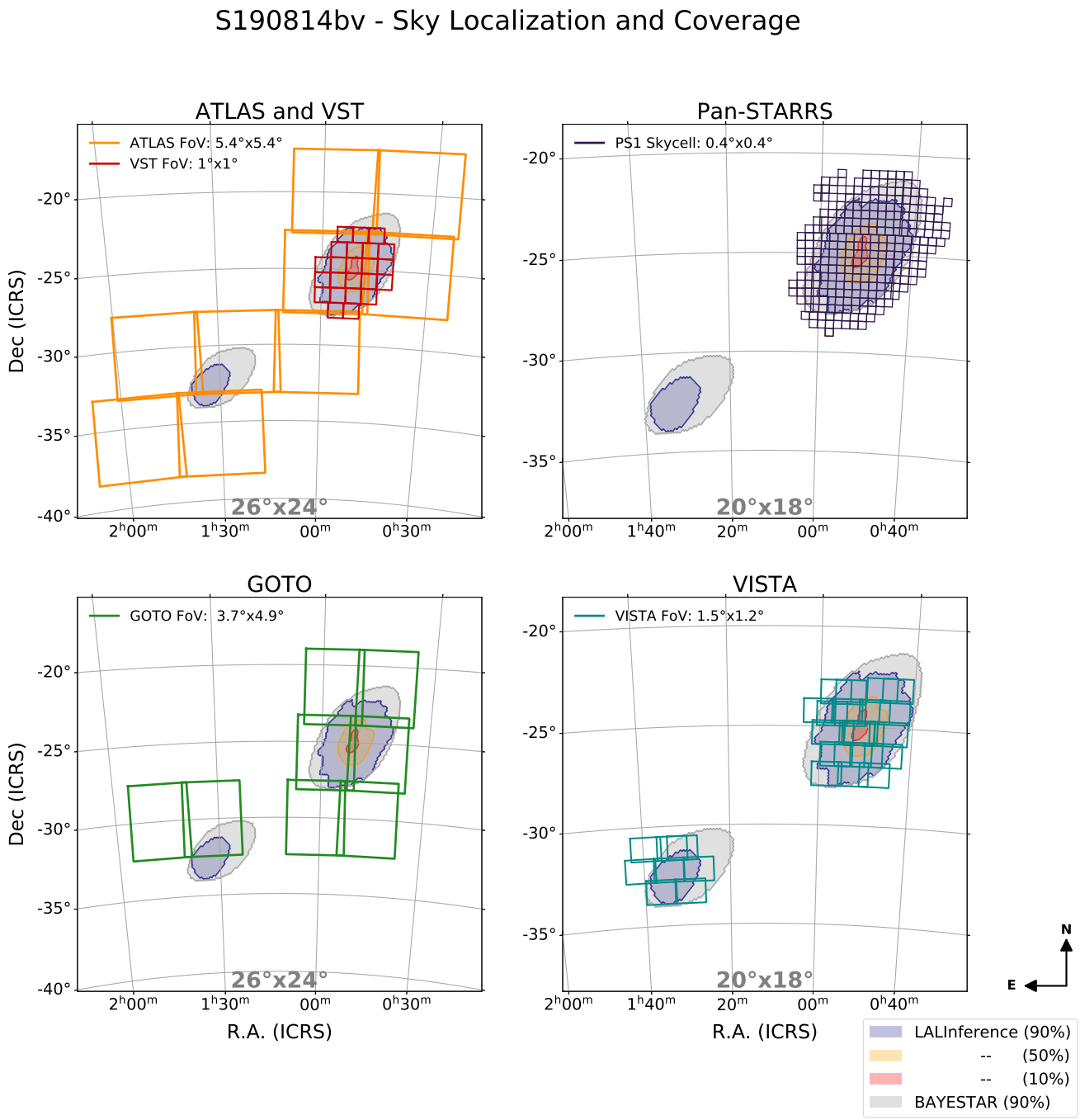

Fig. 1. Coverage maps from the wide-field surveys as listed in Table 1 with the probability contours of the initial skymap (`BAYESTAR`) and the refined skymap `LALInference`.

2.3. The search for transients with VISTA

The 4.1 m Visible and Infrared Survey Telescope for Astronomy (VISTA) is sited at Cerro Paranal and operated by the European Southern Observatory (ESO). The VISTA InfraRed CAMera (VIRCAM) has 16 detectors arranged in a sparse array, and conventionally six pointings are combined with offsets to form a contiguous "tile" of ∼1.6 deg^2 (Sutherland et al. 2015).

Observations were made with VISTA under the VINROUGE programme at three epochs, the first over several nights post-merger (beginning at MJD 58711.17), the second around a week later, and the final epoch roughly seven weeks post-merger which was used as our primary reference template. We only observed in the K_s band (2.15 μm), to optimise our search for a red KN component. A large majority (>90%, see Table 1) of the `LALInference` localisation area (referred to here as "VISTA-wide") was covered at all three epochs, as shown in Fig. 1. The single tile covering the highest likelihood region was re-imaged six times to provide deeper limits in that area (referred to as "VISTA-deep", enclosing ∼21% of the sky localisation probability). Full details of the area covered, timing and representative depth reached are given in Tables 1 and B.2.

Initial processing of the data was performed using a pipeline based on the VISTA Data Flow System (VDFS; González-Fernández et al. 2018) modified for on-the-fly processing. Subsequently, the VINROUGE in-house pipeline for the Identification of GW counterparts through NIR Image

Table 1. Summary of wide-field survey coverage and typical limiting magnitudes.

Telescope	Start MJD	Time after GW	Probability coverage	Limiting mag	Filter
ATLAS	58709.52	−8.7 h	99.8%	18.0	c
GOTO	58710.09	+5.0 h	89.6%	18.7	L
VST	58710.37	+11.5 h	60.7%	20.9	r
Pan-STARRS1	58710.528	+15.50 h	89.4%	20.6, 20.3	$i_{\rm P1}$, $z_{\rm P1}$
ATLAS	58710.60	+17.23 h	99.8%	18.0	o
GOTO	58711.09	+1.2 d	94.1%	18.1	L
VISTA-wide	58711.17	+1.3–3.4 d	94%	21.0	$K_{\rm s}$
VISTA-deep	58711.24	+1.4 d	21%	22.0	$K_{\rm s}$
VST	58711.2	+1.5 d	71.5%	21.9	r
ATLAS	58711.5	+1.6 d	99.8%	17.6	o
Pan-STARRS1	58713.5	+3.6 d	70.4%	21.9	$z_{\rm P1}$
VST	58714.2	+4.3 d	87.7%	21.7	r
Pan-STARRS1	58716.5	+6.6 d	70.7%	23.0	$z_{\rm P1}$
VST	58717.1	+7.2 d	87.7%	21.8	r
VISTA-wide	58719.05	+9.2–10.5 d	94%	21.2	$K_{\rm s}$
VISTA-deep	58720.15	+10.3 d	21%	22.0	$K_{\rm s}$
VST	58724.4	+14.5 d	87.7%	22.0	r
VISTA-wide	58750.1	+40–41 d	94%	21.0	$K_{\rm s}$
VISTA-deep	58751.1	+41 d	21%	22.0	$K_{\rm s}$

Notes. The start MJD refers to the start of observations on that night (for reference, the GW trigger occurred at MJD 58709.882). The given limiting magnitude is the median magnitude of the individual tiles that covered the probability listed. All times are in the observer frame.

Subtraction (`IGNIS`) was used to aid the search for transient sources. Using object lists generated from the VDFS pipeline for both the science and template images, positions were cross-checked to create a list in which the majority of objects visible across multiple epochs were removed, along with objects associated with error flags.

Template and science images were paired based on area coverage, with templates resized to encompass the entire science area per image. Coordinates were aligned through a combination of the `astrometry.net` software `solve-field`, and `SExtractor` (Bertin & Arnouts 1996) and `swarp` to match template image positions directly to their corresponding science images. Template images were then subtracted from science images using the `hotpants` tool[7] (Becker 2015).

We searched for potential counterparts in the subtracted images using two approaches: first by eyeballing the regions around obvious galaxies, particularly those thought to be in the distance range of interest, and secondly through an automated search for sources.

Candidate transients from the automated search were culled based on various criteria, in particular, objects within low confidence regions (e.g. tile edges), with $<5\,\sigma$ detection significance, coincident with foreground stars or the bright cores of galaxies (for which the subtractions often left scars), or unusually sharp images suggestive of hot pixels rather than stellar sources. Moving sources were identified by reference to the MPC. A final check involved human vetting of remaining candidates (typically 1–10 per science image).

This process was repeated for all available science data (including the VISTA-deep field) across the three epochs, cross-matching them over with as many template files as could be attributed to each. Of the sources found in the automated procedure, all were deemed to be image artefacts. Similarly, no convincing new sources were found in the eyeball search, with the exception of the known transient AT2019noq, which was found to have AB magnitudes $K = 20.12 \pm 0.07$ (at MJD 58711.23) and $K = 20.06 \pm 0.07$ (at MJD 58719.25). This source was marginally below the adopted significance threshold in the subtracted image.

[7] http://www.astro.washington.edu/users/becker/v2.0/hotpants.htm

2.4. The search for transients with ATLAS

The Asteroid Terrestrial-impact Last Alert System (ATLAS) is a high cadence, near-Earth asteroid (NEA) survey with two telescopes located on two separate sites in Hawaii (Mauna Loa and Haleakala). The $f/2$ telescopes are 0.5 m aperture with 10.56k × 10.56k pixel CCD cameras (Tonry et al. 2018a). The plate scale is $1\farcs86\,{\rm pix}^{-1}$, giving each camera a FoV of $29.2\,{\rm deg}^2$. Both units scan the sky between $-40° < \delta < +80°$ with a cadence of approximately two days, weather permitting. ATLAS survey mode uses two composite filters – "cyan" and "orange" (c and o, respectively). Cyan covers the Sloan g and r filters and orange covers the Sloan r and i filters.

A typical NEA survey observing cycle is comprised of a sequence of 4 slightly dithered exposures (which we call quads), each lasting 30 s, with overheads and processing requiring an additional 10 s. The 4 exposures are typically separated by 15 minutes within a 1 h period to allow for detection and linking of fast-moving objects. ATLAS frequently adjusts this NEA optimised schedule to carry out similar sequences of quads over the sky area of a GW sky map (e.g. Stalder et al. 2017). Observations are processed by an automatic pipeline to produce de-trended, sky-flattened images. These are corrected astrometrically with respect to the ICRS using *Gaia* stellar positions, and corrected photometrically with respect to a custom built reference catalogue (Refcat2; Tonry et al. 2018b). Difference imaging is employed to identify transients in the survey data and source extraction and measurement are carried out as described in Tonry et al. (2018a). All detections with $S/N \geq 5$ are read into a database at Queen's University Belfast and we require 3 or more detections at $S/N \geq 5$ to form an object detection. After

Table 2. Transients detected with the VST (r-band).

Name	TNS name	RA (hms)	Dec (dms)	MJD	Mag (err)	Note	Tiling
VST J005109.17-221740.7	AT2019qbu	00:51:09.173	−22:17:40.69	58715.16	21.19 ± 0.09	1	T13
VST J004414.33-250744.3	AT2019qby	00:44:14.334	−25:07:44.32	58711.27	21.35 ± 0.02	1	T1
VST J005653.99-275921.4	AT2019qbz	00:56:53.987	−27:59:21.37	58711.30	20.89 ± 0.07	1	T24
VST J004548.54-264939.0	AT2019qca	00:45:48.540	−26:49:39.01	58725.33	21.51 ± 0.05	1	T9
VST J004619.06-260843.2	AT2019qcb	00:46:19.062	−26:08:43.19	58714.24	21.55 ± 0.04	1	T8
VST J005349.82-244549.6	AT2019qcc	00:53:49.820	−24:45:49.58	58725.35	22.14 ± 0.09	1	T21
VST J004656.70-252236.7	AT2019npd	00:46:56.711	−25:22:36.43	58717.22	19.87 ± 0.06	2	T8
VST J004847.88-251823.5	AT2019noq	00:48:47.882	−25:18:23.46	58711.23	19.96 ± 0.03	2	T16
VST J005605.55-243826.4	AT2019nve	00:56:05.510	−24:38:26.40	58710.38	20.53 ± 0.08	2	T21
VST J004659.45-230559.5	AT2019nyv	00:46:59.451	−23:05:59.50	58711.27	21.20 ± 0.09	2	T12
VST J005542.30-244149.9	AT2019nvd	00:55:42.301	−24:41:49.93	58725.35	21.09 ± 0.05	2	T21
VST J005002.82-224118.8	AT2019mwp	00:50:02.820	−22:41:18.78	58711.26	20.57 ± 0.13	2	T13
VST J004804.40-234750.9	AT2019ntm	00:48:04.398	−23:47:50.94	58711.25	21.07 ± 0.11	2	T10
VST J010001.84-264251.3	AT2019ntr	01:00:01.843	−26:42:51.32	58711.29	21.21 ± 0.15	2	T27
VST J005012.07-261152.6	AT2019ntp	00:50:12.072	−26:11:52.56	58711.23	21.04 ± 0.03	2	T16
VST J005305.56-242138.7	AT2019npz	00:53:05.560	−24:21:38.71	58714.25	20.87 ± 0.08	2	T15
VST J004616.81-242221.2	AT2019nxe	00:46:16.814	−24:22:21.19	58714.25	20.87 ± 0.07	2	T7
VST J004320.49-255302.1	SN2019mbq	00:43:20.493	−25:53:02.07	58715.17	18.83 ± 0.04	2	T2
VST J004901.74-231404.9	AT2019nuj	00:49:01.738	−23:14:04.93	58715.16	21.72 ± 0.18	2	T13
VST J004133.33-234432.0	AT2019npe	00:41:33.330	−23:44:31.95	58717.15	21.51 ± 0.07	2	T0
VST J005552.40-254659.8	AT2019npw	00:55:52.399	−25:46:59.81	58711.24	21.34 ± 0.05	2	T23
VST J004330.16-224329.4	AT2019nsm	00:43:30.160	−22:43:29.35	58717.15	21.39 ± 0.09	2	T5
VST J005531.60-225808.5	AT2019num	00:55:31.602	−22:58:08.48	58717.14	21.39 ± 0.09	2	T19
VST J005243.34-233753.6	AT2019nva	00:52:43.339	−23:37:53.64	58717.13	21.36 ± 0.07	2	T14
VST J005646.69-250933.3	AT2019nqw	00:56:46.693	−25:09:33.29	58725.35	20.77 ± 0.03	2	T21
VST J005806.46-245014.3	AT2019nzd	00:58:06.456	−24:50:14.28	58714.23	21.18 ± 0.10	3	T25
VST J005756.90-243400.5	AT2019nys	00:57:56.904	−24:34:00.48	58714.23	21.31 ± 0.10	3	T25
VST J005332.32-234958.5	SN2019npv	00:53:32.316	−23:49:58.50	58717.14	21.62 ± 0.09	3	T20

Notes. 1 – New transient candidates which we first reported in TNS. We verified that AT2019qcb and AT2019qcc are also visible in Pan-STARRS1 subtractions. AT2019qcb (VST J004619.06-260843.2) is detected at z_{P1} = 21.1 ± 0.1 mag, on MJD 58716.53. It is a nuclear transient coincident with a compact galaxy (Kron mag) r_{P1} = 18.68 mag. AT2019qcc (VST J005349.82-244549.6) is detected in two Pan-STARRS1 subtractions at z_{P1} = 21.6 ± 0.2 mag on both MJD 58713.54 and MJD 58716.54 and has a flat light curve in z_{P1}. It is also coincident with a probable compact galaxy r_{P1} = 20.7 (Kron mag). 2 – Independent discoveries already reported in TNS by other groups. 3 – Candidates that are detected on our images but are below the threshold of our search criteria.

such objects are defined, they are subject to various quality filters, machine learning algorithms and cross-matching to known minor planet, star and galaxy catalogues.

ATLAS was serendipitously observing the S190814bv skymap region several hours before the GW detection during its normal survey mode. Hence any recent, young and bright transients would have been identified. Seven pointings of ATLAS covered the entirety of the `LALInference` skymap, and the first pre-discovery observation of the map started at MJD 58709.52 (8.7 h before S190814bv). The coverage continued until MJD 58709.635, or 2.8 h later (Fig. 1). Only the Haleakala telescope observed, in the cyan (c) filter. Some of the earliest exposures were affected by cloud cover and moonlight. No new transient objects which are not cross-matched with stars or known AGN were found in our images. ATLAS re-observed the field on the next two subsequent nights, in the o band (with the Mauna Loa unit). The second night of observations began at MJD 58710.602 (17.26 h after S190814bv) covering 99.8% of the localisation area within a 1 h period. The third night of observations began at MJD 58711.6, again covering 99.8% of the `LALInference` skymap probability. In none of the three post-event epochs did we find any new transients within the GW localisation area of ATLAS.

2.5. The search for transients with Pan-STARRS1

The Pan-STARRS system (Chambers et al. 2016) comprises 2 × 1.8 m telescopes on Haleakala, each with a 1.4-Gigapixel camera mounted at the Cassegrain $f/4.4$ focus of each unit. Here we describe observations with the Pan-STARRS1 telescope (PS1) and the camera GPC1. The GPC1 is composed of sixty Orthogonal Transfer Array devices (OTAs), each of which has a detector area of 4846 × 4868 pixels. The 10 micron pixels (0.″26) give a focal plane of 418.88 mm in diameter or 3.0 degrees. This provides a FoV area of 7.06 deg^2, and an active region of about 5 deg^2 (see Chambers et al. 2016, for a description of the focal plane gaps). The five filter system (generally denoted $grizy_{P1}$) is described in Tonry et al. (2012) and Chambers et al. (2016). For filters in common, the PS1 filters have similar transmission profiles as those from the Sloan Digital Sky Survey (SDSS; Abazajian et al. 2009). Images from Pan-STARRS1 are processed immediately with the Image Processing Pipeline (Magnier et al. 2016; Waters et al. 2016). The existence of the PS1 3π Survey data (Chambers et al. 2016) provides a ready-made template image of the whole sky north of $\delta = -30°$, and we furthermore have proprietary i_{P1} data in a band between $-40° < \delta < -30°$, giving reference sky images in the i_{P1} band down to this lower declination limit. All individual PS1 images have a reference sky subtracted from them

Table 3. All PS1 objects discovered for S190814bv.

PS1 ID	RA J2000	Dec J2000	Classification type	Disc. epoch	Disc. mag	Host	Redshift	IAU ID	Prob. contour
PS19ekf	00:46:57.39	−24:21:42.6	Probable SN	58710.547	19.66 (*i*)	WISEA J004657.40-242142.6	–	AT2019nbp	40
PS19epf	00:48:48.77	−25:18:23.4	Probable SN	58710.585	19.93 (*i*)	WISEA J004847.51-251823.0	–	AT2019noq	20
PS19eph	00:49:51.99	−24:16:17.7	Probable SN	58710.545	19.46 (*i*)	6dFJ0049520−241618	0.435622	AT2019nor	10
PS19epw [(1)]	00:46:56.71	−25:22:36.6	VS in NGC 253	58710.586	20.28 (*i*)	NGC 253	0.0008	AT2019npd	50
PS19epx	00:56:50.42	−24:20:50.0	Probable SN	58710.587	20.66 (*z*)	WISEA J005650.42-242050.3	–	AT2019nqp	80
PS19epz	00:50:26.34	−25:52:57.8	Probable SN	58713.541	21.85 (*z*)	faint, uncatalogued host	–	AT2019nuw	20
PS19eqa	00:50:21.01	−23:42:46.7	Probable SN	58713.541	21.75 (*z*)	WISEA J005021.03-234246.0	–	AT2019nux	50
PS19eqb	00:50:50.39	−25:29:29.5	Probable SN	58713.541	21.01 (*z*)	PSO J012.7099-25.4915	–	AT2019nuy	20
PS19eqc	00:49:52.26	−25:31:25.6	Probable SN	58713.541	21.89 (*z*)	PSO J012.4678-25.5238	–	AT2019nuz	20
PS19eqd	00:52:43.39	−23:37:54.0	Probable SN	58713.541	21.49 (*z*)	PSO J013.1807-23.6317	–	AT2019nva	70
PS19eqe	00:46:51.16	−25:25:39.3	VS in NGC 253	58713.541	21.72 (*z*)	NGC 253	–	AT2019nvb	50
PS19eqf [(2)]	00:52:18.32	−26:19:42.0	SN II	58713.543	21.31 (*z*)	WISEA J005218.36-261942.5	0.070	AT2019nvc	50
PS19eqg	00:55:42.39	−24:41:50.2	Probable SN	58713.541	21.47 (*z*)	PSO J013.9262-24.6973	–	AT2019nvd	60
PS19eqh [(3)]	00:56:05.51	−24:38:26.3	Probable SN	58713.541	21.30 (*z*)	PSO J014.0230-24.6407	–	AT2019nve	60
PS19eqi [(4)]	00:53:32.30	−23:49:58.6	SN Ib	58713.541	21.26 (*z*)	WISEA J005332.35-234955.8	0.056	SN2019npv	70
PS19eqj [(5)]	00:55:52.39	−25:46:59.7	SN IIb	58713.544	21.35 (*z*)	PSO J013.9687-25.7831	0.163	AT2019npw	70
PS19eqk [(6)]	00:56:46.71	−25:09:33.4	Probable SN	58713.542	21.23 (*z*)	PSO J014.1947-25.1593	–	AT2019nqw	80
PS19eqo	00:48:16.08	−25:28:14.9	Probable SN	58713.539	20.89 (*z*)	WISEA J004816.11-252814.8	–	AT2019nvr	40
PS19eqp	00:52:37.75	−26:11:41.4	Probable SN	58713.549	21.44 (*z*)	WISEA J005237.72-261142.4	–	AT2019nvs	50
PS19eqq [(7)]	00:50:12.06	−26:11:52.8	SN Ic-BL	58713.541	21.31 (*z*)	WISEA J005012.11-261154.7	–	AT2019ntp	50
PS19erd	00:55:19.23	−26:11:50.7	Probable SN	58716.542	21.41 (*z*)	WISEA J005519.14-261150.9	–	AT2019ofb	70

Notes. The host galaxies are the primary names as catalogued now in NED. Spectroscopically classified events are noted, and "Probable SN" means the light curve points we have are consistent with it being an unrelated supernova. There are two objects in the nearby galaxy NGC 253, which are certain variable stars in the outskirts of the disc (labelled VS in the table). The final column gives the 2D skymap probability contour within which the transient position lies. Some of the sources are not in the redshift range of the GW event (i.e. 0.046–0.068). A machine-readable file with all photometry for these candidates is available at the CDS. [(1)]Discovered by DECam-Growth: DG19hqpgc. [(2)]Classified by Rodriguez et al. (2019). [(3)]Offset by 3.″8 from galaxy WISEA J005605.37-243830.5, but coincident with faint uncatalogued stellar source. [(4)]Discovered by DECam-Growth: DG19wxnjc. Classified by Gomez et al. (2019b), De et al. (2019a), and Jonker et al. (2019). [(5)]Discovered by DECam-Growth: DG19wgmjc. Classified by Tucker et al. (2019a). [(6)]Discovered by DECam-Growth: DG19xczjc. [(7)]Discovered by DECam-Growth: DG19gcwjc. Classification reported in Wiesner et al. (2019a), but no redshift given.

and sources with at least two detections with $S/N \geq 5$ significance and spatially coincident to within 0.″5 are detected and measured. PS1 typically observes in a quad sequence similar to ATLAS, with a set of 4×45 s exposures taken across a time span of 1 h to identify and link moving sources. The PS1 team can intervene at any moment and direct the telescope to observe a LVC GW sky map with a flexible choice of filter, exposure time, coverage, and dither and stack strategy. The difference images can be combined into deeper stacks or processed individually and the sources resulting from these are read into a large database at Queen's University Belfast. A series of quality control filters, machine learning algorithms and cross-matches against minor planet, stellar and galaxy catalogues are automatically run and human scanning occurs for all objects not coincident with known solar system objects, stars or catalogued AGN (see Smartt et al. 2016a,b, for more details). At the detection time of S190814bv (2019 Aug 14 21:10:39.01), Hawaii was in day time and PS1 began observing the field at 2019 Aug 15 12:40:37 UT, or 15.50 h after the LVC discovery time.

On the first night of observation the individual 45 s exposures (called "warps") were processed individually to search for any fading transient over the 2 h 33 min period of observation. Image sensitivities are estimated by injecting 500 point sources per skycell across a range of magnitudes and the limiting magnitude is defined when 50% of the sources are recovered (described in the content of database table `DiffDetEffMeta` in Flewelling et al. 2016). Each chip exposure is warped onto a pre-defined tesselation (called skycells, see Chambers et al. 2016), and the limits refer to these skycells. The 45 s exposures were combined into a nightly stack on the first three nights of observing. The stacks are made by median combining the warps of each skycell. On the first observing night 25 exposures were combined in $i_{\rm P1}$ and 31 exposures in $z_{\rm P1}$ in each skycell stack, giving a typical exposure time of 1125 s and 1395 s in $i_{\rm P1}$ and $z_{\rm P1}$, respectively. We did not find any fading transient, but the true constraints are weak due to the dither strategy and fill factor.

For the two subsequent nights, we did not process the individual images, rather we combined all the $z_{\rm P1}$ band warps into a nightly stack. The effective exposure times were 12480 s and 13440 s on these respective nights. These were deeper than the 3π reference stacks in $z_{\rm P1}$ in this sky region, so over the next four weeks PS1 observed the region in $z_{\rm P1}$ to make a deeper and more uniform reference stack. The limiting magnitudes of the skycells on the three nights observing of S190814bv were calculated using the new, custom-made deeper reference-stack for template subtraction. The final sky coverage is plotted in Fig. 1.

All images were processed through the Image Processing Pipeline described above. Detections coincident with known stellar objects from the *Gaia* DR1 (Gaia Collaboration 2016), Guide Star Catalogue[8], Two Micron All Sky Survey (2MASS, Skrutskie et al. 2006), SDSS DR12 (Alam et al. 2015) and PS1 (Chambers et al. 2016) catalogues were rejected. Additionally any objects coincident with known AGN were identified and excised from the transient search list. As discussed in Smartt et al. (2016a,b), the AGN identification is based mostly on the Véron-Cetty & Véron (2001) and MILLIQUAS[9] catalogues (Flesch 2015). The resultant objects are spatially cross-matched against known galaxies (mostly through the NASA Extragalactic Database, NED[10]) and all are visually inspected. The objects discovered are listed in Table 3, along with their likely classification (Huber et al. 2019; Srivastas et al. 2019; Smartt et al. 2019a). None of these objects is a viable counterpart of S190814bv (see Sect. 4.4 for details on the candidate rejection).

[8] https://archive.stsci.edu/gsc/
[9] http://quasars.org/milliquas.htm
[10] https://ned.ipac.caltech.edu/

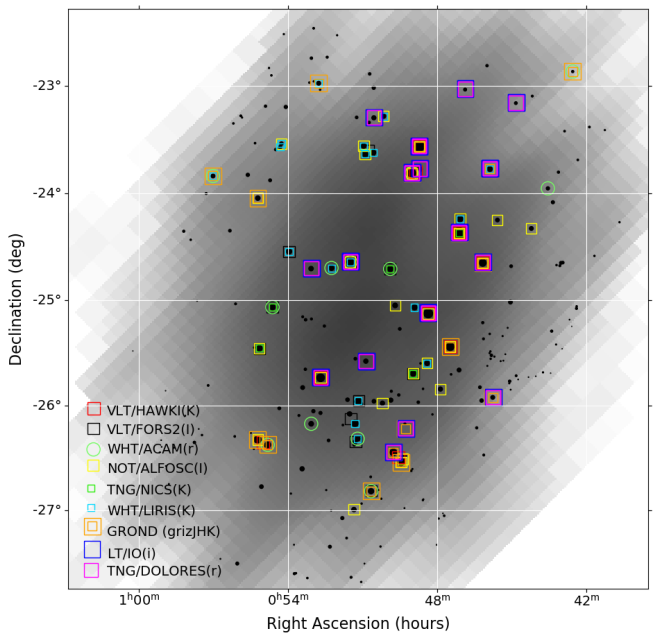

Fig. 2. LVC skymap of S190814bv (`LALInference.v1.fits`) in greyscale, with galaxies selected through `HOGWARTS` over-plotted (black dots). Only the higher probability Northern region of the skymap is included, since the Southern region was not followed up by ENGRAVE. The size of the symbol of each galaxy (i.e. the black dots) is proportional to the probability of hosting the GW event (see Table B.1) given the skymap and a weighing scheme following Arcavi et al. (2017a). The various instruments are illustrated with different colours as in the figure legend, and the typical limiting magnitudes and filters used are given in Table B.1.

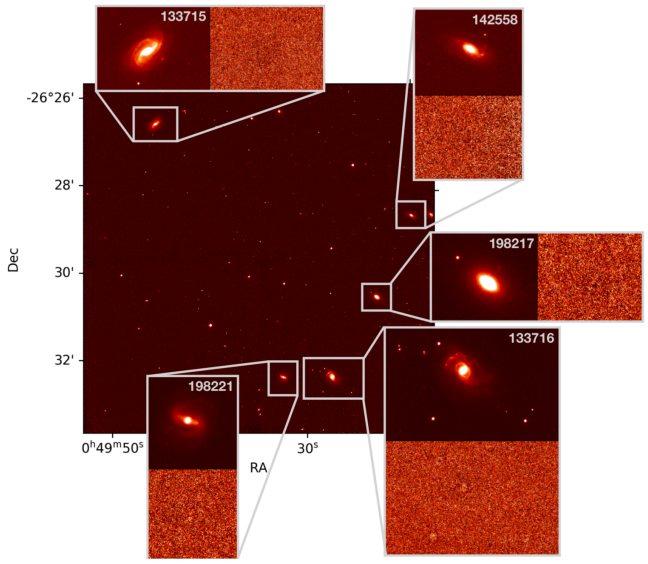

Fig. 3. VLT/HAWK-I image of a galaxy targeted field. A number of catalogued galaxies (and at least one uncatalogued galaxy likely at the same redshift) are visible in the field. The insets show each individual galaxy as well as the resulting subtraction, demonstrating the absence of variable sources to the limits of the data in any of these possible host galaxies. Each galaxy inset is labelled by the HyperLEDA identifier from the GLADE catalogue, and the corresponding limiting magnitudes are listed in Table B.1.

3. Galaxy targeted searches

In addition to the wide-field survey coverage, the unusually tight localisation map of S190814bv (5 deg^2 at 50%), and the distance estimate available from the GW signal (267 ± 52 Mpc), allowed us to define a coordinated programme of multi-wavelength observations of galaxies within the localisation region (e.g. Nissanke et al. 2013; Evans et al. 2016a; Gehrels et al. 2016). While these images cannot cover the whole 2D skymap, they can (often) significantly improve upon the depth of the wide-field surveys for a select number of high-luminosity galaxies (Fig. 2). To identify galaxies with the highest probability of hosting the GW event we utilised the `HOGWARTS` code[11] (Salmon et al. 2020), which ranks galaxies in the Galaxy List for the Advanced Detector Era (GLADE; Dálya et al. 2018) catalogue according to their probability of containing the corresponding merger given the 3D localization probability density (Singer et al. 2016), and based on the expectation that NS–BH merger rates follow the galaxy mass distribution (Arcavi et al. 2017a).

Since the expected colours and luminosities of the counterparts of NS–BH mergers (see Sect. 4.1) still have significant uncertainties (largely due to the lack of observational constraints), our goal was to obtain multi-colour (optical and NIR) imaging, which we prioritised over observing a greater number of galaxies. This strategy enabled our observations to be sensitive to counterparts that were either blue (e.g. disc-wind driven), or very red due to high lanthanide opacities in dynamical ejecta. While our observations targeted the most luminous galaxies weighted for the localization probability, individual telescope pointings were refined in order to capture additional (lower luminosity) galaxies within the localisation volume of the `LALInference` skymap. We obtained a series of coordinated observations using the Gamma-Ray burst Optical and Near-IR Detector (GROND), the Liverpool Telescope (LT), the Nordic Optical Telescope (NOT), the Telescopio Nazionale *Galileo* (TNG), the Very Large Telescope (VLT) and the *William Herschel* Telescope (WHT). In total, over 400 multi-wavelength (*grizJHK*) images of the 67 most probable galaxies within the 3D volume were obtained in the ten days following the merger. When generating target lists for each telescope, we attempted to avoid unnecessary duplication of observations, while ensuring that the highest probability galaxies were observed to the greatest possible depth. In practice weather, seeing and other scheduling constraints meant that some duplication was unavoidable. Our global coverage is shown in Fig. 2 and a list of observed galaxies in order of decreasing probability (as defined in Sect. 3.7) is given in Table B.1. An example set of observations with the VLT High Acuity Wide field K_s band Imager (HAWK-I; Pirard et al. 2004; Casali et al. 2006; Kissler-Patig et al. 2008; Siebenmorgen et al. 2011) is shown in Fig. 3.

Our techniques for searching for transient objects depended on the nature of the data available. All images obtained were manually, and rapidly, compared against existing optical survey data, in particular the PS1 3π survey (e.g. as was done in Coulter et al. 2017b, when AT2017gfo was first discovered). Given the brightness and proximity of the Moon at the time of the observations, only the VLT data exceeded the depth of the PS1 3π survey. For some observations these data remained the best comparison.

In most other cases, when reference images were subsequently obtained, we performed PSF-matched image subtraction using the `hotpants` code. The residual images were then manually inspected to identify any possible transient sources. We

[11] https://gwtool.watchertelescope.ie/

limited our search to the circle centreed on the nucleus of the investigated galaxy, with radius $1.5\times R_{25}$, where R_{25} is the galaxy isophotal radius at $B = 25$ mag arcsec^{-2}[12]. In general, all galaxies are well subtracted except for some of the brighter nuclei that leave notable residuals and prevent the search for transients. We confirmed that no transients are identified in the difference images. To quantify the depth of these images we inserted artificial stars into the images in different positions within the galaxy search radius with a range of magnitudes and estimated their recovery in our difference images. The limiting magnitude is defined as the average magnitude of the faintest artificial stars that can be visually identified, where optical and NIR photometry is calibrated against the PS1 and 2MASS catalogues, respectively. In all cases these stars had $S/N \sim 3$. We found that the limiting magnitude is fairly constant at different positions within the galaxy search radius with the exception of the nuclei.

3.1. VLT observations

The Very Large Telescope (VLT) is a facility operated by ESO on Cerro Paranal in the Atacama Desert of northern Chile (Arsenault et al. 2006), which consists of four individual 8.2 m telescopes (UT1–4). We obtained observations of 16 high-priority galaxies with the VLT using i and z imaging with the FOcal Reducer and low dispersion Spectrograph (FORS – Appenzeller et al. 1998, mounted at UT1), and NIR imaging for further 17 galaxies with HAWK-I (Kissler-Patig et al. 2008, mounted at UT4; see Fig. 3 for an example image) in the K_s band (see Table B.1). All VLT data were reduced using the standard EsoReflex graphical environment (v2.9.1; Freudling et al. 2013). The observations were performed in one epoch of FORS imaging on 2019 Aug 16 and three epochs of HAWK-I imaging on 2019 Aug 16, 22–23 and 2019 Sept 23–24. Given the likely slow rise time of KNe in the NIR bands, the first two HAWK-I K_s-band epochs were intended to be sensitive to the peak of the KN a few days after merger time. This complemented the FORS optical imaging within the first 24–48 h, which is more sensitive to early emission.

FORS observations consisted of 3×100 s observations in the i band, although one field was erroneously observed in the z band for the same exposure time. These images reached significantly deeper limiting magnitudes ($i \sim 23$–24.5 mag) across the field than those obtained by smaller aperture telescope searches. The cores of some galaxies were, on occasion, saturated, removing our ability to detect transients close to the nucleus.

3.2. WHT observations

A series of optical and NIR observations of 17 galaxies in the sample were taken with the *William Herschel* Telescope (WHT, Boksenberg 1985) from 2019 Aug 14–22. Optical observations of 17 galaxies were obtained in the r band using the Auxiliary-port CAMera (ACAM, Benn et al. 2008) instrument on 2019 Aug 15, while NIR observations of 12 galaxies were taken in the K_s band using the Long-slit Intermediate Resolution Infrared Spectrograph (LIRIS, Acosta-Pulido et al. 2002) over the following nights. Both the LIRIS and ACAM images were reduced using standard `IRAF` procedures[13] and the custom LIRIS package for LIRIS[14].

3.3. TNG observations

Optical and NIR images of a subset of 19 galaxies were carried out with the Italian 3.6 m Telescopio Nazionale *Galileo* (TNG, Poretti 2018), situated on La Palma, using the optical DOLoRes (Molinari et al. 1999) and near-infrared NICS (Oliva et al. 2001) instruments. Ten galaxies were observed in the r band with relatively short (120 s) exposures obtained on 2019 Aug 15 between 02:13 and 02:54 UT (D'Avanzo et al. 2019a). Image reduction was carried out using standard `IRAF` procedures. Astrometry was performed using the USNO–B1.0[15] catalogue. The typical upper limit is $r \sim 22.8$ (3σ detection limit).

NIR observations of five galaxies were undertaken on 2019 Aug 16, Aug 20 and Sept 5 (usually between 03:00 and 05:00 UT). In addition, the galaxy ESO474-026 was observed on 2019 Aug 17. Each galaxy was observed for 1200 s total exposure time with the K_s filter (D'Avanzo et al. 2019b). Image reduction was carried out using the *jitter* task of the `ESO-eclipse` package[16]. Astrometry and photometric zeropoints were calculated using the 2MASS[17] catalogue. The typical upper limit is $K_s \sim 19.7 - 20.9$ (3σ detection limit).

3.4. GROND observations

We observed 36 galaxies simultaneously in $g', r', i', z', J, H, K_s$ with GROND (Greiner et al. 2008), mounted at the 2.2 m MPG telescope at the ESO La Silla Observatory. For each galaxy we obtained an average exposure of 2.1 min in the optical bands and 3.9 min in the NIR bands, and the data were reduced using the GROND pipeline (Krühler et al. 2008), which applies bias and flat-field corrections, stacks images and provides an astrometric calibration. The observations reached typical 3σ detection limits of 20−22 mag in the r' band and 17.5−19.5 mag in K_s.

3.5. LT observations

The Liverpool Telescope (LT; Steele et al. 2004) is a 2 m fully robotic telescope on the Canary island of La Palma, Spain. A total of 19 galaxies were observed using the IO:O imaging camera. IO:O has a 10×10 arcmin^2 FoV and was operated with a 2×2 binning, providing a pixel scale of $0\farcs3$ pix^{-1}. The observations were made between 01:38 and 05:34 UT on 2019 Aug 15. For all fields, 2×150 s exposures in r band were obtained, and for some of the highest-probability candidates we also obtained 2×150 s exposures in i band. Reduced images were provided by the IO:O pipeline and stacked with SWarp[18]. Image subtraction of these data were performed using our own subtraction tools rather than `hotpants`, and detection limits were measured performing PSF photometry at fixed positions over a grid around the centre of each image to determine the median and standard deviation of the sky background as measured in each aperture. Using these measurements, with the calibration tied to the PS1 photometric standards in each field, we derived 3σ limiting magnitudes of 20.3 in both bands.

3.6. Galaxy catalogue incompleteness

While searches for EM counterparts targeting known galaxies within the localisation region of a GW are eminently feasible for

[12] http://leda.univ-lyon1.fr/
[13] https://iraf-community.github.io
[14] http://www.ing.iac.es/Astronomy/instruments/liris/liris_ql.html
[15] https://www.usno.navy.mil/USNO/astrometry/optical-IR-prod/icas/fchpix
[16] https://www.eso.org/sci/software/eclipse/
[17] https://irsa.ipac.caltech.edu/Missions/2mass.html
[18] https://www.astromatic.net/software/swarp

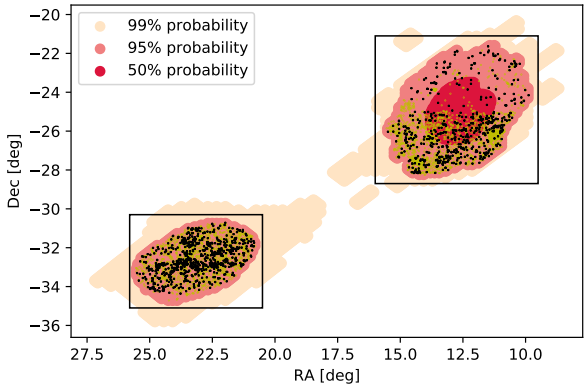

Fig. 4. 50, 95, and 99% probability regions for S190814bv. Boxes indicate the northern and southern regions of the map as discussed in the text. Galaxies which have a spectroscopic redshift in NED, and lie within the 95% contour at a distance $\pm 3\sigma$ that of S190814bv are marked in black; galaxies with an inconsistent spectroscopic redshift are plotted in yellow. The inhomogeneous coverage of NED in the northern contour is clearly visible.

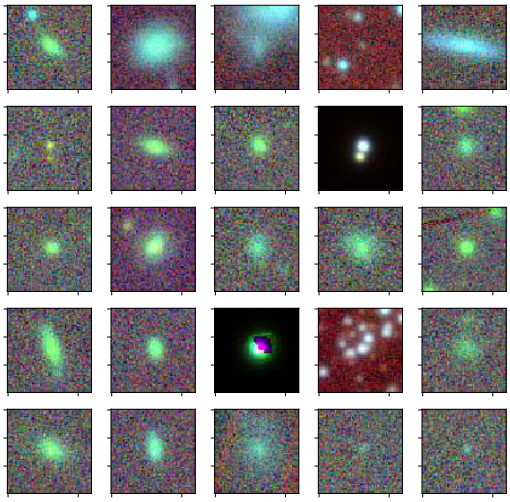

Fig. 5. Example $15'' \times 15''$ Pan-STARRS *gri* cutouts around extended sources identified by our cuts.

nearby events, such an approach becomes less effective as distance increases. There are two reasons for this: firstly, the density of galaxies per unit area on the sky increases such that tiling the GW map becomes more efficient; secondly, the completeness of galaxy catalogues drops off precipitously beyond 200−300 Mpc. Nonetheless, for S190814bv we used targeted deep optical and NIR observations of some of the most likely host galaxies in the probability map as reported by the `HOGWARTS` ranking tool. We thus needed to determine the completeness of the galaxy catalogues that `HOGWARTS` used for the position and distance of S190814bv.

To assess the completeness of GLADE, we queried NED for any galaxies within the 95% probability region of the `LALInference` skymap, and with a listed spectroscopic redshift. This resulted in 5209 galaxies, of which 1376 have a spectroscopic redshift within 3σ of the S190814bv distance luminosity marginalised over the whole sky (267 ± 52 Mpc). We plot the positions of these galaxies in Fig. 4. What is apparent from Fig. 4 is that the completeness of the NED database varies across the map, with a sharp drop in the number of galaxies above Dec = −25°. This is almost certainly due to the lack of coverage of the 2dF galaxy redshift survey above Dec = −25° (Colless et al. 2001).

We attempt to quantify this varying incompleteness in NED in order to determine what fraction of stellar luminosity and mass we have covered in the galaxy targeted search. To this end, we selected galaxy candidates from the PS1 3π catalogue, as this is the deepest, most homogeneous public imaging catalogue available over the whole skymap. PS1 reaches a limiting magnitude of 98% completeness for point sources of 22.5–23 mag in each of $g_{\rm P1}$, $r_{\rm P1}$, $i_{\rm P1}$, with extended source completeness being about 0.5 mag brighter (Chambers et al. 2016). For reference, an apparent magnitude limit of ∼22 mag corresponds to an absolute magnitude ∼−15.1 mag at a distance of 267 Mpc. This absolute magnitude is comparable to that of the Small Magellanic Cloud, and so at the distance of S190814bv PS1 is essentially complete to all galaxies of relevance. While we may miss some very low surface brightness dwarf galaxies, these contain so little stellar mass that they can be ignored for our purposes (see Sect. 3.7 for a discussion of this).

To create our galaxy candidate catalogue for S190814bv, we queried the PS1 database (Flewelling et al. 2016) for all sources within the northern 95% localisation region. In order to select only extended objects, we require that $g_{\rm PSF} - g_{\rm Kron} > 0.1$ mag, and $r_{\rm PSF} - r_{\rm Kron} > 0.1$ mag, and in addition that the source has $n_{\rm detections} > 10$ within the PS1 catalogue. Finally, we limit ourselves to the brightest galaxies in the field, setting a threshold of $r_{\rm Kron} < 20$ mag, which is equivalent to an absolute magnitude of ∼−17 mag at the distance of S190814bv. We also mask out regions in our catalogue around the Sculptor Galaxy NGC 253 and globular cluster NGC 288, which both contain a large number of spurious detections in the PS1 catalogue.

Visual inspection of a random sample of sources from our extended source catalogue confirms that the majority (≳90%) are indeed galaxies (Fig. 5). The small number of sources brighter than $r = 14$ mag in the catalogue all appear to be saturated, bright stars rather than galaxies, so we impose a brightness cut-off at $r = 14$ mag. We are finally left with 23 466 candidate galaxies within the northern 95% localisation probability region of S190814bv. In order to better assess the issue of completeness, we cross-matched our PS1 galaxy catalogue against the NED and GLADE galaxy lists, requiring a matching radius of $<1\farcs5$. We show the fraction of galaxies that have an associated NED or GLADE counterpart in Fig. 6. The GLADE completeness reaches a maximum of ∼80% for galaxies brighter than $r \sim 16.5$ mag, but drops rapidly at fainter magnitudes, with a completeness of only ∼50% at $r = 17.5$ mag, and ≲20% for $r < 18$ mag; the NED completeness is substantially lower between $r \sim 15.5$–17.5 mag.

The completeness of galaxy catalogues in the context of gravitational wave searches was also recently considered by Kulkarni et al. (2018). These authors employed a different approach to this work, by using nearby supernovae with known distances to generate a random sample of galaxies. From this, Kulkarni et al. then determine the fraction with extant spectroscopic redshifts. While Kulkarni et al. look at a somewhat closer distance (<200 Mpc), it is nonetheless encouraging that their "Relative Completeness Fraction" of 75% (which is implicitly weighted by host mass), is comparable to our completeness for the most luminous galaxies.

3.7. Probability covered by our targeted search

As demonstrated in the previous section, while the GLADE catalogue is somewhat incomplete in terms of galaxy number in

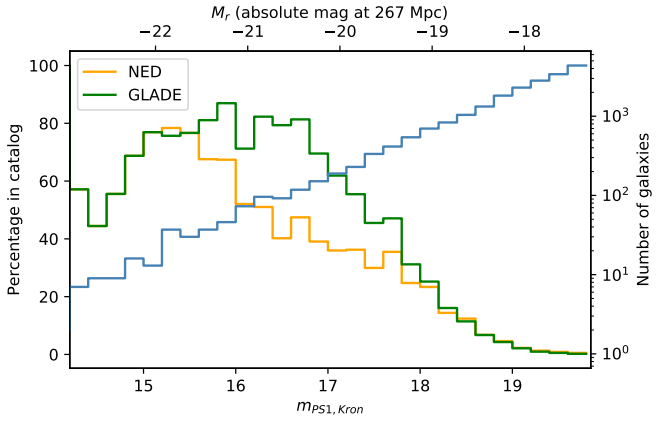

Fig. 6. Orange and green lines, left axis: percentage of sources in the PS1 catalogue that have an associated NED and GLADE, respectively, cross-matched galaxy with spectroscopic redshift as a function of magnitude. Blue line, right axis: histogram of galaxy counts as a function of magnitude, from our Pan-STARRS-derived extended source catalogue.

the localisation volume, it contains the majority of the most luminous (and hence most massive) galaxies. In order to quantitatively estimate the efficiency of our galaxy-targeted search, in terms of covering the GW localisation probability, we proceed here to assign a definite probability of being the actual host of S190814bv to all catalogued galaxies in the volume, accounting for the mentioned incompleteness. The full list of targeted galaxies and the corresponding observations are reported in Table B.1. Let us consider galaxies as point-like objects, and let i be an index that runs on all galaxies that are located within the volume V_α that contains a given fraction α of the GW 3D posterior localisation probability density $P_{\rm 3D}({\rm RA}, {\rm Dec}, d_{\rm L})$ (i.e. the 3D skymap). We assume the probability $P_{{\rm gal},i}$ that the merger has taken place within galaxy i to be proportional to the product between $P_{\rm 3D}(\mathbf{x_i})$, namely the GW localisation probability density per unit volume at the galaxy position $\mathbf{x}_i = ({\rm RA}_i, {\rm Dec}_i, d_{{\rm L},i})$, and $R_{{\rm NS-BH},i}$, that is the NS–BH merger rate in galaxy i (which in principle depends on its present properties and on its history). Artale et al. (2019) have shown, combining state-of-the art compact binary population synthesis models and cosmological simulations, that the NS–BH rate in galaxies at low redshift correlates almost linearly with the galaxy total stellar mass ($R_{\rm NS-BH} \propto M^{0.8}$), with some scatter driven by differences in galaxy merger histories, specific star formation rate and metallicity evolution. Based on these results, for simplicity we assume $R_{{\rm NS-BH},i} \propto M_i$ and we use the galaxy $K_{\rm s}$-band luminosity L_K as a proxy for galaxy mass, so that $R_{{\rm NS-BH},i} \propto L_{K,i}$. This leads to

$$P_{{\rm gal},i} = A\, P_{\rm 3D}(\mathbf{x}_i)\, L_{K,i}, \tag{1}$$

which is similar to the galaxy ranking score used by Arcavi et al. (2017b), but with B-band replaced by $K_{\rm s}$-band luminosity (which is a better tracer of galaxy mass). In order to compute the normalisation constant A, we impose the condition

$$\alpha = \sum_{i=1}^{N} P_{{\rm gal},i} = A \sum_{i=1}^{N} P_{\rm 3D}(\mathbf{x}_i)\, L_{K,i},, \tag{2}$$

where N is the total number of galaxies in the volume V_α (equality (2) is strictly valid only when $\alpha = 1$, but in practice it remains correct to an excellent approximation for α close to one). Since our catalogue only contains a fraction of the actual galaxies in the volume, we need to split the sum on the RHS of Eq. (2) into two terms

$$\sum_{i=1}^{N} P_{\rm 3D}(\mathbf{x}_i)\, L_{K,i} = \sum_{i=1}^{N_{\rm cat}} P_{\rm 3D}(\mathbf{x}_i)\, L_{K,i} + \sum_{i=N_{\rm cat}+1}^{N} P_{\rm 3D}(\mathbf{x}_i)\, L_{K,i}, \tag{3}$$

where $N_{\rm cat}$ is the number of GLADE galaxies within V_α. Assuming the remaining $K_{\rm s}$-band luminosity (present in the volume, but missing from the catalogue) to be uniformly distributed within the volume, we can approximate the last term as

$$\sum_{i=N_{\rm cat}+1}^{N} P_{\rm 3D}(\mathbf{x}_i)\, L_{K,i} \sim \langle P_{\rm 3D}\rangle_{V_\alpha}\, (L_{\rm TOT} - L_{\rm cat}), \tag{4}$$

where $L_{\rm cat}$ is the total $K_{\rm s}$-band luminosity in GLADE galaxies, $L_{\rm TOT}$ is the total $K_{\rm s}$-band luminosity in the localisation volume, and $\langle P_{\rm 3D}\rangle_{V_\alpha}$ is the GW 3D localisation probability density averaged over the volume, that is $\langle P_{\rm 3D}\rangle_{V_\alpha} = \alpha/|V_\alpha|$, where $|V_\alpha|$ is the extent of the localisation volume (e.g. in comoving Mpc^3).

This finally gives the normalisation constant as

$$A = \frac{\alpha}{\sum_{i=1}^{N_{\rm cat}} P_{\rm 3D}(\mathbf{x}_i)\, L_{K,i} + \alpha(L_{\rm TOT} - L_{\rm cat})/|V_\alpha|}. \tag{5}$$

The total $K_{\rm s}$-band luminosity in the localisation volume can be estimated as $L_{\rm TOT} \sim |V_\alpha| \times j$, where $j \sim (7\pm1.5)\times10^8\, L_\odot\, h\,{\rm Mpc}^{-3}$ is the $K_{\rm s}$-band local luminosity density (Hill et al. 2010).

In order to construct the volume that contains 95% of the localisation probability from the latest public 3D GW localisation probability density based on GW parameter estimation (the `LALInference` skymap; The LIGO Scientific Collaboration and the Virgo Collaboration 2019b), we employ a 3D greedy binning approach. The 3D bins are defined by dividing the sky into tiles using a healpix grid (with $N_{\rm side} = 1024$), and further dividing the distance coordinate into 3000 linearly-spaced bins between 0 and 700 Mpc. The probability contained in each bin is assigned based on the 3D skymap (following Singer et al. 2016). The bins are then summed in order of decreasing probability density until the enclosed probability equals 95%, which defines the desired localisation volume. The extent of the obtained volume is $|V_{95\%}| \approx 1.4\times10^5\,{\rm Mpc}^3$, which gives $L_{\rm TOT} \sim (6.9\pm1.5)\times10^{13}\, L_\odot$. 1061 GLADE galaxies fall within this volume. Only 45% of these have a $K_{\rm s}$-band measurement reported in the catalogue, due to the 2MASS magnitude limit. To circumvent this problem we utilise our own VINROUGE observations to obtain $K_{\rm s}$-band magnitudes for a large fraction of the galaxies. These data were processed through the VISTA Data Flow System (González-Fernández et al. 2018), which provides outputs in the same form as for other VISTA public surveys, including catalogue counts and photometric calibration (per tile) for each observation. We therefore determine and extract $K_{\rm s}$-band magnitudes for sources on each tile and cross match the resulting catalogues with our GLADE output. This results in 876 matches, providing an 82% completeness. For the brightest galaxies we use the $K_{\rm s}-J$ colour from 2MASS and the redshifts reported in GLADE to k-correct the VISTA magnitudes, in order to compute the corresponding luminosities. For the remaining galaxies, we use the median k-correction (which amounts to 0.10 mag). We finally compute the $K_{\rm s}$-band luminosity as

$$\log(L_K/L_\odot) = 0.4(3.27 - \tilde{K}) - \log(1+z) + 2\log(d_{\rm L}/d_0), \tag{6}$$

where 3.27 is the absolute $K_{\rm s}$-band magnitude of the Sun (Willmer 2018) (in the Vega system), $\tilde{K}$ is the k-corrected

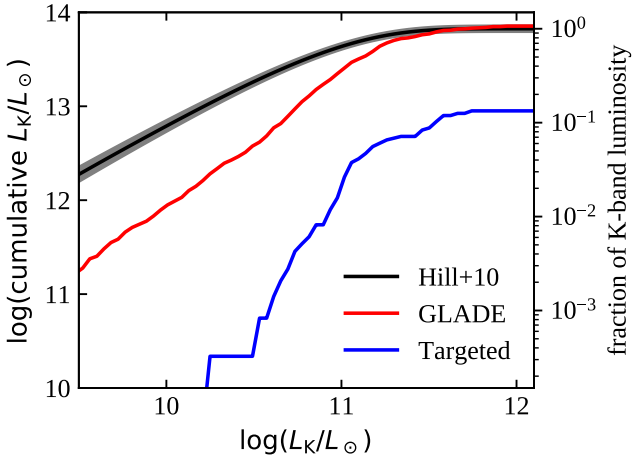

Fig. 7. Cumulative K_s-band luminosity distribution of GLADE galaxies in the S190814bv localisation region, and of our targeted galaxies, compared to the expected distribution in the 95% localisation volume assuming the K_s-band luminosity density and distribution from Hill et al. (2010). The grey area in the latter distribution represents the 1σ uncertainty.

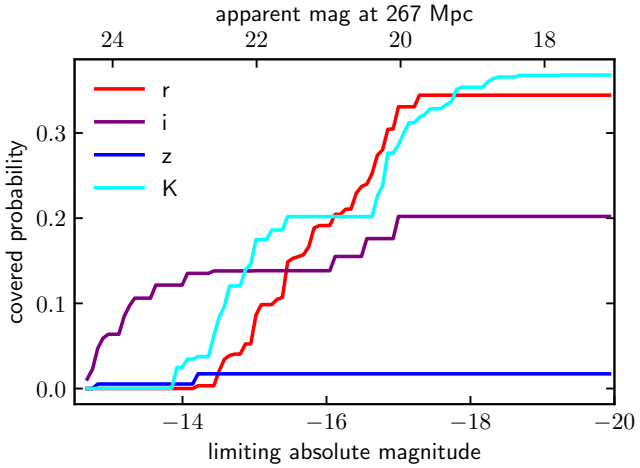

Fig. 8. Probability (as defined in Eq. (1)) covered by our galaxy-targeted search as a function of limiting absolute magnitude in different bands.

K_s-band magnitude of the galaxy, and $d_0 = 10$ pc. Summing over all galaxies with a K_s-band magnitude measurement, we obtain $L_{cat} \sim 7.8 \times 10^{13}\, L_\odot$, that is, the GLADE catalogue for S190814bv is essentially complete in terms of K_s-band luminosity. This can be seen in Fig. 7, which compares the cumulative K_s-band luminosity distribution of GLADE galaxies in the S190814bv 95% localisation volume (red line) and that of our targeted galaxies (blue line) with the expected distribution in the same volume, based on a Schechter fit to the local galaxy luminosity distribution (Hill et al. 2010). This comparison indicates that, despite the incompleteness of current catalogues, galaxy-targeting-based searches are still viable out to these distances, as already suggested, for example, by Hanna et al. (2014), Evans et al. (2016b) and Gehrels et al. (2016).

All the galaxies in our targeted search (see Table B.1) apart from five have a measured K_s-band magnitude reported in GLADE (from 2MASS). In other words, even though the HOGWARTS code selects the galaxies based on their B-band luminosity, the resulting sample is generally bright in K_s-band as well. We compute L_K (following Eq. (6)) and therefore $P_{gal,i}$ (Eq. (1)) using our VISTA magnitudes, as explained above. The resulting distribution of covered probability as a function of limiting magnitude in different bands is shown in Fig. 8. The sum of the probabilities over the targeted galaxies in our search amounts to ~50%. This does not enable us to place stringent limits on the properties of the putative EM counterpart of S190814bv using the galaxy-targeted search alone, but it nevertheless shows that targeted searches still have a reasonable chance of detecting a counterpart at ~250 Mpc.

4. Discussion

NS-BHs are hybrid merger events that offer insights into a range of behaviours that are not accessible through other mergers. They have both a larger total mass and a larger chirp mass than NS–NS systems. Thus they should produce a stronger GW signal that can be observed out to greater distances. No extant NS–BH systems are known and their range of masses, and astrophysical rates still therefore have very few observational constraints. Population synthesis models show NS–BH systems may be somewhat rarer than NS–NS (e.g., Abadie et al. 2010; Dominik et al. 2015; Eldridge & Stanway 2016; Kruckow et al. 2018; Giacobbo & Mapelli 2018; Neijssel et al. 2019), but with significant uncertainties (Belczynski et al. 2016). There is also tentative evidence that they may contribute to the known population of cosmological short GRBs (Gompertz et al. 2020b).

During the last phase of the NS–BH coalescence, the NS can be partially or totally disrupted by the BH tidal field or swallowed directly by the BH without any significant mass left outside the merger remnant (Lattimer & Schramm 1976; Shibata & Taniguchi 2011). EM emission is expected when the disruption occurs before the NS reaches the innermost stable circular orbit (ISCO) of the BH. Tidal disruption depends on the mass ratio of the two compact objects, on the BH spin, and on the NS Equation of State (EoS, Shibata & Taniguchi 2011; Kyutoku et al. 2011; Foucart 2012; Foucart et al. 2018). Simulations in Newtonian gravity show that the NS can also be disrupted over several orbits (Rosswog 2005; Davies et al. 2005). The properties of the progenitors dictate the mass ejected in tidal tails, and the potential formation of a disc wind. In turn, the properties of the ejecta (mass, electron fraction, entropy, and expansion velocity) determine the nucleosynthetic outcome, and hence the contribution that such binaries may make to the heavy element budget of the Universe (see e.g. Rosswog et al. 2017; Just et al. 2015; Roberts et al. 2017). The presence and properties of ejecta and disc determine also the possible formation of a relativistic jet and hence electromagnetic emission as a short GRB. The EM counterparts could also be much more varied than in the NS–NS case (Rosswog 2017).

Finally, the combination of a GW-detected NS–BH binary with an EM counterpart would enable a standard siren measurement of the Hubble constant and other cosmological parameters (e.g., Schutz 1986; Nissanke et al. 2010) out to larger distances than attainable via NS–NS binaries. In what follows, using our limits, we place constraints on the properties of the putative KN and GRB jet that might have been associated with S190814bv.

4.1. Constraints on kilonova emission

4.1.1. Comparison to AT2017gfo-like kilonovae

Currently, the only KN detected alongside a GW trigger is AT2017gfo, the KN that accompanied GW170817. While we have to be cautious since that source was classified as a NS–NS

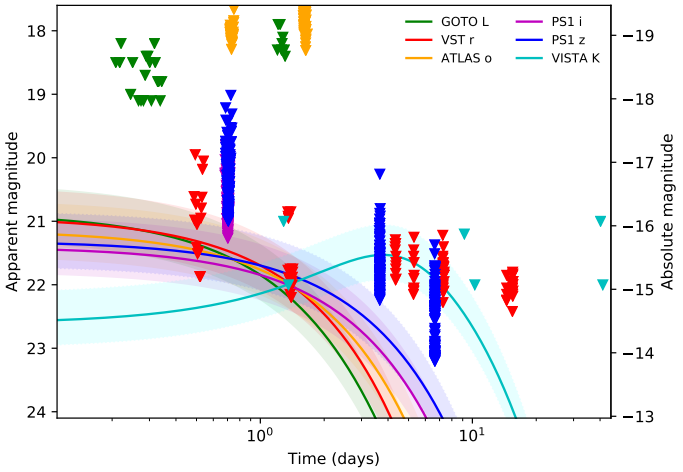

Fig. 9. 3σ or 50% completeness upper limits from the wide-field instrument follow-up campaign. The data used are referenced in Sect. 4.1. The kilonova models, representing an AT2017gfo-like evolution, are shifted to the luminosity distance measure from the LVC skymap (267 Mpc; `LALInference.v1.fits`), and the shaded regions represent the 1σ confidence interval (±52 Mpc). Absolute magnitudes assume a distance of 267 Mpc. Foreground extinction is not included.

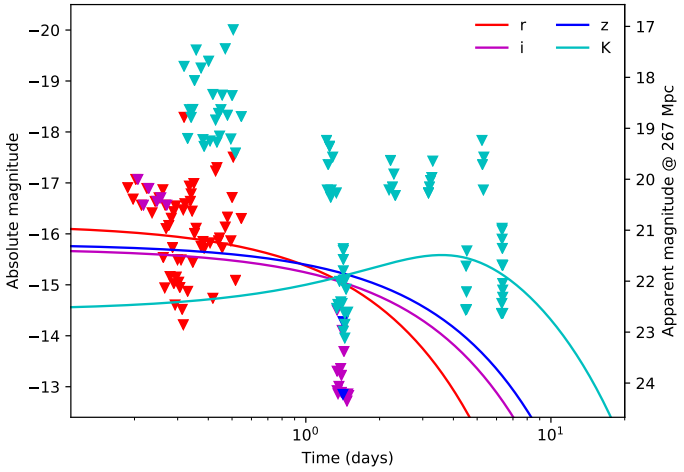

Fig. 10. Our galaxy targeted limits for S190814bv, alongside the equivalent AT2017gfo KN models. Due to the different distances of the observed galaxies, the data and models are presented in absolute magnitudes. For limits below the model lines, our observations would have uncovered a transient comparable to AT2017gfo, had it been present. We also show the apparent magnitude of the data and models when shifted to the luminosity distance of S190814bv (267 Mpc). Foreground extinction is not included.

merger (Abbott et al. 2017a), it is nonetheless prudent to compare it to our limits for S190814bv because it is the only high-confidence KN to date. Foreground[19] and host galaxy extinction is assumed to be negligible in this analysis.

Figure 9 presents our wide-field follow-up limits (ATLAS, GOTO, PS1, VISTA and VST), plotted against phenomenological fits[20] to the AT2017gfo light curve based on data from Andreoni et al. (2017), Arcavi et al. (2017a), Chornock et al. (2017), Cowperthwaite et al. (2017), Drout et al. (2017), Evans et al. (2017), Kasliwal et al. (2017), Pian et al. (2017), Smartt et al. (2017), Tanvir et al. (2017), Troja et al. (2017), Utsumi et al. (2017) and Valenti et al. (2017). We find that some of the early VST observations were deep enough to detect a KN of similar brightness to AT2017gfo if one occurred within the 1σ distance confidence interval. The first VISTA-deep observation also constrains an AT2017gfo-like KN down to the S190814bv distance, and several PS1 frames constrain the near end of the distance distribution. However the large distance to this event precludes a strong statement on whether an AT2017gfo-like event would have been detected by PS1, VISTA or VST. Our deepest limits do exclude KNe (within the relevant frames) similar to those which have been claimed to accompany GRB 130603B (Tanvir et al. 2013; Berger et al. 2013), GRB 050709 (Jin et al. 2016), GRB 060614 (Yang et al. 2015), and GRB 150101B (Gompertz et al. 2018; Troja et al. 2018b). These were all brighter than AT2017gfo at similar epochs to our sampling (Gompertz et al. 2018). Note, though, that some claimed KNe are fainter than AT2017gfo, such as those accompanying GRB 160821B (Lamb et al. 2019b; Troja et al. 2019) and GRB 070809 (Jin et al. 2020).

Our galaxy-targeted observations are able to place significantly deeper limits over a fraction of the error box. In particular, early observations, which exceeded $r > 22$ mag, are well below the expected brightness of an AT2017gfo-like KN. Data taken in the IR on timescales of 5−10 days reaching $K > 21$ mag are also competitive. This is illustrated in Fig. 10, which shows the comparison (in absolute magnitudes) between the galaxy-targeted limits and AT2017gfo. Solid lines in the figure show our phenomenological fits to the AT2017gfo light curve in the listed bands, converted to absolute magnitudes at the distances of the targeted galaxies. Downward pointing triangles show the absolute limiting magnitudes of our galaxy-targeted observations. As can be seen, early observations from the WHT and TNG in the r-band (Sects. 3.2 and 3.3), and later observations in the IR from HAWK-I are the most constraining (Sect. 3.1), and we are confident in these cases that our observations would have uncovered a KN similar to AT2017gfo if it had been present in the targeted galaxies.

In order to assess more quantitatively the ability of our observations to uncover a putative AT2017gfo-like transient, we can combine our wide-field and galaxy-targeted observations as described in Appendix A. Assuming as our EM counterpart model an AT2017gfo-like event whose flux is scaled by a constant factor, we can derive the covered probability as a function of the ratio between our limiting flux in the most constraining observations and that of AT2017gfo, which is shown in Fig. 11, where we show the covered probability in the r, i, z and K bands (red, purple, blue and cyan lines, respectively), and the combined probability (black line) that corresponds to having a constraining observation in at least one band. For the few, highest probability galaxies the most constraining limit arises from our galaxy targeted programme, but for the majority of the localisation volume the most constraining limits are through wide field observations, in particular from VST (r band), PS1 (z-band) and VISTA (K_s-band). Our search is therefore sensitive to an AT2017gfo-like KN over ∼40% of the localisation probability (as defined in Sect. 3.7), and over ∼80% to a transient with the same temporal behaviour, but brighter by a factor of 2. The most constraining observations (due to both depth and coverage) are those in the r and K_s bands.

[19] The typical value of $E(B-V)$ over the skymap is <0.1.

[20] As described on the ENGRAVE webpage, `http://www.engrave-eso.org`, these Bazin et al. (2011) model fits are purely phenomenological (cf. Gompertz et al. 2018), and describe the temporal evolution of AT2017gfo when shifted to the luminosity distance (267 Mpc) of S190814bv.

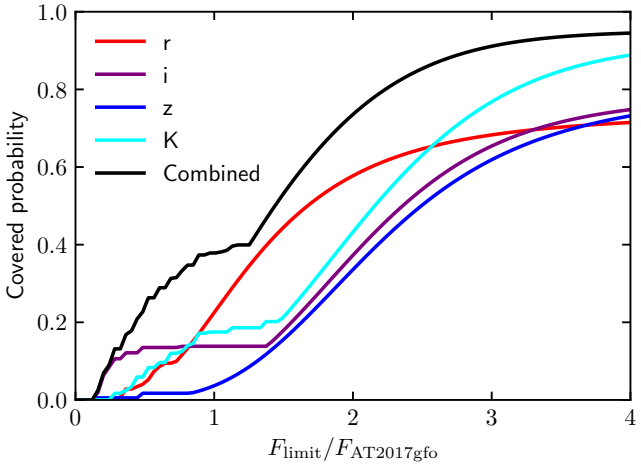

Fig. 11. Covered probability (defined as described in Appendix A) at which we are sensitive to KN of a given brightness relative to AT2017gfo, based on both our galaxy targeted observations and wide-field limits. Coloured lines show the covered probabilities in four different bands, listed in the legend. The black line shows the combined covered probability.

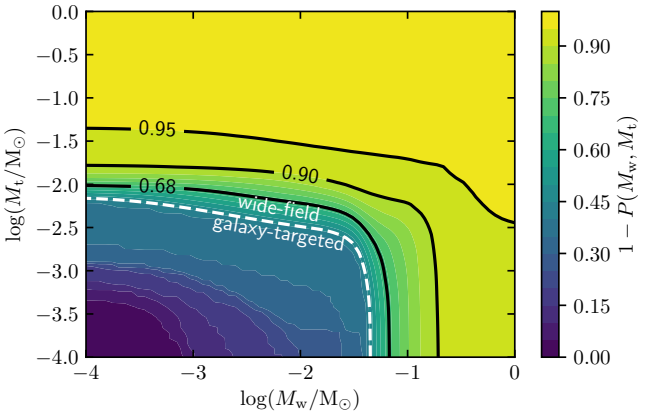

Fig. 12. Limits on the tidal ejecta mass ($M_{\rm t}$) and secular disc wind mass ($M_{\rm w}$) that we obtain by comparing the NS–BH KN model from Barbieri et al. (2019) to the limits derived from our search (both galaxy-targeted and wide-field). The colour map shows the confidence level at which we can exclude each pair ($M_{\rm w}, M_{\rm t}$).

4.1.2. Constraints on the ejecta and on the binary properties

There are fundamental differences between the merger of two NSs (e.g. Ciolfi et al. 2017; Radice et al. 2018; Wollaeger et al. 2018; Shibata & Hotokezaka 2019) and that of a NS and a BH (e.g. Foucart et al. 2013; Kyutoku et al. 2013; Fernández et al. 2017; Tanaka et al. 2014). In the latter case less extreme values for the NS–BH mass ratio, larger BH spin and stiffer NS EoS favour the disruption of the NS before the ISCO, enabling the formation of the accretion disc, tidal tails, and unbound ejecta. This material forms different components from which EM signals can originate (Rantsiou et al. 2008; Pannarale & Ohme 2014; Foucart 2012; Hinderer et al. 2019; Foucart et al. 2019; Barbieri et al. 2019). The KN emission for a given merger is a function of the mass deposited in the various components of the KN, including low-electron-fraction tidal tails (Foucart et al. 2014; Kiuchi et al. 2015; Roberts et al. 2017; Kyutoku et al. 2018) and the neutrino- and viscosity-driven less neutron-rich winds (Fernández & Metzger 2013; Just et al. 2015). It is therefore relevant to compare the observational limits on any KN emission from S190814bv with the expectations of NS–BH models.

We use, for that purpose, the multi-component, anisotropic, NS–BH-specific KN model presented in Barbieri et al. (2019), which builds on the NS–NS KN model of Perego et al. (2017). In this model, three outflow components produce KN emission: (1) the tidal ejecta (which are concentrated close to the orbital plane and have the shape of a crescent); two disc-related winds, namely (2) the neutrino-driven wind from the inner part of the accretion disc and (3) the viscosity-driven wind that results from small scale turbulence of magnetic origin inside the disc. For simplicity, since the neutrino-driven wind (2) is expected to unbind only a small fraction of the disc mass in NS–BH remnants, we neglect that component. As a further simplification, we fix the average (root mean square) velocity v and the (grey) opacity κ of the remaining two components to plausible values, namely $v_{\rm t} = 0.3c$ and $\kappa_{\rm t} = 15\,{\rm cm^2 g^{-1}}$ for the tidal ejecta and $v_{\rm w} = 0.1c$ and $\kappa_{\rm w} = 5\,{\rm cm^2 g^{-1}}$ for the viscous disc wind, based on their expected velocity and composition: the tidal ejecta are typically expected to retain a very low electron fraction $Y_{\rm e} < 0.2$ (e.g. Fernández et al. 2017) leading to efficient r-process nucleosynthesis of Lanthanides and hence a high opacity $\kappa_{\rm t} > 10\,{\rm cm^2\,g^{-1}}$ (Tanaka et al. 2020); disc wind outflows feature a wider range of $Y_{\rm e}$, due to viscous heating and neutrino irradiation from the inner part of the disc. Differently from NS–NS mergers, though, the absence of shocks and of intense neutrino production by a meta-stable neutron star remnant are likely to cause the disc wind to remain significantly neutron-rich (e.g. Fernández & Metzger 2013; Just et al. 2015). This justifies our choice of $\kappa_{\rm w} = 5\,{\rm cm^2 g^{-1}}$, which is appropriate for outflows with intermediate $Y_{\rm e} \sim 0.25 - 0.35$ (Tanaka et al. 2020). We assume $\theta_{\rm v} = 30°$ as the viewing angle[21] – measured with respect to the total angular momentum axis – which is the most likely value for a GW-detected inspiral (see Schutz 2011). We are left with the total masses of the two components, $M_{\rm t}$ and $M_{\rm w}$, as free parameters. By requiring the resulting light curves to be compatible with our upper limits (both from the galaxy-targeted and from the wide-field searches), following the method outlined in Appendix A, we obtain the constraints on $M_{\rm t}$ and $M_{\rm w}$ shown in Fig. 12. The colour map in the figure shows the confidence level at which we can exclude each pair ($M_{\rm w}, M_{\rm t}$), denoted as $1 - P(M_{\rm w}, M_{\rm t})$. The region to the lower left of the white dashed line is constrained only by galaxy-targeted observations, while the outer region is constrained mostly by wide-field observations. Large tidal ejecta masses $M_{\rm t} > 0.05\,M_\odot$ are excluded with high confidence >95%, and we can exclude the region $M_{\rm t} > 0.01\,M_\odot$ and $M_{\rm w} > 0.1\,M_\odot$ at approximately one sigma confidence.

By employing numerical-relativity-based fitting formulae that link the properties of the outflows to those of the progenitor binary (Foucart et al. 2018; Kawaguchi et al. 2016), the limits can also be translated into constraints on the NS–BH binary intrinsic properties, again following Barbieri et al. (2019, see also Barbieri et al. 2020). By assuming the disc wind mass to be 30% of the total disc mass (e.g. Fernández & Metzger 2013; Just et al. 2015; Fernández et al. 2019), we take our representative limits on the disc and tidal ejecta masses (corresponding to the region excluded at 1σ confidence in Fig. 12) to be $M_{\rm disc} < 0.3\,M_\odot$ and $M_{\rm t} < 10^{-2}\,M_\odot$, respectively. Figure 13 shows the NS–BH parameter space allowed by our limits, for three

[21] This parameter has only a minor influence on the light curve, so this assumption does not affect our results significantly.

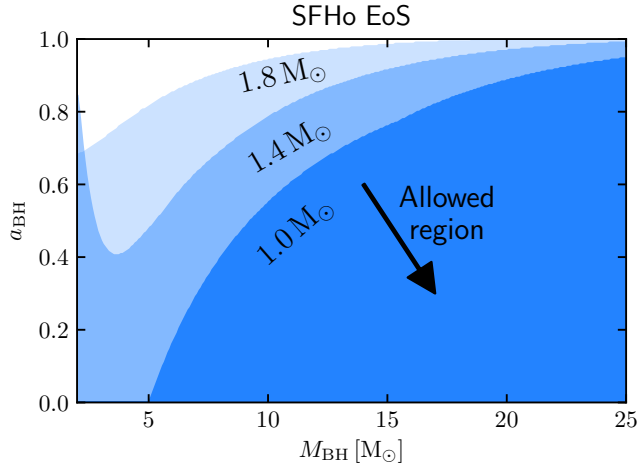

Fig. 13. Constraints on the BH spin ($a_{\rm BH}$) and the BH mass ($M_{\rm BH}$) of the NS–BH binary, assuming remnant disc and tidal ejecta mass limits of $M_{\rm disc} < 0.3\,M_\odot$ and $M_{\rm t} < 10^{-2}\,M_\odot$, which correspond to approximately 1 sigma exclusion confidence (see text). The SFHo EoS has been adopted to compute the NS tidal deformability.

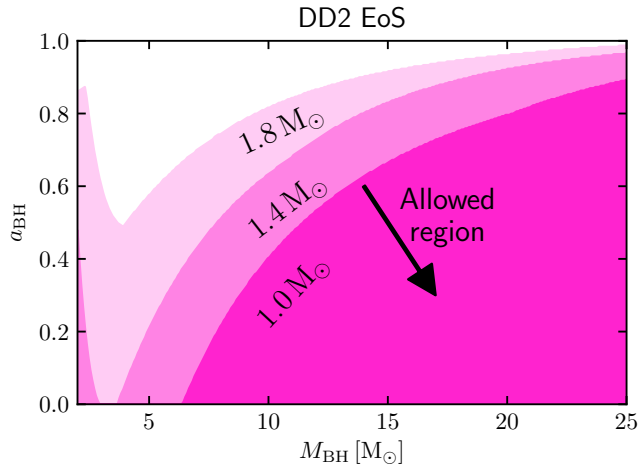

Fig. 14. Same as Fig. 13, but for the DD2 equation of state.

possible NS masses, assuming the SFHo NS EoS (Steiner et al. 2013). Different colour shades show the allowed parameter region of the binary for a fixed NS mass (reported near the edge of the region). Figure 14 shows the corresponding limits assuming the DD2 EoS (Typel et al. 2010; Hempel et al. 2012), which is stiffer than SFHo. These two EoSs are representative of the uncertainties in the NS EoS obtained from present nuclear and astrophysical constraints (e.g. Oertel et al. 2017), as well as from constraints derived from GW170817 (Abbott et al. 2018b).

Based on these results, we can therefore exclude that the progenitor NS–BH binary produced a large amount of ejecta. This is consistent with the negligible probability for remnant material left after the merger as reported by the LIGO/Virgo Collaboration in low latency (The LIGO Scientific Collaboration and the Virgo Collaboration 2019a). This indicates that most likely the NS was not disrupted by tidal forces during the final part of the inspiral towards its BH companion, which disfavours high (aligned) BH spins and small mass ratio (or both), as shown quantitatively in Figs. 12–14. At very low mass ratios $q = M_{\rm BH}/M_{\rm NS}$, the maximum allowed BH spin actually increases with decreasing BH mass. Although the NS tidal disruption is more likely for lower BH masses, the fraction of unbound mass (on which our constraint is tighter) is much smaller (Foucart et al. 2019). As a caveat, we note that the dynamical ejecta fitting formula by Kawaguchi et al. (2016) was calibrated only for mass ratios $3 \leq M_{\rm BH}/M_{\rm NS} \leq 7$ (but see Foucart et al. 2019). We note that a small or absent amount of mass left outside the remnant BH was found to be the most likely outcome of BH–NS mergers in the population synthesis simulations described in Zappa et al. (2019).

4.2. Constraints of GRB afterglow-like emission

By assuming that S190814bv launched a short GRB jet, and that all short GRBs have a similar jet structure to that seen in GW170817, we can use the upper limits on any prompt γ-ray emission to constrain the inclination of the system (e.g. Salafia et al. 2019; Saleem et al. 2020; Song et al. 2019). We employ the two jet structures of Lamb et al. (2019a) (see also Resmi et al. 2018; Salafia et al. 2019), both of which are compatible with the afterglow of GRB 170817A, namely a Gaussian and a two-component structure. For both structures, the central-core isotropic-equivalent kinetic energy is $E_{K,\rm iso} = 10^{52}$ erg and the Lorentz factor is $\Gamma = 100$. The two-component structure has "wings" with 10% of the core kinetic isotropic equivalent energy and $\Gamma = 5$. The core half-opening angles are $\theta_{\rm c} = 0.09$ rad for the Gaussian structure, and $\theta_{\rm c} = 0.07$ rad for the two-component structure. Figure 15 shows the reported *Fermi*/GBM upper-limit (Kocevksi 2019 – pink line), assuming a soft, ∼1 s duration burst (see Goldstein et al. 2016) at 267 Mpc. Using the two jet structure models described above, the observed isotropic equivalent γ-ray energy for an off-axis observer can be found using the method in Ioka & Nakamura 2019 (which is equivalent to that described in Salafia et al. 2015). We assume a 10% efficiency for energy dissipated as γ-rays by the jet and include opacity due to pair-production where the Lorentz factor is $\Gamma \lesssim 20$–30 following the method in Lamb & Kobayashi (2016, 2017, see also Matsumoto et al. 2019). The top panel of Fig. 15 shows the resulting isotropic-equivalent emitted gamma-ray energy, as a function of the viewing angle, for the Gaussian model (orange dotted line) and the two-component model (blue dash-dotted line) respectively. If there had been a successful GRB 170817A-like jet, the figure shows that the system should be inclined at >10°, or with a $(\theta_{\rm v} - \theta_{\rm c}) \gtrsim 5°$ where $\theta_{\rm c}$ is the jet's core opening angle and $\theta_{\rm v}$ is the viewing angle from the central axis. The cosmological population of short GRBs typically have an isotropic γ-ray energy in the range $10^{49} \lesssim E_{\gamma,\rm iso} \lesssim 10^{52}$ erg (Fong et al. 2015), thus a successful-GRB producing jet (if any) may have had a lower efficiency or core energy than those assumed here and the lower-limit on the off-axis angle could be smaller.

The afterglow for each structure is shown in the bottom panel of Fig. 15 at an inclination of 10° and 20° (thick and thin lines, respectively). The r band VST upper limits are shown as red triangles and the i- and z-band PS1 upper limits as purple and blue triangles, respectively. For the afterglow light curves we assume an ambient density $n = 10^{-3}\,{\rm cm}^{-3}$, microphysical parameters $\varepsilon_{\rm B} = \varepsilon_{\rm e}{}^2 = 0.01$, and an electron distribution index of $p = 2.15$. In Fig. 15 we only show the r band light-curve, noting that the difference in magnitude for r–z is $\delta m_{r-z} \sim 0.2$ for our model parameters. Our model afterglow light curve is too faint to be constrained by the upper limits. However, for these parameters we can rule out an environment with an ambient density $n \gtrsim 1\,{\rm cm}^{-3}$ for a system inclined at $(\theta_{\rm v} - \theta_{\rm c}) \sim 5°$, where we have assumed our energy and microphysical parameters are typical (e.g. Fong et al. 2015; Gompertz et al. 2015).

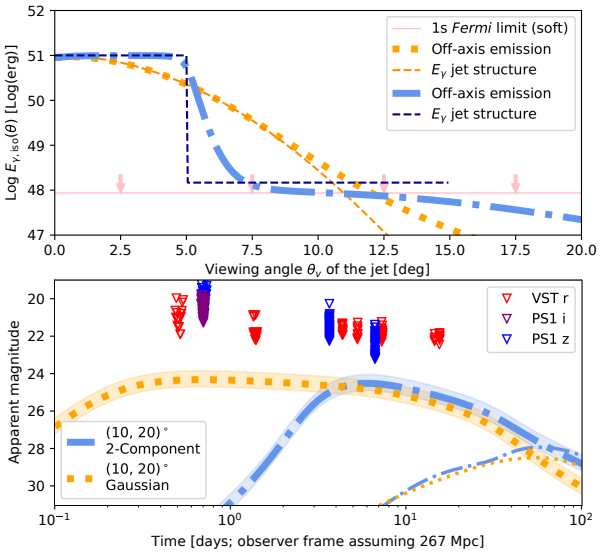

Fig. 15. *Top panel*: the upper limits from *Fermi*/GBM (Kocevksi 2019) provide an inclination limit for a GRB with a GRB 170817A-like jet structure (pink line with downward arrows). We assume two possible structures following the phenomenology of those in Lamb et al. (2019a), namely a Gaussian (orange) and a two-component structure (blue). The parameters are reported in the text. *Bottom panel*: r band afterglow for each structure (Gaussian as an orange dotted line, two-component as a blue dash-dotted line) at an inclination of 10° and 20° (thinner lines) assuming an ambient number density $n = 10^{-3}$ cm^{-3}, microphysical parameters $\varepsilon_B = {\varepsilon_e}^2 = 0.01$, and $p = 2.15$. Upper limits in the r band from VST, and i and z band limits from PS1 are shown as triangles. Models are calculated for a luminosity distance 267 Mpc, the shaded region on the 10° afterglow indicates a ±52 Mpc uncertainty in the luminosity distance.

4.3. Comparison to other studies

S190814bv has also been the target of further follow-up reported by other groups. Gomez et al. (2019a) present a study of 96 GLADE galaxies in the 50% error region, which represent 70% of the integrated luminosity in the covered region. They estimate that they cover 25% of all galaxies in the overall localisation area, and are complete down to 0.75 L^* (Schechter 1976) in the region they cover. The typical limiting magnitude they obtain after image subtraction is $i = 22.2$ mag, which is equivalent to $M_i = -14.9$ mag and therefore fainter than AT2017gfo at the distance of S190814bv, at an observing time of $\approx$ 36 hrs after the GRB. These limits are comparable to the ones we reach with VST in r at a similar time. They rule out KNe with $M_{\mathrm{ej}} > 0.01\,M_\odot$ in their observations, but the incomplete coverage prevents their observations from being constraining at a high confidence.

Andreoni et al. (2020) present the results of the EM counterpart search by the GROWTH collaboration, using both DECam wide-field tiling observations and targeted spectroscopic and photometric observations of detected candidate transients. All candidates are found to be unrelated SNe. The wide-field coverage is very complete (>98%), with the most constraining limit reached at 3.4 days, $z > 22.3$ mag. This limit is comparable to our PS1 z band limits at a similar time. Comparing their limits to different models, they constrain, depending on model and distance, the ejecta mass to $M_{\mathrm{ej}} < 0.03 \cdots 0.1\,M_\odot$, which is consistent with our results.

Watson et al. (2020) present shallow wide-field observations with the DDOTI imager, covering the entire main probability region (90% of the total probability) down to an unfiltered limit of $w > 17.9$ mag half a day after trigger. They find no candidate transients. They are able to rule out typical on-axis sGRBs but would not have detected a KN similar to AT2017gfo at the distance of S190814bv.

Dobie et al. (2019) present their search for radio transients using ASKAP. They find a single significant transient, AT2019osy, which they suggest is likely associated with a low luminosity AGN. ENGRAVE observations of AT2019osy will be presented in a companion paper in preparation.

Antier et al. (2020) report on rapid early follow-up by the Global Rapid Advanced Network Devoted to the Multi-messenger Addicts (GRANDMA), reaching limits of 17−18.5 mag within the first two hours, earlier but shallower than the GOTO limits presented in this work. These place no constraints on the potential KN emission associated with S190814bv.

Finally, during the revision of this manuscript a preprint was circulated by Vieira et al. (2020), describing the wide-field optical search by the Canada-France-Hawaii Telescope (CFHT). The search reaches limits comparable to ours, despite covering a lower total localisation probability. The corresponding constraints on the putative KN ejecta masses are similar to ours, even though we caution that they are obtained using non BHNS-specific KN models.

4.4. Ruling out identified transients as counterparts

The worldwide intensive efforts to identify a counterpart to S190814bv had led to the identification of multiple transients within the error localisation, even though this remains one of the smallest regions available. In part this is due to the deep observations that were capable of identifying transients sources fainter than 22 mag. In addition to the transients identified here through our searches, additional counterparts have been found by other groups (Andreoni et al. 2020; Gomez et al. 2019a; Dobie et al. 2019; Vieira et al. 2020). In total approximately 75 unique optical transients were identified. In principle, each of these should be considered a potential counterpart unless it can be ruled out through follow-up observations. There are various routes that such an approach can take. Firm reasons for rejection include:

1. The identification of the transient source in imaging taken prior to the detection of the GW event (Pre.Det)[22].
2. A spectrum of the source or host galaxy that places the source outside of the plausible 3D-GW volume (i.e. too distant, or too close, (Spec.Host.z)).
3. A spectrum which identifies the source as a different kind of transient event, for which the progenitors are known (SN).
4. The source is actually moving, normally because it is an asteroid, but in one case a high proper motion star (Ast, HPM).

In addition there are further indications which can be used to disfavour sources, but offer a less secure rejection of their association with S190814bv such as:

5. A photometric redshift which is inconsistent with the 3D-GW volume (Phot.Host.z).
6. A lightcurve which does not match the expectations for the counterparts of NS–NS or NS–BH mergers, but is in keeping with a supernova (SN?)
7. No obvious underlying host galaxy (No.Host)
8. A source which is nuclear in its host galaxy and therefore likely to be related to AGN activity (AGN?).

[22] The definition in parenthesis is that used in Table C.1.

These latter scenarios (5–8) are not as robust as 1–4 since each has potential pitfalls. Photometric redshifts often have significant associated uncertainty and are prone to catastrophic failure. It is possible that a photometric redshift which formally places the event outside the GW horizon could be in error. The use of lightcurves requires some assumptions as to the nature of the electromagnetic emission from the GW event. Since we have only a single well sampled kilonova, and a handful of events identified superposed to short-GRB afterglows, this provides a limited observational comparison. Furthermore, we have no kilonova clearly associated to black-hole neutron star mergers. Nonetheless there are strong reasons to expect low ejecta masses and hence strong limits on the associated luminosities and timescales, hence the photometric evolution can provide a constraint. The lack of an obvious host galaxy would at first sight suggest a distant object, or a large kick to the progenitor. In most cases we would expect to be able to identify a host within ∼100 kpc of the transient location. The absence of such a host would disfavour an association with the GW event. However, it should also be noted that some short GRBs arise from an apparently "hostless" population (e.g. Berger 2010; Tunnicliffe et al. 2014), and such an event could be missed. Finally, while most nuclear activity is due to either AGN activity or nuclear starbursts, there are suggestions that mergers could be driven at much higher rates within accretion discs around supermassive black holes (Bartos et al. 2017; Stone et al. 2017). Hence, while nuclear events would apparently be disfavoured as counterparts this should not rule them out. Indeed, the transient AT2019osy, identified as a nuclear radio transient, was an object of interest in the error region of S190814bv. For this reason we separate events which are ruled out for one of the reasons 5–8 from those firmly ruled out via 1–4.

In Appendix C we present a summary of all transient sources identified in the error region of S190814bv by our searches and those of others. We also indicate the reasons that each of these can be rejected (or not). Of the 73 sources presented there 36 are ruled out robustly, 29 are unlikely based on weaker constraints, the remaining 8 have little information to make such distinctions. There is some value in ascertaining if any of these eight events could be plausible counterparts through future observations, for example to obtain host redshifts. However, we also note that these events are not ruled out due to a paucity of observational constraints, rather than any particular diagnostics which would indicate they are likely related to S190814bv. Indeed, given the small error localisation of S190814bv and its relatively high distance, this list of transients provides some indication of the challenge that will remain in identifying robust EM counterparts to GW sources even in the 4-detector era.

5. Conclusions

S190814bv was unique amongst the GW detections to date in having an exceptionally small error box. This in turn made it plausible to search for EM emission via targeting of known galaxies. However, such searches were hampered by the large distance to the event (267 ± 52 Mpc compared to ≈40 Mpc for GW170817). Although unprecedented in previous observations, systems like S190814bv may well be more common in the future thanks to both the increasing sensitivity (hence range) of the detectors, and the addition of further GW observatories such as KAGRA in the Kamiokande underground site, Japan, and LIGO-India (Abbott et al. 2018c). Hence, it is relevant to consider what may be the most effective route to the identification of counterparts in this era (corresponding to O4 and beyond). It is striking that at these distances relatively sensitive wide-field searches such as PS1, VST and VISTA do not, in general, reach sufficiently deep limits to constrain a KN comparable in luminosity to AT2017gfo. This suggests that the current generation of wide-field facilities may not be especially well suited to the majority of candidates in the future, where observations may need to reach $r > 23$ mag to probe a reasonable fraction of KN parameter space (see Sagués Carracedo et al. 2020 and Coughlin et al. 2020 who reach similar conclusions). While some wide-field facilities may be able to attain sufficient depth over a significant fraction of future events (e.g. DECam, BlackGEM, Rubin Observatory LSST) it may well be the case that events at ∼300 Mpc may only be detectable by 8 m class observatories. The requirement to observe such events will depend sensitively on where the true event rate of NS–NS and NS–BH lies. At the higher end, optical/IR observers can focus on more nearby events. However, should the event rate lie at the lower end it is necessary to consider if 8 m telescope resources may be needed to identify counterparts, and ELT-like resources required for their follow-up. It therefore continues to be case that the effort should be expended on extending the GW detector network such that the 3D probability volumes for the GW events can become tractable for such observations to be plausible.

Acknowledgements. Based on observations collected at the European Southern Observatory under ESO programmes 1102.D-0353(E), 1102.D-0353(F), 1102.D-0353(Q), 1102.D-0353(G), 0103.D-0070(A), 0103.D-0070(B), 0103.D-0703(A), 0103.D-0722(A), 0103.A-9099(A), 198.D-2010(D) and 60.A-9285(A). ATLAS is primarily funded through NEO NASA grants NN12AR55G, 80NSSC18K0284, and 80NSSC18K1575. The ATLAS science products have been made possible through the contributions of the University of Hawaii IfA, the Queen's University Belfast, the Space Telescope Science Institute, and the South African Astronomical Observatory. PanSTARRS is primarily funded through NEO NASA grants NASA Grants NNX08AR22G, NNX14AM74G. The PanSTARRS science products for LIGO-Virgo follow-up are made possible through the contributions of the University of Hawaii IfA and the Queen's University Belfast. The Gravitational-wave Optical Transient Observer (GOTO) project acknowledges the support of the Monash-Warwick Alliance; Warwick University; Monash University; Sheffield University; Leicester University; Armagh Observatory & Planetarium; the National Astronomical Research Institute of Thailand (NARIT); University of Portsmouth; Turku University and the Instituto de Astrofísica de Canarias (IAC). Part of the funding for GROND was generously granted from the Leibniz-Prize to Prof. G. Hasinger (DFG grant HA 1850/28-1). The Liverpool Telescope is operated on the island of La Palma by Liverpool John Moores University in the Spanish Observatorio del Roque de los Muchachos of the Instituto de Astrofísica de Canarias with financial support from the UK Science and Technology Facilities Council. The WHT and its override programme are operated on the island of La Palma by the Isaac Newton Group of Telescopes in the Spanish Observatorio del Roque de los Muchachos of the Instituto de Astrofísica de Canarias; part of these data were taken under program (19A)N3. FEB thanks CONICYT Basal AFB-170002 and Chile's Ministry of Economy fund IC120009. MGB, PDA and AM acknowledge support from ASI grant I/004/11/3. MBr, EC, AP and SPi acknowledge support from MIUR (PRIN 2017 grant 20179ZF5KS). EB, EM and MT acknowledge funding from GRAWITA. SHB is indebted to the Danish National Research Foundation (DNRF132) for support. SCa acknowledges support from grant MAE0065741. EC acknowledges the support of the H2020 OPTICON programme 730890. TWC acknowledges the Humboldt Foundation and Marie Sklodowska-Curie grant 842471. MDP thanks Istanbul University for support. PAE acknowledges UKSA support. RAJEF is supported by an STFC studentship. MF is supported by a Royal Society – SFI University Research Fellowship. LG was funded by the EU H2020 programme under MSCA grant no. 839090. CG, JH and LI were supported by a research grant from VILLUM FONDEN (project 16599). CG and LI were supported by a research grant from VILLUM FONDEN (25501). GGh acknowledges the PRIN MIUR "Figaro" for financial support. AGo acknowledges financial support from the Slovenian Research Agency (grants P1-0031, I0-0033, and J1-8136). BPG, AJL and JDL acknowledge support from ERC grant 725246 (TEDE, PI Levan). SGG acknowledges support by FCT Fundação para a Ciência e Tecnologia and by Project PTDC/FIS-AST-31546. GGr acknowledges the ESCAPE H2020 project no. 824064. MG is supported by the Polish NCN MAESTRO grant 2014/14/A/ST9/00121. PJG acknowledges support from NOVA and from the South African NRF SARChI grant 111692.

CPG and MS acknowledge support from EU/FP7-ERC grant no. 615929. KEH acknowledges support by a Project Grant from The Icelandic Research Fund. YDH acknowledges support from the China Scholarships Council. JJ acknowledges support from NOVA and NWO-FAPESP grant for instrumentation. AJ acknowledges funding from the European Research Council (ERC). ZPJ was supported by the Foundation for Distinguished Young Scholars of Jiangsu Province (no. BK20180050). PGJ acknowledges funding from the ERC under Consolidator Grant agreement no. 647208. DAK acknowledges Spanish research project RTI2018-098104-J-I00 (GRBPhot). SKl acknowledges support by DFG grant Kl 766/16-3. ECK acknowledges support from the GREAT research environment. GPL acknowledges support from STFC via grant ST/N000757/1. GL was supported by a research grant (19054) from VILLUM FONDEN. KM acknowledges support from the ERC (grant no. 758638). IM is partially supported by OzGrav (ARC project CE17010000). MM acknowledges support from ERC through ERC-2017-CoG no. 770017. MJM acknowledges the National Science Centre, Poland, grant 2018/30/E/ST9/00208. BMJ and DW are supported by Independent Research Fund Denmark grant DFF-7014-00017. MN is supported by a Royal Astronomical Society Research Fellowship. ANG acknowledges support by grant DFG Kl 766/16-3. PTOB acknowledges funding from STFC. SRO gratefully acknowledges the support of the Leverhulme Trust. FO acknowledges the support of the H2020 Hemera program, grant no. 730970. MAPT was supported by grants RYC-2015-17854 and AYA2017-83216-P. EP aknowledges financial support from INAF. GP is supported by the Millennium Science Initiative through grant IC120009. MLP is partially supported by a "Linea 2" project of the Catania University. JQV acknowledges support from CONICYT folio 21180886. TMR acknowledges the support of the Vilho, Yrjo and Kalle Vaisala Foundation. ARo acknowledges support from Premiale LBT 2013. SR is supported by VR grants 2016-03657_3 and the research environment grant GREAT, Dnr. 2016-06012, and the Swedish National Space board, Dnr. 107/16. OSS acknowledges the Italian Ministry of Research (MIUR) grant 1.05.06.13. LSa acknowledges the Irish Research Council Scholarship no. GOIPG/2017/1525. SJS acknowledges support from STFC Grant ST/P000312/1. ERS and DS acknowledge funding from UK STFC CG ST/P000495/1. RLCS acknowledges funding from STFC. DS acknowledges support from STFC via grant ST/T007184/1. SDV acknowledges the support of the CNES. LW supported by Polish NCN DAINA 2017/27/L/ST9/03221. The Cosmic DAWN center is funded by the Danish National Research Foundation.

References

Abadie, J., Abbott, B. P., Abbott, R., et al. 2010, Classical Quantum Gravity, 27, 173001
Abazajian, K. N., Adelman-McCarthy, J. K., Agüeros, M. A., et al. 2009, ApJS, 182, 543
Abbott, B. P., Abbott, R., Abbott, T. D., et al. 2016, Phys. Rev. Lett., 116, 061102
Abbott, B. P., Abbott, R., Abbott, T. D., et al. 2017a, Phys. Rev. Lett., 119, 161101
Abbott, B. P., Abbott, R., Abbott, T. D., et al. 2017b, ApJ, 848, L13
Abbott, B. P., Abbott, R., Abbott, T. D., et al. 2017c, ApJ, 848, L12
Abbott, B. P., Abbott, R., Abbott, T. D., et al. 2017d, Nature, 551, 85
Abbott, T. M. C., Abdalla, F. B., Allam, S., et al. 2018a, ApJS, 239, 18
Abbott, B. P., Abbott, R., Abbott, T. D., et al. 2018b, Phys. Rev. Lett., 121, 161101
Abbott, B. P., Abbott, R., Abbott, T. D., et al. 2018c, Liv. Rev. Relativ., 21, 3
Ackley, K., Dyer, M., Eyles, R., et al. 2019, GRB Coordinates Network, 25337, 1
Acosta-Pulido, J., Ballesteros, E., Barreto, M., et al. 2002, Newsletter Isaac Newton Group Telescopes, 6, 22
Ageron, M., Baret, B., Coleiro, A., et al. 2019, GRB Coordinates Network, 25330, 1
Alam, S., Albareti, F. D., Allende Prieto, C., et al. 2015, ApJS, 219, 12
Alvarez-Muniz, J., Pedreira, F., Zas, E., Hampert, K. H., & Schimp, M. 2019, GRB Coordinates Network, 25409, 1
Andreoni, I., Ackley, K., Cooke, J., et al. 2017, PASA, 34, e069
Andreoni, I., Goldstein, D. A., Ahumada, T., et al. 2019a, GRB Coordinates Network, 25362, 1
Andreoni, I., Goldstein, D. A., Dobie, D., & Kasliwal, M. M. 2019b, GRB Coordinates Network, 25488, 1
Andreoni, I., Goldstein, D. A., Kasliwal, M. M., et al. 2020, ApJ, 890, 131
Antier, S., Agayeva, S., Aivazyan, V., et al. 2020, MNRAS, 492, 3904
Appenzeller, I., Fricke, K., Fürtig, W., et al. 1998, The Messenger, 94, 1
Arcavi, I., Hosseinzadeh, G., Howell, D. A., et al. 2017a, Nature, 551, 64
Arcavi, I., McCully, C., Hosseinzadeh, G., et al. 2017b, ApJ, 848, L33
Arnaboldi, M., Petr-Gotzens, M., Rejkuba, M., et al. 2010, The Messenger, 139, 6
Arsenault, R., Hubin, N., Stroebele, S., et al. 2006, The Messenger, 123, 6
Artale, M. C., Mapelli, M., Giacobbo, N., et al. 2019, MNRAS, 487, 1675
Barbieri, C., Salafia, O. S., Perego, A., Colpi, M., & Ghirlanda, G. 2019, A&A, 625, A152
Barbieri, C., Salafia, O. S., Perego, A., Colpi, M., & Ghirlanda, G. 2020, Eur. Phys. J. A, 56, 8
Bartos, I., Kocsis, B., Haiman, Z., & Márka, S. 2017, ApJ, 835, 165
Bauer, F. E., Fruchter, A. S., Gonzalez Lopez, J., et al. 2019, GRB Coordinates Network, 25801, 1
Bazin, G., Ruhlmann-Kleider, V., Palanque-Delabrouille, N., et al. 2011, A&A, 534, A43
Becker, A. 2015, Astrophysics Source Code Library [record ascl:1504.004]
Belczynski, K., Holz, D. E., Bulik, T., & O'Shaughnessy, R. 2016, Nature, 534, 512
Benn, C., Dee, K., & Agócs, T. 2008, in ACAM: A New Imager/Spectrograph for the William Herschel Telescope, SPIE Conf. Ser., 7014, 70146X
Berger, E. 2010, ApJ, 722, 1946
Berger, E., Fong, W., & Chornock, R. 2013, ApJ, 774, L23
Bertin, E., & Arnouts, S. 1996, A&AS, 117, 393
Bloom, J. S., Richards, J. W., Nugent, P. E., et al. 2012, PASP, 124, 1175
Boksenberg, A. 1985, Vistas Astron, 28, 531
Brocato, E., Branchesi, M., Cappellaro, E., et al. 2018, MNRAS, 474, 411
Brunn, S. H., Sagues Carracedo, A., Chen, T.-W., et al. 2019, GRB Coordinates Network, 25384, 1
Cai, C., Yi, Q. B., Xiao, S., et al. 2019, GRB Coordinates Network, 25365, 1
Capaccioli, M., & Schipani, P. 2011, The Messenger, 146, 2
Cartier, R., Briceno, C., Olivares, F., et al. 2019, GRB Coordinates Network, 25784, 1
Casali, M., Pirard, J.-F., Kissler-Patig, M., et al. 2006, in SPIE Conf. Ser., Proc. SPIE, 6269, 62690W
Castro-Tirado, A. J., Valeev, A. F., Hu, Y.-D., et al. 2019, GRB Coordinates Network, 25543, 1
Chambers, K. C., Magnier, E. A., Metcalfe, N., et al. 2016, ArXiv e-prints [arXiv:1612.05560]
Chen, T.-W., Nicuesa Guelbenzu, A., Fraser, M., et al. 2019, GRB Coordinates Network, 25372, 1
Chornock, R., Berger, E., Kasen, D., et al. 2017, ApJ, 848, L19
Ciolfi, R., Kastaun, W., Giacomazzo, B., et al. 2017, Phys. Rev. D, 95, 063016
Colless, M., Dalton, G., Maddox, S., et al. 2001, MNRAS, 328, 1039
Coughlin, M. W., Dietrich, T., Antier, S., et al. 2020, MNRAS, 492, 863
Coulter, D. A., Foley, R. J., Kilpatrick, C. D., et al. 2017a, Science, 358, 1556
Coulter, D., Kilpatrick, C., Siebert, M., et al. 2017b, GRB Coordinates Network, 21529, 1
Covino, S., Wiersema, K., Fan, Y. Z., et al. 2017, Nat. Astron., 1, 791
Cowperthwaite, P. S., Berger, E., Villar, V. A., et al. 2017, ApJ, 848, L17
Dálya, G., Galgóczi, G., Dobos, L., et al. 2018, MNRAS, 479, 2374
D'Avanzo, P., Campana, S., Salafia, O. S., et al. 2018, A&A, 613, L1
D'Avanzo, P., Melandri, A., Izzo, L., et al. 2019a, GRB Coordinates Network, 25331, 1
D'Avanzo, P., Rossi, A., Greco, G., et al. 2019b, GRB Coordinates Network, 25361, 1
Davies, M. B., Levan, A. J., & King, A. R. 2005, MNRAS, 356, 54
De, K., Jencson, J., Kasliwal, M. M., Goldstein, D. A., & Andreoni, I. 2019a, GRB Coordinates Network, 25478, 1
De, K., Goldstein, D., Andreoni, I., et al. 2019b, GRB Coordinates Network, 25348, 1
Dichiari, S., Troja, E., Cenko, S. B., et al. 2019, GRB Coordinates Network, 25374, 1
Dimitriadis, G., Brown, J. S., Seibert, M. R., et al. 2019, GRB Coordinates Network, 25395, 1
Dobie, D., Kaplan, D. L., Murphy, T., et al. 2018, ApJ, 858, L15
Dobie, D., Stewart, A., Murphy, T., et al. 2019, ApJ, 887, L13
Dominik, M., Berti, E., O'Shaughnessy, R., et al. 2015, ApJ, 806, 263
Drout, M. R., Piro, A. L., Shappee, B. J., et al. 2017, Science, 358, 1570
Dyer, M. J., Dhillon, V. S., Littlefair, S., et al. 2018, in Observatory Operations: Strategies, Processes, and Systems VII, SPIE Conf. Ser., 10704, 107040C
Eichler, D., Livio, M., Piran, T., & Schramm, D. N. 1989, Nature, 340, 126
Eldridge, J. J., & Stanway, E. R. 2016, MNRAS, 462, 3302
Evans, P. A., Osborne, J. P., Kennea, J. A., et al. 2016a, MNRAS, 455, 1522
Evans, P. A., Kennea, J. A., Barthelmy, S. D., et al. 2016b, MNRAS, 460, L40
Evans, P. A., Cenko, S. B., Kennea, J. A., et al. 2017, Science, 358, 1565
Evans, P. A., Kennea, J. A., Tohuvavohu, A., et al. 2019, GRB Coordinates Network, 25400, 1
Fernández, R., & Metzger, B. D. 2013, MNRAS, 435, 502
Fernández, R., Foucart, F., Kasen, D., et al. 2017, Classical Quantum Gravity, 34, 154001
Fernández, R., Tchekhovskoy, A., Quataert, E., Foucart, F., & Kasen, D. 2019, MNRAS, 482, 3373
Flesch, E. W. 2015, PASA, 32, e010

Flewelling, H. A., Magnier, E. A., Chambers, K. C., et al. 2016, ArXiv e-prints [arXiv:1612.05243]
Fong, W., & Berger, E. 2013, ApJ, 776, 18
Fong, W., Berger, E., Margutti, R., & Zauderer, B. A. 2015, ApJ, 815, 102
Foucart, F. 2012, Phys. Rev. D, 86, 124007
Foucart, F., Deaton, M. B., Duez, M. D., et al. 2013, Phys. Rev. D, 87, 084006
Foucart, F., Deaton, M. B., Duez, M. D., et al. 2014, Phys. Rev. D, 90, 024026
Foucart, F., Hinderer, T., & Nissanke, S. 2018, Phys. Rev. D, 98, 081501
Foucart, F., Duez, M. D., Kidder, L. E., et al. 2019, Phys. Rev. D, 99, 103025
Freiburghaus, C., Rosswog, S., & Thielemann, F.-K. 1999, ApJ, 525, L121
Freudling, W., Romaniello, M., Bramich, D. M., et al. 2013, A&A, 559, A96
Gaia Collaboration (Brown, A. G. A., et al.) 2016, A&A, 595, A2
Gall, C., Hjorth, J., Rosswog, S., Tanvir, N. R., & Levan, A. J. 2017, ApJ, 849, L19
Gehrels, N., Cannizzo, J. K., Kanner, J., et al. 2016, ApJ, 820, 136
Ghirlanda, G., Salafia, O. S., Paragi, Z., et al. 2019, Science, 363, 968
Giacobbo, N., & Mapelli, M. 2018, MNRAS, 480, 2011
Goldstein, D. A., & Anand, S. 2019, GRB Coordinates Network, 25394, 1
Goldstein, A., Burns, E., Hamburg, R., et al. 2016, ArXiv e-prints [arXiv:1612.02395]
Goldstein, A., Veres, P., Burns, E., et al. 2017, ApJ, 848, L14
Goldstein, D., Perley, D. A., Andreoni, I., & Kasliwal, M. M. 2019a, GRB Coordinates Network, 25355, 1
Goldstein, D. A., Andreoni, I., Zhou, R., et al. 2019b, GRB Coordinates Network, 25391, 1
Goldstein, D. A., Andreoni, I., Hankins, M., et al. 2019c, GRB Coordinates Network, 25393, 1
Gomez, S., Hosseinzadeh, G., Cowperthwaite, P. S., et al. 2019a, ApJ, 884, L55
Gomez, S., Hosseinzadeh, G., Berger, E., et al. 2019b, GRB Coordinates Network, 25483, 1
Gompertz, B. P., van der Horst, A. J., O'Brien, P. T., Wynn, G. A., & Wiersema, K. 2015, MNRAS, 448, 629
Gompertz, B. P., Levan, A. J., Tanvir, N. R., et al. 2018, ApJ, 860, 62
Gompertz, B. P., Cutter, R., Steeghs, D., et al. 2020a, MNRAS, 497, 726
Gompertz, B. P., Levan, A. J., & Tanvir, N. R. 2020b, ApJ, 895, 58
González-Fernández, C., Hodgkin, S. T., Irwin, M. J., et al. 2018, MNRAS, 474, 5459
Grado, A., Cappelaro, E., Getman, F., et al. 2019a, GRB Coordinates Network, 25371, 1
Grado, A., Cappellaro, E., Brocato, E., et al. 2019b, GRB Coordinates Network, 25669, 1
Grado, A., Cappellaro, E., Covino, S., et al. 2020, MNRAS, 492, 1731
Greiner, J., Bornemann, W., Clemens, C., et al. 2008, PASP, 120, 405
Hanna, C., Mandel, I., & Vousden, W. 2014, ApJ, 784, 8
Hempel, M., Fischer, T., Schaffner-Bielich, J., & Liebendörfer, M. 2012, ApJ, 748, 70
Herner, K., Palmese, A., Soares-Santos, M., et al. 2019a, GRB Coordinates Network, 25373, 1
Herner, K., Palmese, A., Soares-Santes, M., et al. 2019b, GRB Coordinates Network, 25398, 1
Hill, D. T., Driver, S. P., Cameron, E., et al. 2010, MNRAS, 404, 1215
Hinderer, T., Nissanke, S., Foucart, F., et al. 2019, Phys. Rev. D, 100, 063021
Hjorth, J., Levan, A. J., Tanvir, N. R., et al. 2017, ApJ, 848, L31
Hu, Y.-D., Castro-Tirado, A. J., Valeev, A. F., et al. 2019, GRB Coordinates Network, 25588, 1
Huber, M., Smith, K. W., Chambers, K., et al. 2019, GRB Coordinates Network, 25356, 1
IceCube Collaboration 2019, GRB Coordinates Network, 25321, 1
Ioka, K., & Nakamura, T. 2019, MNRAS, 487, 4884
Japelj, J., Jin, Z., Kankare, E., et al. 2019a, GRB Coordinates Network, 25447, 1
Japelj, J., Kankare, E., Kool, E., et al. 2019b, GRB Coordinates Network, 25526, 1
Jin, Z.-P., Hotokezaka, K., Li, X., et al. 2016, Nat. Commun., 7, 12898
Jin, Z.-P., Covino, S., Liao, N.-H., et al. 2020, Nat. Astron., 4, 77
Jonker, P., Maguire, K., Fraser, M., et al. 2019, GRB Coordinates Network, 25454, 1
Just, O., Bauswein, A., Ardevol Pulpillo, R., Goriely, S., & Janka, H.-T. 2015, MNRAS, 448, 541
Kasen, D., Metzger, B., Barnes, J., Quataert, E., & Ramirez-Ruiz, E. 2017, Nature, 551, 80
Kasliwal, M. M., Nakar, E., Singer, L. P., et al. 2017, Science, 358, 1559
Kawaguchi, K., Kyutoku, K., Shibata, M., & Tanaka, M. 2016, ApJ, 825, 52
Kissler-Patig, M., Pirard, J.-F., Casali, M., et al. 2008, A&A, 491, 941
Kiuchi, K., Sekiguchi, Y., Kyutoku, K., et al. 2015, Phys. Rev. D, 92, 064034
Kocevksi, D. 2019, GRB Coordinates Network, 25326, 1
Kruckow, M. U., Tauris, T. M., Langer, N., Kramer, M., & Izzard, R. G. 2018, MNRAS, 481, 1908
Krühler, T., Küpcü Yoldas, A., Greiner, J., et al. 2008, ApJ, 685, 376
Kuijken, K. 2011, The Messenger, 146, 8
Kulkarni, S. R., Perley, D. A., & Miller, A. A. 2018, ApJ, 860, 22
Kyutoku, K., Okawa, H., Shibata, M., & Taniguchi, K. 2011, Phys. Rev. D, 84, 064018
Kyutoku, K., Ioka, K., & Shibata, M. 2013, Phys. Rev. D, 88, 041503
Kyutoku, K., Kiuchi, K., Sekiguchi, Y., Shibata, M., & Taniguchi, K. 2018, Phys. Rev. D, 97, 023009
Lamb, G. P., & Kobayashi, S. 2016, ApJ, 829, 112
Lamb, G. P., & Kobayashi, S. 2017, MNRAS, 472, 4953
Lamb, G. P., Lyman, J. D., Levan, A. J., et al. 2019a, ApJ, 870, L15
Lamb, G. P., Tanvir, N. R., Levan, A. J., et al. 2019b, ApJ, 883, 48
Lattimer, J. M., & Schramm, D. N. 1976, ApJ, 210, 549
Lattimer, J. M., Mackie, F., Ravenhall, D. G., & Schramm, D. N. 1977, ApJ, 213, 225
Lazzati, D., Perna, R., Morsony, B. J., et al. 2018, Phys. Rev. Lett., 120, 241103
Levan, A. J., Lyman, J. D., Tanvir, N. R., et al. 2017, ApJ, 848, L28
Li, L.-X., & Paczyński, B. 1998, ApJ, 507, L59
Lipunov, V. M., Gorbovskoy, E., Kornilov, V. G., et al. 2017, ApJ, 850, L1
Lopez-Cruz, O., Castro-Tirado, A. J., Macri, L., et al. 2019a, GRB Coordinates Network, 25419, 1
Lopez-Cruz, O., Castro-Tirado, A. J., Macri, L., et al. 2019b, GRB Coordinates Network, 25571, 1
Lyman, J. D., Lamb, G. P., Levan, A. J., et al. 2018, Nat. Astron., 2, 751
Magnier, E.A., Chambers, K.C., Flewelling, H.A., et al. 2016, ArXiv e-prints [arXiv:1612.05240]
Margutti, R., Alexander, K. D., Xie, X., et al. 2018, ApJ, 856, L18
Matsumoto, T., Nakar, E., & Piran, T. 2019, MNRAS, 486, 1563
McCully, C., Hiramatsu, D., Howell, D. A., et al. 2017, ApJ, 848, L32
Metzger, B. D., Martínez-Pinedo, G., Darbha, S., et al. 2010, MNRAS, 406, 2650
Molinari, E., Conconi, P., Pucillo, M., & Monai, S. 1999, in Looking Deep in the Southern Sky, eds. R. Morganti, & W. J. Couch, 157
Molkov, S., Mereghetti, S., Savchenko, V., et al. 2019, GRB Coordinates Network, 25323, 1
Mooley, K. P., Frail, D. A., Dobie, D., et al. 2018, ApJ, 868, L11
Neijssel, C. J., Vigna-Gómez, A., Stevenson, S., et al. 2019, MNRAS, 490, 3740
Nicholl, M., Berger, E., Kasen, D., et al. 2017, ApJ, 848, L18
Nissanke, S., Holz, D. E., Hughes, S. A., Dalal, N., & Sievers, J. L. 2010, ApJ, 725, 496
Nissanke, S., Kasliwal, M., & Georgieva, A. 2013, ApJ, 767, 124
Nynka, M., Ruan, J. J., Haggard, D., & Evans, P. A. 2018, ApJ, 862, L19
Oertel, M., Hempel, M., Klähn, T., & Typel, S. 2017, Rev. Mod. Phys., 89, 015007
Ohno, M., Axelsson, M., Longo, F., et al. 2019, GRB Coordinates Network, 25386, 1
Oliva, E., Marconi, A., Maiolino, R., et al. 2001, A&A, 369, L5
Palmer, D. M., Barthelmy, S. D., Lien, A. Y., et al. 2019, GRB Coordinates Network, 25341, 1
Pannarale, F., & Ohme, F. 2014, ApJ, 791, L7
Perego, A., Radice, D., & Bernuzzi, S. 2017, ApJ, 850, L37
Pian, E., D'Avanzo, P., Benetti, S., et al. 2017, Nature, 551, 67
Pilia, M., Pittori, C., Tavani, M., et al. 2019a, GRB Coordinates Network, 25327, 1
Pilia, M., Pittori, C., Tavani, M., et al. 2019b, GRB Coordinates Network, 25335, 1
Pirard, J.-F., Kissler-Patig, M., Moorwood, A., et al. 2004, in Ground-based Instrumentation for Astronomy, eds. A. F. M. Moorwood, & M. Iye, Proc. SPIE, 5492, 1763
Poretti, E. 2018, https://www.doi.org/10.5281/zenodo.1892959
Radice, D., Perego, A., Hotokezaka, K., et al. 2018, ApJ, 869, 130
Rantsiou, E., Kobayashi, S., Laguna, P., & Rasio, F. A. 2008, ApJ, 680, 1326
Resmi, L., Schulze, S., Ishwara-Chandra, C. H., et al. 2018, ApJ, 867, 57
Roberts, L. F., Lippuner, J., Duez, M. D., et al. 2017, MNRAS, 464, 3907
Rodriguez, A., Meza-Retamal, N., Quirola, J., et al. 2019, GRB Coordinates Network, 25423, 1
Rossi, A., D'Avanzo, P., Cappellaro, E., et al. 2019, GRB Coordinates Network, 25383, 1
Rosswog, S. 2005, ApJ, 634, 1202
Rosswog, S. 2017, Phys. Online J., 10, 131
Rosswog, S., Feindt, U., Korobkin, O., et al. 2017, Classical Quantum Gravity, 34, 104001
Ruan, J., Vieira, N., Haggard, D., et al. 2019, GRB Coordinates Network, 25443, 1
Sagués Carracedo, A., Bulla, M., Feindt, U., & Goobar, A. 2020, MNRAS, submitted [arXiv:2004.06137]
Salafia, O. S., Ghisellini, G., Pescalli, A., Ghirlanda, G., & Nappo, F. 2015, MNRAS, 450, 3549
Salafia, O. S., Ghirlanda, G., Ascenzi, S., & Ghisellini, G. 2019, A&A, 628, A18

Saleem, M., Resmi, L., Arun, K. G., & Mohan, S. 2020, ApJ, 891, 130
Salmon, L., Hanlon, L., Jeffrey, R. M., & Martin-Carrillo, A. 2020, A&A, 634, A32
Savchenko, V., Ferrigno, C., Kuulkers, E., et al. 2017, ApJ, 848, L15
Schechter, P. 1976, ApJ, 203, 297
Schutz, B. F. 1986, Nature, 323, 310
Schutz, B. F. 2011, Classical Quantum Gravity, 28, 125023
Shappee, B. J., Simon, J. D., Drout, M. R., et al. 2017, Science, 358, 1574
Shibata, M., & Hotokezaka, K. 2019, Ann. Rev. Nucl. Part. Sci., 69, 41
Shibata, M., & Taniguchi, K. 2011, Liv. Rev. Relativ., 14, 6
Siebenmorgen, R., Carraro, G., Valenti, E., et al. 2011, The Messenger, 144, 9
Singer, L. P., Chen, H.-Y., Holz, D. E., et al. 2016, ApJ, 829, L15
Skrutskie, M. F., Cutri, R. M., Stiening, R., et al. 2006, AJ, 131, 1163
Smartt, S. J., Chambers, K. C., Smith, K. W., et al. 2016a, MNRAS, 462, 4094
Smartt, S. J., Chambers, K. C., Smith, K. W., et al. 2016b, ApJ, 827, L40
Smartt, S. J., Chen, T.-W., Jerkstrand, A., et al. 2017, Nature, 551, 75
Smartt, S. J., Smith, K. W., Srivastav, S., et al. 2019a, GRB Coordinates Network, 25455, 1
Smartt, S. J., Malesani, D. B., Smith, K. W., et al. 2019b, GRB Coordinates Network, 25386, 1
Soares-Santos, M., Holz, D. E., Annis, J., et al. 2017, ApJ, 848, L16
Soares-Santos, M., Tucker, D., Allam, S., et al. 2019a, GRB Coordinates Network, 25336, 1
Soares-Santos, M., Annis, J., Garcia, A., et al. 2019b, GRB Coordinates Network, 25425, 1
Soares-Santos, M., Annis, J., Garcia, A., et al. 2019c, GRB Coordinates Network, 25438, 1
Soares-Santos, M., Annis, J., Herner, K., et al. 2019d, GRB Coordinates Network, 25486, 1
Song, H.-R., Ai, S.-K., Wang, M.-H., et al. 2019, ApJ, 881, L40
Srivastas, S., Huber, M., Smartt, S. J., et al. 2019, GRB Coordinates Network, 25417, 1
Stalder, B., Tonry, J., Smartt, S. J., et al. 2017, ApJ, 850, 149
Steele, I. A., Smith, R. J., Rees, P. C., et al. 2004, in The Liverpool Telescope: Performance and First Results, SPIE Conf. Ser., 5489, 679
Steiner, A. W., Hempel, M., & Fischer, T. 2013, ApJ, 774, 17
Stewart, A., Dobie, D., Murphy, T., et al. 2019, GRB Coordinates Network, 25487, 1
Stone, N. C., Metzger, B. D., & Haiman, Z. 2017, MNRAS, 464, 946
Sugizaki, M., Kawai, N., Negoro, H., et al. 2019, GRB Coordinates Network, 25329, 1
Sutherland, W., Emerson, J., Dalton, G., et al. 2015, A&A, 575, A25
Svinkin, D., Golenetskii, S., Aptekar, R., et al. 2019, GRB Coordinates Network, 25369, 1
Tanaka, M., Hotokezaka, K., Kyutoku, K., et al. 2014, ApJ, 780, 31
Tanaka, M., Kato, D., Gaigalas, G., & Kawaguchi, K. 2020, MNRAS, 496, 1369
Tanvir, N. R., Levan, A. J., Fruchter, A. S., et al. 2013, Nature, 500, 547
Tanvir, N. R., Levan, A. J., González-Fernández, C., et al. 2017, ApJ, 848, L27
The LIGO Scientific Collaboration and the Virgo Collaboration 2019a, GRB Coordinates Network, 25324, 1
The LIGO Scientific Collaboration and the Virgo Collaboration 2019b, GRB Coordinates Network, 25333, 1
Tonry, J. L., Stubbs, C. W., Lykke, K. R., et al. 2012, ApJ, 750, 99
Tonry, J. L., Denneau, L., Heinze, A. N., et al. 2018a, PASP, 130, 064505
Tonry, J. L., Denneau, L., Flewelling, H., et al. 2018b, ApJ, 867, 105
Troja, E., Piro, L., van Eerten, H., et al. 2017, Nature, 551, 71
Troja, E., Piro, L., Ryan, G., et al. 2018a, MNRAS, 478, L18
Troja, E., Ryan, G., Piro, L., et al. 2018b, Nat. Commun., 9, 4089
Troja, E., Castro-Tirado, A. J., Becerra González, J., et al. 2019, MNRAS, 489, 2104
Tucker, D., Butner, M., Wiesner, M., et al. 2019a, GRB Coordinates Network, 25484, 1
Tucker, D., Allam, S., Wiesner, M., et al. 2019b, GRB Coordinates Network, 25379, 1
Tunnicliffe, R. L., Levan, A. J., Tanvir, N. R., et al. 2014, MNRAS, 437, 1495
Typel, S., Röpke, G., Klähn, T., Blaschke, D., & Wolter, H. H. 2010, Phys. Rev. C, 81, 015803
Utsumi, Y., Tanaka, M., Tominaga, N., et al. 2017, PASJ, 69, 101
Valenti, S., David, J., Yang, S., et al. 2017, ApJ, 848, L24
Veitch, J., Raymond, V., Farr, B., et al. 2015, Phys. Rev. D, 91, 042003
Véron-Cetty, M. P., & Véron, P. 2001, A&A, 374, 92
Vieira, N., Ruan, J. J., Haggard, D., et al. 2020, ApJ, 895, 96
Waters, C. Z., Magnier, E. A., Price, P. A., et al. 2016, ArXiv e-prints [arXiv:1612.05245]
Watson, D., Hansen, C. J., Selsing, J., et al. 2019, Nature, 574, 497
Watson, A. M., Butler, N. R., Lee, W. H., et al. 2020, MNRAS, 492, 5916
Wiesner, M., Butner, M., Allam, S., et al. 2019a, GRB Coordinates Network, 25596, 1
Wiesner, M., Butner, M., Tucker, D., et al. 2019b, GRB Coordinates Network, 25540, 1
Willmer, C. N. A. 2018, ApJS, 236, 47
Wollaeger, R. T., Korobkin, O., Fontes, C. J., et al. 2018, MNRAS, 478, 3298
Yang, S. 2018, Ph.D. thesis, http://paduaresearch.cab.unipd.it/11854/
Yang, B., Jin, Z.-P., Li, X., et al. 2015, Nat. Commun., 6, 7323
Yang, S., Cappellaro, E., Grado, A., et al. 2019, GRB Coordinates Network, 25748, 1
Zappa, F., Bernuzzi, S., Pannarale, F., Mapelli, M., & Giacobbo, N. 2019, Phys. Rev. Lett, 123, 041102

[1] School of Physics and Astronomy, Monash University, Clayton, Victoria 3800, Australia
[2] INAF – Osservatorio di Astrofisica e Scienza dello Spazio di Bologna, Via Piero Gobetti 93/3, 40129 Bologna, Italy
[3] INAF / Brera Astronomical Observatory, Via Bianchi 46, 23807 Merate, LC, Italy
[4] INFN – Sezione di Milano-Bicocca, Piazza della Scienza 3, 20126 Milano, MI, Italy
[5] University of Milano-Bicocca, Department of Physics "G. Occhialini", Piazza della Scienza 3, 20126 Milano, Italy
[6] Instituto de Astrofísica and Centro de Astroingeniería, Facultad de Física, Pontificia Uni versidad Católica de Chile, Casilla 306, Santiago 22, Chile
[7] Millennium Institute of Astrophysics (MAS), Nuncio Monseñor Sótero Sanz 100, Providencia, Santiago, Chile
[8] Space Science Institute, 4750 Walnut Street, Suite 205, Boulder, CO 80301, USA
[9] INAF, Osservatorio Astronomico di Padova, 35122 Padova, Italy
[10] Space Telescope Science Institute, 3700 San Martin Drive, Baltimore, MD 21218, USA
[11] INAF Osservatorio Astronomico di Capodimonte, Via Moiariello 16, 80131 Napoli, Italy
[12] Gran Sasso Science Institute, Viale F. Crispi 7, 67100 L'Aquila, AQ, Italy
[13] INFN – Laboratori Nazionali del Gran Sasso, 67100 L'Aquila, AQ, Italy
[14] INAF, Osservatorio Astronomico di Roma, Via di Frascati 33, 00078 Monteporzio Catone, RM, Italy
[15] INAF – Osservatorio Astronomico d'Abruzzo, Via M. Maggini snc, 64100 Teramo, Italy
[16] DARK, Niels Bohr Institute, University of Copenhagen, Lyngbyvej 2, 2100 Copenhagen Ø, Denmark
[17] Nordita, KTH Royal Institute of Technology and Stockholm University, Roslagstullsbacken 23, 106 91 Stockholm, Sweden
[18] Instituto de Astrofísica de Andalucía (IAA-CSIC), Glorieta de la Astronomía s/n, 18008 Granada, Spain
[19] Institute for Astronomy, University of Hawai'i, 2680 Woodlawn Drive, Honolulu, HI 96822, USA
[20] APC, Univ Paris Diderot, CNRS/IN2P3, CEA/Irfu, Obs de Paris, Sorbonne Paris Cité, France
[21] AIM, CEA, CNRS, Université Paris-Saclay, Université Paris Diderot, Sorbonne Paris Cité, 91191 Gif-sur-Yvette, France
[22] The Oskar Klein Centre, Department of Astronomy, Stockholm University, AlbaNova 10691, Stockholm, Sweden
[23] Max-Planck-Institut für Extraterrestrische Physik, Giessenbachstraße 1, 85748 Garching, Germany
[24] INFN, Sezione di Padova, 35131 Padova, Italy
[25] Astrophysics Research Institute, IC2 building, Liverpool Science Park, 146 Brownlow Hill, Liverpool L3 5RF, UK
[26] Department of Physics, University of Warwick, Coventry CV4 7AL, UK
[27] INAF – Istituto di radioastronomia Bologna, Bologna, Italy
[28] ASI Science Data Centre, Via del Politecnico snc, 00133 Rome, Italy
[29] Faculty of Science, Department of Astronomy and Space Sciences, Istanbul University, Beyazıt, 34119 Istanbul, Turkey
[30] Department of Physics and Astronomy, University of Sheffield, Sheffield S3 7RH, UK

[31] Instituto de Astrofísica de Canarias, 38205 La Laguna, Tenerife, Spain
[32] Institute of Space Sciences (ICE, CSIC), Campus UAB, Carrer de Can Magrans s/n, 08193 Barcelona, Spain
[33] School of Physics and Astronomy, University of Leicester, University Road, Leicester LE1 7RH, UK
[34] Physics and Astronomy Department Galileo Galilei, University of Padova, Padova, Italy
[35] School of Physics, O'Brien Centre for Science North, University College Dublin, Belfield, Dublin 4, Ireland
[36] Cosmic Dawn Center (DAWN), Copenhagen Ø, Denmark
[37] Niels Bohr Institute, University of Copenhagen, Lyngbyvej 2, 2100 Copenhagen Ø, Denmark
[38] Departamento de Física Teórica y del Cosmos, Universidad de Granada, 18071 Granada, Spain
[39] Astrophysics Research Centre, School of Mathematics and Physics, Queen's University Belfast, Belfast BT7 1NN, UK
[40] University of Nova Gorica, Center for Astrophysics and Cosmology, Vipavska 13, 5000 Nova Gorica, Slovenia
[41] Institute of Astronomy, University of Cambridge, Madingley Road, Cambridge CB3 0HA, UK
[42] CENTRA-Centro de Astrofíisica e Gravitação and Departamento de Física, Instituto Superior Técnico, Universidade de Lisboa, Avenida Rovisco Pais, 1049-001 Lisboa, Portugal
[43] Università degli Studi di Urbino "Carlo Bo", 61029 Urbino, Italy
[44] INFN, Sezione di Firenze, 50019 Sesto Fiorentino, Firenze, Italy
[45] Astronomical Observatory, University of Warsaw, Al. Ujazdowskie 4, 00-478 Warszawa, Poland
[46] Department of Astrophysics/IMAPP, Radboud University, PO Box 9010, 6500 GL Nijmegen, The Netherlands
[47] Department of Astronomy, University of Cape Town, Private Bag X3, Rondebosch 7701, South Africa
[48] South African Astronomical Observatory, PO Box 9, Observatory 7935, South Africa
[49] The Inter-University Institute for Data Intensive Astronomy, University of Cape Town, Private Bag X3, Rondebosch 7701, South Africa
[50] Department of Physics and Astronomy, University of Southampton, Southampton SO17 1BJ, UK
[51] Department of Physics and Astronomy, University of Turku, Vesilinnantie 5, Turku 20014, Finland
[52] Centre for Astrophysics and Cosmology, Science Institute, University of Iceland, Dunhagi 5, 107 Reykjavík, Iceland
[53] School of Physics & Astronomy, Cardiff University, Queens Buildings, The Parade, Cardiff CF24 3AA, UK
[54] Anton Pannekoek Institute for Astronomy, University of Amsterdam, Science Park 904, 1098 XH Amsterdam, The Netherlands
[55] Key Laboratory of Dark Matter and Space Astronomy, Purple Mountain Observatory, Chinese Academy of Sciences, Nanjing 210008, PR China
[56] SRON, Netherlands Institute for Space Research, Sorbonnelaan 2, 3584 CA Utrecht, The Netherlands
[57] School of Physics and Astronomy, The University of Manchester, Manchester M13 9PL, UK
[58] Max-Planck-Institut für Astronomie, Königstuhl 17, 69117 Heidelberg, Germany
[59] Thüringer Landessternwarte Tautenburg, Sternwarte 5, 07778 Tautenburg, Germany
[60] Finnish Centre for Astronomy with ESO (FINCA), 20014 University of Turku, Finland
[61] DTU Space, National Space Institute, Technical University of Denmark, Elektrovej 327, 2800 Kongens Lyngby, Denmark
[62] Università degli Studi di Trieste and INFN, Sezione di Trieste, 34127 Trieste, Italy
[63] School of Physics, Trinity College Dublin, University of Dublin, College Green, Dublin 2, Ireland
[64] Institute for Gravitational Wave Astronomy and School of Physics and Astronomy, University of Birmingham, Edgbaston, Birmingham B15 2TT, UK
[65] Astronomical Observatory Institute, Faculty of Physics, Adam Mickiewicz University, ul. Słoneczna 36, 60-286 Poznań, Poland
[66] Institute of Cosmology and Gravitation, University of Portsmouth, Portsmouth PO1 3FX, UK
[67] Istituto di Astrofisica e Planetologia Spaziali (INAF), Via del Fosso del Cavaliere 100, Roma 00133, Italy
[68] Universitá di Pisa, Largo B. Pontecorvo 3, 56127 Pisa, Italy
[69] INFN – Sezione di Pisa, Largo B. Pontecorvo 3, 56127 Pisa, Italy
[70] Department of Physics, Trento University, Via Sommarive 14, 38123 Povo, Trento, Italy
[71] Departamento de Astrofísica, Universidad de La Laguna, 38206 La Laguna, Tenerife, Spain
[72] Departamento de Ciencias Fisicas, Universidad Andres Bello, Avda. Republica 252, Santiago, Chile
[73] National Astronomical Research Institute of Thailand, Ministry of Science and Technology, Chiang Mai 50180, Thailand
[74] INAF – Osservatorio Astronomico di Cagliari, Via della Scienza 5, 09047 Selargius, CA, Italy
[75] University of Cagliari, Dept of Physics, S.P. Monserrato-Sestu Km 0, 700, 09042 Monserrato, CA, Italy
[76] Dipartimento di Fisica e Astronomia "E. Majorana", Università degli studi di Catania, Via Santa Sofia 64, 95123 Catania, Italy
[77] INFN – Laboratori Nazionali del Sud, Via Santa Sofia 62, 95123 Catania, Italy
[78] INFN, Sezione di Napoli, Complesso Universitario di Monte S. Angelo, Via Cintia Edificio 6, 80126 Napoli, Italy
[79] Department of Physics, Via Cinthia, 80126 Fuorigrotta, Naples, Italy
[80] Armagh Observatory and Planetarium, Armagh BT61 9DG, UK
[81] Department of Physics and Astronomy, Johns Hopkins University, Baltimore, MD 21218, USA
[82] Institut für Astro- und Teilchenphysik, Universität Innsbruck, Technikerstrasse 25/8, 6020 Innsbruck, Austria
[83] The Oskar Klein Centre, Department of Physics, Stockholm University, AlbaNova, 10691 Stockholm, Sweden
[84] INAF – Istituto di Astrofisica Spaziale e Fisica Cosmica di Milano, Via A. Corti 12, 20133 Milano, Italy
[85] Physics Department, University of Calabria, Via P. Bucci, 87036 Rende, Italy
[86] European Southern Observatory, Alonso de Córdova, 3107, Vitacura, Santiago 763-0355, Chile
[87] Department of Physics, University of Bath, Bath BA2 7AY, UK
[88] Department of Physics, Harvard University, Cambridge, MA 02138, USA
[89] Department of Physics, The George Washington University, 725 21st Street NW, Washington, DC 20052, USA
[90] Astronomy, Physics, and Statistics Institute of Sciences (APSIS), The George Washington University, Washington, DC 20052, USA
[91] GEPI, Observatoire de Paris, PSL University, CNRS, 5 Place Jules Janssen, 92190 Meudon, France

Appendix A: From limiting magnitudes to limits in the model parameter space

For an EM counterpart model defined by an intrinsic light curve $\mathrm{d}L/\mathrm{d}\nu(\nu, t)$ (specific luminosity at a given rest-frame frequency ν, as a function of rest-frame post-merger time t), one can in principle use the galaxy-targeted and wide-field observations to exclude the presence of such emission in a given galaxy. We define here a framework that allows us to combine the results of different searches with a heterogeneous range of telescopes. We work under the simplifying assumption that each observation has a well-defined limiting flux, above which we can exclude a detection with high confidence.

A galaxy-targeted search consists of a set of observations of $N_{\rm gal}$ galaxies, each observed $N_{{\rm obs},i}$ times (i here runs on the galaxies). Each observation takes place at a time $t_{i,j}$ post-merger, and reaches a limiting flux $F_{{\rm lim},i,j}$ in a band whose central frequency is $\nu_{i,j}$. We can exclude that galaxy i hosted the putative EM counterpart as long as

$$F_{{\rm lim},i,j} < F_{{\rm model},i,j} = \frac{(1+z_i)}{4\pi d_{{\rm L},i}^2}\frac{\mathrm{d}L}{\mathrm{d}\nu}\left((1+z_i)\nu_{i,j}, \frac{t_{i,j}}{(1+z_i)}\right), \quad \text{(A.1)}$$

for any index j running over the $N_{{\rm obs},i}$ observations of that galaxy. In that case, the observations contribute a total of $P_{{\rm gal},i}$ to the confidence at which the particular EM counterpart model can be excluded. Formally, calling ξ the set of parameters and assumptions that define a particular EM counterpart model, we can exclude ξ with a confidence defined by

$$1 - P(\xi) = \sum_{i=1}^{N_{\rm gal}} P_{{\rm gal},i}\mathcal{E}_i(\xi), \quad \text{(A.2)}$$

with

$$\mathcal{E}_i(\xi) = 1 - \Pi_{j=1}^{N_{{\rm obs},i}}\mathrm{H}\left(F_{{\rm lim},i,j} - F_{\rm model}(\xi, \nu_{i,j}, t_{i,j})\right), \quad \text{(A.3)}$$

where H is the Heaviside step function. The quantity $\mathcal{E}_{i,j}(\xi)$ is 1 if at least one observation of galaxy i is constraining (i.e. it satisfies inequality reported in Eq. (A.1)), and 0 otherwise. In the absence of a detection, the quantity defined by Eq. (A.2) is most commonly referred to as the "covered probability" with respect to a particular source model.

In the case of a wide-field search, one can define the corresponding exclusion confidence as[23]

$$1 - P(\xi) = \sum_{i=1}^{N_{\rm tiles}} P_{{\rm tile},i}\int_0^\infty \mathrm{d}r\frac{\mathrm{d}P}{\mathrm{d}r}\mathcal{E}_i(r,\xi), \quad \text{(A.4)}$$

with

$$\mathcal{E}_i(r,\xi) = 1 - \Pi_{j=1}^{N_{{\rm obs},i}}\mathrm{H}\left(F_{{\rm lim},i,j} - F_{\rm model}(r,\xi,\nu_{i,j},t_{i,j})\right). \quad \text{(A.5)}$$

[23] For wide-field observations we assume the localisation probability density to follow the GW 3D skymap, that is, we do not distribute such probability to galaxies as in the galaxy-targeted search case. This relies on the assumption that the galaxy density averages out on scales as large as those probed by wide-field observations. Figure B.1 shows that this is a good approximation in our case, and this removes the uncertainty on the catalogue completeness.

Here the sum runs over a number $N_{\rm tiles}$ of non-overlapping sky tiles (e.g. a healpix tessellation), each observed $N_{{\rm obs},i}$ times, at epochs $t_{i,j}$, with limiting fluxes $F_{{\rm lim},i,j}$ in bands whose central frequencies are $\nu_{i,j}$. $P_{{\rm tile},i}$ is the (2D) skymap probability density integrated over the tile, while $\mathrm{d}P/\mathrm{d}r$ defines how this probability density is distributed over luminosity distance $r \equiv d_{\rm L}$ (i.e. sky-position-conditional distance probability density of the tile in the 3D skymap – Singer et al. 2016). Here $\mathcal{E}_i(r,\xi)$ equals 1 up to the distance beyond which the putative EM counterpart becomes too faint to be detected by the wide-field observations of tile i, and 0 for longer distances. This general framework allows for combining constraints from different wide-field searches.

The results from wide-field and galaxy-targeted searches can be combined conservatively by taking the most constraining between the two for each particular EM counterpart model.

Appendix B: Data tables

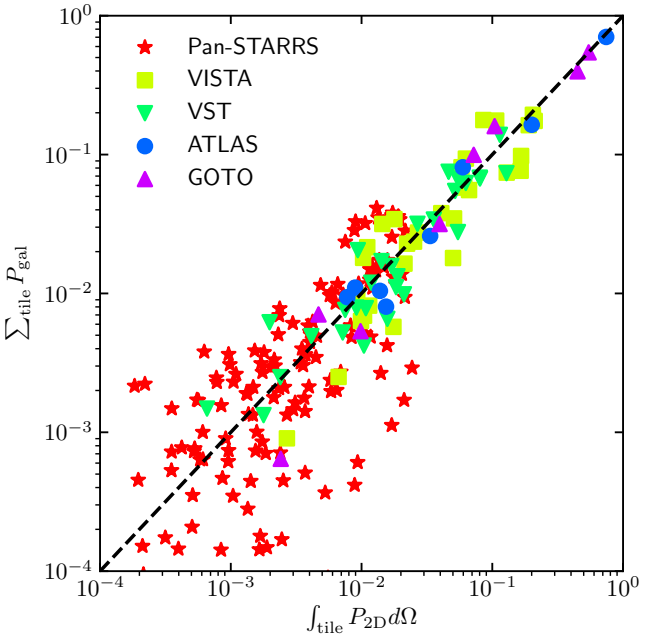

Fig. B.1. GW probability versus galaxy-weighted probability in wide-field observations. Comparison between the `LALInference` GW sky localisation probability density ($P_{\rm 2D}$) integrated over the tiles of our wide-field observations and the sum of individual galaxy probabilities $P_{\rm gal}$ (Sect. 3.7) over galaxies that fall in the same tile. The data are reported in Table B.2. Due to the wide field of view of these facilities, the galaxy density averages out, and the probabilities computed in the two ways are very similar. We note that the larger scatter for Pan-STARRS observations is due to the fact that observations are divided into smaller "sky cells". Grouping sky cells in the same observation would reduce the scatter.

In this appendix, we provide tables which list exhaustively both our galaxy-targeted (Table B.1) and wide-field (Table B.2) observations. Figure B.1 compares two different possible definitions of the probability contained in a wide-field observation, namely the `LALInference` sky localisation probability integrated over the observed tile, and the sum of the individual galaxy probabilities contained in the same tile, showing that the two are essentially equivalent in the case of wide-field observations.

Table B.1. Galaxies targeted in our search, in order of decreasing, combined, probability ($P_{3D} \times P_{gal}$).

Targeted galaxies								Observations of each galaxy			
Galaxy	RA (Deg)	Dec (Deg)	d_L (Mpc)	K_s (Vega)	$\log(L_K)$ ($L_\odot$)	P_{3D} (10^{-5}Mpc^{-3})	P_{gal}	Telescope/ Instrument	ΔT (days)	Band	m_{lim} (AB)
198197	12.091079	−25.126814	297.2	12.4	11.30	24.341	0.02607	LT/IO:O	0.20	r	20.3
								LT/IO:O	0.21	i	20.3
								VLT/HAWKI	1.37	K	22.3
								VLT/HAWKI	4.51	K	22.0
ESO474-035	13.173257	−25.733852	271.0	12.5	11.15	31.691	0.02402	LT/IO:O	0.26	r	20.3
								VLT/HAWKI	1.39	K	22.5
								VLT/HAWKI	4.54	K	21.5
797191	12.178233	−23.773075	253.9	12.3	11.22	24.334	0.02150	LT/IO:O	0.33	r	20.3
								VLT/HAWKI	1.35	K	22.4
								VLT/HAWKI	4.52	K	22.5
773232	12.793847	−25.954172	279.4	12.6	11.17	26.130	0.02098	WHT/ACAM	0.29	r	22.2
								VLT/FORS	1.40	i	24.0
IC1587	12.180364	−23.561686	195.8	11.4	11.35	13.990	0.01673	LT/IO:O	0.25	r	20.3
								LT/IO:O	0.26	i	20.3
								ESO2.2/GROND	0.35	K	18.0
								ESO2.2/GROND	0.35	r	21.0
								VLT/HAWKI	1.35	K	22.4
								VLT/HAWKI	4.49	K	22.5
2798981	13.803607	−26.330975	237.3	11.7	11.37	12.437	0.01585	VLT/HAWKI	1.42	K	21.4
								VLT/HAWKI	6.32	K	21.0
787700	12.874431	−24.642494	274.2	13.2	10.91	34.979	0.01535	LT/IO:O	0.22	r	20.3
								LT/IO:O	0.23	i	20.3
								WHT/ACAM	0.30	r	21.7
								VLT/FORS	1.43	i	23.5
2864	12.256170	−23.811317	233.7	12.6	11.02	25.547	0.01453	LT/IO:O	0.27	r	20.3
								LT/IO:O	0.27	i	20.3
								WHT/ACAM	0.28	r	20.7
								ESO2.2/GROND	0.44	K	18.5
								ESO2.2/GROND	0.44	r	21.0
								VLT/HAWKI	1.48	K	22.4
								VLT/HAWKI	4.52	K	22.0

Notes. For each galaxy we report: HyperLEDA name (except for those followed by 2MX in parentheses, which are from 2MASSX), right ascension, declination and luminosity distance as listed in the GLADE catalogue*, K_s-band magnitude as measured in our own VISTA/VINROUGE data, K_s-band luminosity, 3D skymap probability density per unit volume at the galaxy position, and localisation probability (Eq. (1)), followed by a list of observations of that galaxy, for which we specify the telescope, the post-merger time at which the observation was performed, the band, and the limiting magnitude. *The distances in GLADE are computed assuming a flat cosmology with $H_0 = 70\,\mathrm{km\,s^{-1}Mpc^{-1}}$ and $\Omega_m = 0.27$ (Dálya et al. 2018). The difference in luminosity distance when compared to our assumed cosmology ($H_0 = 70\,\mathrm{km\,s^{-1}Mpc^{-1}}$ and $\Omega_m = 0.30$) is <1 Mpc within 400 Mpc, but we anyway report the distance computed with our assumed cosmology.

Table B.1. continued.

Targeted galaxies								Observations of each galaxy			
Galaxy	RA (Deg)	Dec (Deg)	d_L (Mpc)	K_s (Vega)	$\log(L_K)$ ($L_\odot$)	P_{3D} (10^{-5}Mpc^{-3})	P_{gal}	Telescope/ Instrument	ΔT (days)	Band	m_{lim} (AB)
2694	11.543399	−24.650192	219.8	12.1	11.17	18.183	0.01448	LT/IO:O	0.24	r	20.3
								ESO2.2/GROND	0.50	K	18.0
								ESO2.2/GROND	0.50	r	20.0
								VLT/HAWKI	1.46	K	21.8
								VLT/HAWKI	6.34	K	21.0
769203	12.800914	−26.313063	262.8	12.6	11.09	20.970	0.01374	WHT/ACAM	0.29	r	22.5
								VLT/FORS	1.41	i	23.0
								WHT/LIRIS	3.27	K	20.0
133717	12.320091	−26.219179	330.6	12.1	11.52	7.504	0.01329	LT/IO:O	0.33	r	20.3
198196	11.870618	−25.440655	265.8	12.9	11.01	23.869	0.01301	ESO2.2/GROND	0.47	K	17.5
								ESO2.2/GROND	0.47	r	21.0
								VLT/HAWKI	1.41	K	22.5
								VLT/HAWKI	6.31	K	22.5
787067	13.064037	−24.698730	224.5	12.8	10.91	29.229	0.01289	WHT/ACAM	0.30	r	21.7
								WHT/LIRIS	2.32	K	20.0
3235517	12.103154	−25.595707	272.1	13.1	10.98	24.497	0.01249	WHT/LIRIS	2.29	K	20.0
798968	12.643789	−23.618547	227.8	12.4	11.07	19.656	0.01234	WHT/LIRIS	1.33	K	20.0
								VLT/FORS	1.34	i	23.5
								WHT/LIRIS	3.17	K	20.0
								WHT/LIRIS	3.17	K	20.0
2998	12.828166	−26.168060	285.2	13.0	11.02	21.414	0.01195	VLT/FORS	1.42	z	23.0
IC1588	12.740481	−23.557995	240.6	12.4	11.11	17.184	0.01187	VLT/FORS	1.34	i	24.0
								WHT/LIRIS	3.20	K	20.0
00485495-2504100 (2MX)	12.228970	−25.069471	240.6	13.1	10.84	31.409	0.01165	WHT/LIRIS	2.26	K	20.0
3235434	13.788131	−25.455704	229.5	12.6	11.01	20.751	0.01151	TNG/NICS	1.22	K	19.0
								VLT/FORS	1.46	i	24.0
								TNG/NICS	5.23	K	19.0
783013	13.656960	−25.067099	221.7	12.5	11.00	20.588	0.01117	WHT/ACAM	0.31	r	22.2
								TNG/NICS	1.25	K	19.0
								TNG/NICS	1.25	K	19.0
								WHT/LIRIS	1.26	K	20.0
								VLT/FORS	1.47	i	24.0
768450.0	13.722800	−26.381190	259.0	12.3	11.22	12.416	0.01100	VLT/HAWKI	1.42	K	21.4
								VLT/HAWKI	1.42	K	21.8
								VLT/HAWKI	6.32	K	21.0

Table B.1. continued.

Targeted galaxies								Observations of each galaxy			
Galaxy	RA (Deg)	Dec (Deg)	d_L (Mpc)	K_s (Vega)	$\log(L_K)$ ($L_\odot$)	P_{3D} (10^{-5}Mpc^{-3})	P_{gal}	Telescope/ Instrument	ΔT (days)	Band	m_{lim} (AB)
133715	12.441799	−26.443037	242.2	12.6	11.04	16.618	0.00975	LT/IO:O	0.34	*r*	20.3
								ESO2.2/GROND	0.45	*K*	18.5
								VLT/HAWKI	1.44	*K*	22.5
								VLT/HAWKI	6.36	*K*	22.5
3231	13.704722	−26.371256	236.5	12.3	11.14	13.226	0.00974	WHT/ACAM	0.31	*r*	21.4
								ESO2.2/GROND	0.40	*K*	17.5
								VLT/HAWKI	1.42	*K*	22.8
								VLT/HAWKI	1.42	*K*	21.8
								VLT/HAWKI	6.32	*K*	21.5
00530427-2610148 (2MX)	13.267828	−26.170792	243.0	13.1	10.87	23.859	0.00955	WHT/ACAM	0.31	*r*	22.0
788830	13.490571	−24.543142	295.8	13.1	11.04	15.322	0.00905	VLT/FORS	1.39	*i*	24.0
786964	12.473102	−24.707197	233.1	13.4	10.70	30.588	0.00820	WHT/ACAM	0.28	*r*	21.7
								WHT/LIRIS	1.22	*K*	20.0
								TNG/NICS	1.27	*K*	20.0
								VLT/FORS	1.35	*i*	24.0
								TNG/NICS	5.30	*K*	20.0
786999	13.269273	−24.704401	231.0	13.4	10.71	28.883	0.00800	LT/IO:O	0.29	*r*	20.3
792107	11.771893	−24.238703	291.8	13.3	10.94	17.133	0.00797	VLT/FORS	1.49	*i*	24.5
133716	12.364808	−26.538301	223.9	12.3	11.11	11.189	0.00778	ESO2.2/GROND	0.37	*K*	17.5
								ESO2.2/GROND	0.37	*r*	21.0
								VLT/HAWKI	1.44	*K*	22.8
								VLT/HAWKI	6.36	*K*	22.0
133702	12.242800	−25.693450	296.0	13.7	10.78	20.375	0.00658	TNG/NICS	1.23	*K*	20.0
								VLT/FORS	1.48	*i*	24.5
								TNG/NICS	5.26	*K*	20.0
100480	23.594837	−32.835316	286.2	11.3	11.72	2.269	0.00648	ESO2.2/GROND	0.34	*K*	19.0
								ESO2.2/GROND	0.34	*r*	20.5
133703	11.472051	−23.772461	234.2	12.6	11.00	11.794	0.00640	LT/IO:O	0.21	*r*	20.3
								LT/IO:O	0.22	*i*	20.3
								ESO2.2/GROND	0.49	*K*	19.0
								ESO2.2/GROND	0.49	*r*	21.0
								WHT/LIRIS	2.19	*K*	20.0
3264	13.806392	−26.321253	184.1	11.7	11.16	8.011	0.00623	ESO2.2/GROND	0.36	*K*	17.5
								ESO2.2/GROND	0.36	*r*	21.0
								VLT/HAWKI	1.42	*K*	21.4
								VLT/HAWKI	6.32	*K*	21.0

Table B.1. continued.

Targeted galaxies								Observations of each galaxy			
Galaxy	RA (Deg)	Dec (Deg)	d_L (Mpc)	K_s (Vega)	$\log(L_K)$ ($L_\odot$)	P_{3D} (10^{-5}Mpc^{-3})	P_{gal}	Telescope/ Instrument	ΔT (days)	Band	m_{lim} (AB)
101138	13.804421	−24.044033	203.1	11.8	11.21	7.085	0.00613	ESO2.2/GROND	0.52	*K*	19.5
								ESO2.2/GROND	0.52	*r*	22.0
771842	12.881038	−26.077213	294.6	14.0	10.69	19.981	0.00530	VLT/FORS	1.42	*z*	24.5
198221	12.385612	−26.538588	301.2	13.3	10.95	9.862	0.00473	VLT/HAWKI	1.44	*K*	22.3
								VLT/HAWKI	6.36	*K*	22.5
ESO474-036	13.192388	−22.975018	213.1	11.3	11.45	3.038	0.00459	ESO2.2/GROND	0.33	*K*	19.0
								ESO2.2/GROND	0.33	*r*	22.0
2947	12.666141	−26.813395	316.8	12.7	11.22	5.106	0.00455	WHT/ACAM	0.28	*r*	21.2
								ESO2.2/GROND	0.51	*K*	17.5
								ESO2.2/GROND	0.51	*r*	20.0
								TNG/NICS	1.29	*K*	20.0
								VLT/FORS	1.37	*i*	24.5
								TNG/NICS	5.33	*K*	20.0
198225	12.174922	−23.368631	329.4	12.9	11.17	5.247	0.00418	WHT/ACAM	0.27	*r*	22.0
802484	12.810972	−23.291632	268.2	13.2	10.91	8.806	0.00388	WHT/ACAM	0.30	*r*	22.0
804101	11.210597	−23.159029	222.7	12.5	11.00	6.527	0.00353	LT/IO:O	0.34	*r*	20.3
198205	12.540436	−23.280048	256.8	13.6	10.71	12.082	0.00337	WHT/LIRIS	3.23	*K*	20.0
133698	14.254662	−23.837297	221.6	12.2	11.11	4.664	0.00324	WHT/ACAM	0.32	*r*	22.5
								ESO2.2/GROND	0.38	*K*	19.0
								ESO2.2/GROND	0.38	*r*	21.0
198217	12.346334	−26.507498	298.9	13.8	10.74	10.667	0.00314	VLT/HAWKI	1.44	*K*	22.3
								VLT/HAWKI	6.36	*K*	22.0
142558	12.332034	−26.476397	253.3	13.8	10.59	14.724	0.00305	VLT/HAWKI	1.44	*K*	22.8
								VLT/HAWKI	6.36	*K*	22.0
101147	22.938530	−32.415623	240.8	12.0	11.27	2.868	0.00289	ESO2.2/GROND	0.44	*K*	19.0
								ESO2.2/GROND	0.44	*r*	21.0
798818	12.726862	−23.631887	316.2	13.9	10.76	9.227	0.00289	VLT/FORS	1.34	*i*	23.0
773323	12.467500	−25.946250	305.6	14.4	10.52	15.905	0.00287	WHT/LIRIS	3.30	*K*	20.0
805757	11.720657	−23.033381	249.3	13.6	10.66	10.878	0.00270	LT/IO:O	0.20	*r*	20.3
198201	12.637869	−23.295488	237.0	13.6	10.64	11.357	0.00266	LT/IO:O	0.32	*r*	20.3
795185	10.888593	−23.952913	307.3	13.2	11.02	4.174	0.00235	WHT/ACAM	0.27	*r*	22.5
								WHT/LIRIS	2.22	*K*	20.0
131961	23.018082	−33.802876	307.5	11.9	11.55	1.089	0.00208	ESO2.2/GROND	0.35	*K*	19.0
								ESO2.2/GROND	0.35	*r*	22.0
133690	10.639115	−22.866308	292.3	11.8	11.54	1.055	0.00199	WHT/ACAM	0.26	*r*	21.7
								ESO2.2/GROND	0.43	*K*	19.0
								ESO2.2/GROND	0.43	*r*	20.0
773149	12.815700	−25.960900	300.1	15.1	10.24	20.028	0.00189	VLT/FORS	1.40	*i*	24.5
PGC002953	12.679955	−22.888277	221.5	12.9	10.84	4.890	0.00183	WHT/ACAM	0.29	*r*	21.0

Table B.1. continued.

Targeted galaxies								Observations of each galaxy			
Galaxy	RA (Deg)	Dec (Deg)	d_L (Mpc)	K_s (Vega)	$\log(L_K)$ ($L_\odot$)	P_{3D} (10^{-5}Mpc^{-3})	P_{gal}	Telescope/ Instrument	ΔT (days)	Band	m_{lim} (AB)
131965	22.342892	−32.849354	228.0	12.1	11.19	1.922	0.00159	ESO2.2/GROND	0.41	*K*	19.0
								ESO2.2/GROND	0.41	*r*	21.0
IC1581	11.442945	−25.920193	222.0	13.0	10.81	4.485	0.00155	LT/IO:O	0.29	*r*	20.3
								ESO2.2/GROND	0.42	*K*	18.0
								ESO2.2/GROND	0.42	*r*	22.0
684102	22.549915	−32.903667	292.0	12.8	11.11	1.651	0.00115	ESO2.2/GROND	0.48	*K*	19.0
								ESO2.2/GROND	0.48	*r*	21.0
131958	24.334146	−33.330853	232.2	12.6	11.01	2.003	0.00109	ESO2.2/GROND	0.38	*K*	19.0
								ESO2.2/GROND	0.38	*r*	21.0
777373.0	12.718400	−25.577060	225.6	16.0	9.61	27.183	0.00060	LT/IO:O	0.32	*r*	20.3
ESO540-029	12.120861	−22.147444	220.1	13.4	10.67	1.513	0.00038	ESO2.2/GROND	0.46	*K*	18.0
								ESO2.2/GROND	0.46	*r*	21.0
ESO540-013	10.242757	−22.083128	286.5	12.5	11.24	0.398	0.00037	ESO2.2/GROND	0.32	*K*	18.0
								ESO2.2/GROND	0.32	*r*	19.0
								LT/IO:O	0.35	*r*	20.3
95210	22.145348	−32.296467	288.3	14.0	10.62	1.587	0.00036	ESO2.2/GROND	0.55	*K*	19.0
								ESO2.2/GROND	0.55	*r*	21.0
131959	23.877426	−32.970612	288.2	14.4	10.49	2.018	0.00034	ESO2.2/GROND	0.43	*K*	19.5
								ESO2.2/GROND	0.43	*r*	20.0
ESO474-026	11.781363	−24.370647	114.9	11.1	10.98	0.516	0.00027	LT/IO:O	0.24	*r*	20.3
								LT/IO:O	0.25	*i*	20.3
								ESO2.2/GROND	0.33	*K*	18.5
								ESO2.2/GROND	0.33	*r*	20.0
								VLT/HAWKI	1.34	*K*	22.4
								VLT/HAWKI	6.28	*K*	22.5
172818	11.202063	−22.116533	288.6	13.8	10.72	0.713	0.00020	WHT/ACAM	0.27	*r*	21.2
2561	10.676272	−21.774082	148.9	13.8	10.14	0.274	0.00002	LT/IO:O	0.19	*r*	20.3

Table B.2. Wide-field observations.

Facility	Tile ID	$\int_{\text{tile}} P_{\text{2D}}\, d\Omega$ [%]	$\sum_{\text{tile}} P_{\text{gal}}$ [%]	RA [deg]	Dec [deg]	MJD	Filter	Limiting mag [AB]
VST	0	1.692	1.578	10.573625	−23.734472	58711.36	*r*	21.90
						58715.36	*r*	21.60
						58717.36	*r*	22.00
						58724.36	*r*	22.10
VST	1	1.421	1.710	10.558375	−24.729083	58711.36	*r*	20.90
						58715.36	*r*	21.50
						58717.36	*r*	22.10
						58724.36	*r*	22.20
VST	2	0.413	0.493	10.558333	−25.724028	58711.36	*r*	22.00
						58715.36	*r*	22.10
						58717.36	*r*	21.80
						58724.36	*r*	21.90
VST	3	0.048	0.000	10.959208	−20.706361	58710.36	*r*	20.10
VST	4	0.198	0.620	10.959167	−21.706333	58710.36	*r*	20.60
VST	5	1.187	1.194	10.959125	−22.706306	58710.36	*r*	21.90
VST	6	1.835	1.110	11.295375	−22.736917	58711.36	*r*	21.80
						58715.36	*r*	22.10
						58717.36	*r*	22.10
						58724.36	*r*	22.30
VST	7	8.051	6.725	11.639292	−24.731056	58710.36	*r*	20.70
						58711.36	*r*	21.00
						58714.36	*r*	21.70
						58717.36	*r*	21.90
						58725.36	*r*	22.00
VST	8	5.198	5.474	11.630167	−25.731028	58710.36	*r*	20.60
						58711.36	*r*	20.90
						58714.36	*r*	21.60
						58717.36	*r*	22.10
						58725.36	*r*	22.20
VST	9	1.575	0.656	11.599125	−26.719083	58711.36	*r*	22.20
						58714.36	*r*	21.50
						58717.36	*r*	22.10
						58725.36	*r*	22.40
VST	10	5.458	6.723	11.647958	−23.731083	58710.36	*r*	21.50
						58711.36	*r*	21.80
						58715.36	*r*	22.10
						58717.36	*r*	21.20
						58725.36	*r*	22.00
VST	11	0.239	0.250	12.035458	−21.706333	58710.36	*r*	20.20
VST	12	2.109	0.986	12.043125	−22.706306	58710.36	*r*	21.00
VST	13	1.882	1.330	12.368625	−22.736861	58711.36	*r*	22.20
						58715.36	*r*	22.20
						58717.36	*r*	22.30
						58724.36	*r*	22.20
VST	14	8.029	6.823	12.740292	−23.731083	58715.36	*r*	21.30
						58717.36	*r*	21.60
						58725.36	*r*	22.20
VST	15	12.833	7.345	12.740250	−24.731056	58710.36	*r*	21.40
						58711.36	*r*	21.90
						58714.36	*r*	21.70
						58717.36	*r*	21.80
						58725.36	*r*	22.00
VST	16	11.429	13.867	12.740208	−25.731028	58710.36	*r*	21.00
						58711.36	*r*	21.80
						58714.36	*r*	21.70
						58717.36	*r*	21.90
						58725.36	*r*	21.80
VST	17	4.633	7.519	12.709542	−26.719111	58711.36	*r*	21.80
						58714.36	*r*	21.40
						58717.36	*r*	21.70
						58725.36	*r*	21.90
VST	18	0.750	0.761	12.814125	−27.714861	58711.36	*r*	22.00
						58714.36	*r*	21.90
						58717.36	*r*	21.40
						58725.36	*r*	22.10

Notes. For each facility we report a list of unique tiles, identified by a Tile ID and by the RA and Dec of the tile centre, along with the `LALInference` sky location probability density (P_{2D}) integrated over the solid angle subtended by the tile, and the sum of the galaxy probabilities P_{gal} over galaxies that fall within the tile (see Fig. B.1 for a comparison plot). For each tile, we then report the MJD, Filter and Limiting magnitude of the observations carried out of these tiles.

Table B.2. continued.

Facility	Tile ID	$\int_{\rm tile} P_{\rm 2D}\,{\rm d}\Omega$ [%]	$\sum_{\rm tile} P_{\rm gal}$ [%]	RA [deg]	Dec [deg]	MJD	Filter	Limiting mag [AB]
VST	19	0.936	2.050	13.441833	−22.736889	58711.36	*r*	21.90
						58715.36	*r*	21.90
						58717.36	*r*	22.00
						58725.36	*r*	22.00
VST	20	2.676	3.173	13.832625	−23.731083	58710.36	*r*	21.50
						58715.36	*r*	21.70
						58717.36	*r*	21.70
						58725.36	*r*	21.80
VST	21	5.460	2.766	13.841208	−24.731056	58710.36	*r*	21.10
						58715.36	*r*	21.90
						58717.36	*r*	21.60
						58725.36	*r*	22.10
VST	22	3.573	3.406	13.810042	−26.719333	58711.36	*r*	21.80
						58714.36	*r*	21.40
						58717.36	*r*	21.70
						58725.36	*r*	22.10
VST	23	6.271	6.244	13.850250	−25.731028	58710.36	*r*	19.90
						58711.36	*r*	20.90
						58714.36	*r*	21.90
						58717.36	*r*	22.00
						58725.36	*r*	22.10
VST	24	1.078	0.784	13.930083	−27.711639	58711.36	*r*	21.90
						58714.36	*r*	21.40
						58717.36	*r*	21.80
						58725.36	*r*	21.90
VST	25	0.718	0.523	14.917500	−24.748889	58711.36	*r*	21.80
						58714.36	*r*	21.80
						58717.36	*r*	21.70
						58725.36	*r*	22.10
VST	26	1.043	0.421	14.917042	−25.728472	58714.36	*r*	21.80
						58714.36	*r*	21.80
						58717.36	*r*	21.90
						58725.36	*r*	22.00
VST	27	0.913	0.791	14.901708	−26.715667	58711.36	*r*	22.00
						58714.36	*r*	21.30
						58717.36	*r*	21.70
						58725.36	*r*	22.00
VST	28	0.066	0.148	9.882875	−21.706333	58710.36	*r*	20.80
VST	29	0.178	0.133	9.875167	−22.706306	58710.36	*r*	21.90
VISTA	0	0.667	0.250	25.095850	−32.299140	58712.32	*K*	21.00
						58719.37	*K*	21.00
						58750.36	*K*	21.00
VISTA	1	1.442	3.164	23.948508	−33.391240	58712.28	*K*	21.00
						58719.33	*K*	21.00
						58751.22	*K*	21.00
VISTA	2	0.269	0.090	24.730321	−31.206940	58712.36	*K*	21.00
						58719.41	*K*	21.00
						58751.34	*K*	21.00
VISTA	3	1.784	3.429	23.445350	−32.299140	58712.31	*K*	21.00
						58719.36	*K*	21.00
						58751.23	*K*	21.00
VISTA	4	1.028	1.804	22.244808	−33.391240	58712.27	*K*	21.00
						58719.32	*K*	21.00
						58751.21	*K*	21.00
						58751.31	*K*	21.00
VISTA	5	0.927	0.974	23.228521	−31.206940	58712.34	*K*	21.00
						58712.39	*K*	21.00
						58719.40	*K*	21.00
						58751.33	*K*	21.00
VISTA	6	1.044	0.691	22.635321	−31.206940	58712.33	*K*	21.00
						58719.38	*K*	21.00
						58750.37	*K*	21.00
VISTA	7	1.106	2.153	21.729250	−32.299140	58712.29	*K*	21.00
						58719.35	*K*	21.00
						58751.32	*K*	21.00
VISTA	8	1.753	0.574	14.469058	−27.491250	58714.22	*K*	21.00
						58720.40	*K*	21.00
						58752.28	*K*	21.00
VISTA	9	6.639	5.550	14.012971	−26.491250	58711.20	*K*	21.00
						58719.23	*K*	21.00
						58750.32	*K*	21.00

Table B.2. continued.

Facility	Tile ID	$\int_{\text{tile}} P_{\text{2D}}\, d\Omega$ [%]	$\sum_{\text{tile}} P_{\text{gal}}$ [%]	RA [deg]	Dec [deg]	MJD	Filter	Limiting mag [AB]
VISTA	10	5.010	1.799	14.489817	−25.399150	58712.17	*K*	21.00
						58720.23	*K*	21.00
						58750.12	*K*	21.00
VISTA	11	1.144	0.817	14.972704	−24.306950	58712.22	*K*	21.00
						58720.27	*K*	21.00
						58751.26	*K*	21.00
VISTA	12	2.520	2.361	12.988658	−27.491250	58714.21	*K*	21.00
						58720.28	*K*	21.00
						58752.20	*K*	21.00
VISTA	13	10.706	17.574	13.227671	−26.491250	58711.19	*K*	21.00
						58719.22	*K*	21.00
						58750.31	*K*	21.00
VISTA	14	5.098	3.471	14.252400	−24.441050	58712.40	*K*	21.00
						58720.38	*K*	21.00
						58751.37	*K*	21.00
VISTA	15	20.441	19.345	13.004717	−25.399150	58711.40	*K*	21.00
						58720.22	*K*	21.00
						58750.11	*K*	21.00
VISTA	16	2.230	2.282	14.070646	−23.348850	58714.18	*K*	21.00
						58720.37	*K*	21.00
						58752.18	*K*	21.00
VISTA	17	8.540	17.738	12.256171	−26.491250	58711.18	*K*	21.00
						58719.21	*K*	21.00
						58750.29	*K*	21.00
VISTA	18	12.904	7.413	13.439304	−24.306950	58712.21	*K*	21.00
						58720.26	*K*	21.00
						58751.25	*K*	21.00
VISTA	19	16.476	7.644	13.266400	−24.441050	58712.37	*K*	21.00
						58720.35	*K*	21.00
						58751.36	*K*	21.00
VISTA	20	0.990	0.634	11.821058	−27.491250	58714.20	*K*	21.00
						58719.18	*K*	21.00
						58752.05	*K*	21.00
						58752.10	*K*	21.00
						58752.12	*K*	21.00
VISTA	21	21.098	17.478	12.748617	−25.399150	58711.24	*K*	21.00
						58711.26	*K*	21.00
						58711.27	*K*	21.00
						58711.28	*K*	21.00
						58711.29	*K*	21.00
						58711.30	*K*	21.00
						58711.35	*K*	21.00
						58711.36	*K*	21.00
						58711.38	*K*	21.00
						58711.39	*K*	21.00
						58719.26	*K*	21.00
						58719.27	*K*	21.00
						58719.29	*K*	21.00
						58719.42	*K*	21.00
						58720.15	*K*	21.00
						58720.16	*K*	21.00
						58720.17	*K*	21.00
						58720.18	*K*	21.00
						58720.19	*K*	21.00
						58720.21	*K*	21.00
						58750.35	*K*	21.00
						58751.07	*K*	21.00
						58751.08	*K*	21.00
						58751.11	*K*	21.00
						58751.12	*K*	21.00
						58751.13	*K*	21.00
						58751.14	*K*	21.00
						58751.16	*K*	21.00
						58751.17	*K*	21.00
						58751.18	*K*	21.00
						58751.19	*K*	21.00
VISTA	22	5.813	8.108	13.273946	−23.348850	58714.17	*K*	21.00
						58720.36	*K*	21.00
						58751.38	*K*	21.00
VISTA	23	18.996	16.287	12.246717	−25.399150	58711.23	*K*	21.00
						58719.25	*K*	21.00
						58751.10	*K*	21.00

Table B.2. continued.

Facility	Tile ID	$\int_{\rm tile} P_{\rm 2D}\,{\rm d}\Omega$ [%]	$\sum_{\rm tile} P_{\rm gal}$ [%]	RA [deg]	Dec [deg]	MJD	Filter	Limiting mag [AB]
VISTA	24	2.131	1.639	11.191771	−26.491250	58711.17	*K*	21.00
						58719.14	*K*	21.00
						58750.27	*K*	21.00
						58750.28	*K*	21.00
VISTA	25	16.608	9.775	11.966904	−24.306950	58712.20	*K*	21.00
						58720.24	*K*	21.00
						58750.15	*K*	21.00
VISTA	26	4.070	3.787	10.946017	−25.399150	58711.22	*K*	21.00
						58719.16	*K*	21.00
						58750.33	*K*	21.00
VISTA	27	6.280	9.353	11.613746	−23.214750	58712.25	*K*	21.00
						58720.33	*K*	21.00
						58751.28	*K*	21.00
VISTA	28	6.106	5.785	10.890504	−24.306950	58712.18	*K*	21.00
						58719.17	*K*	21.00
						58750.14	*K*	21.00
						58750.16	*K*	21.00
VISTA	29	2.701	2.745	10.778046	−23.214750	58712.24	*K*	21.00
						58719.20	*K*	21.00
						58751.27	*K*	21.00
Pan-STARRS	0	0.020	0.000	15.543640	−26.588360	58710.58	*z*	19.65
						58710.59	*i*	20.30
Pan-STARRS	1	0.067	0.000	15.195180	−26.989770	58710.57	*z*	19.21
						58710.57	*i*	20.26
Pan-STARRS	2	0.032	0.000	15.550540	−26.186890	58710.59	*i*	20.26
						58710.59	*z*	19.90
Pan-STARRS	3	0.001	0.000	16.007700	−25.389260	58710.57	*z*	19.41
						58710.59	*i*	20.07
Pan-STARRS	4	0.050	0.000	14.751030	−27.396890	58710.57	*i*	20.23
						58710.58	*z*	19.77
Pan-STARRS	5	0.058	0.000	15.188230	−26.588360	58710.58	*z*	20.04
						58710.59	*i*	20.48
Pan-STARRS	6	0.035	0.000	15.557400	−25.785410	58710.59	*i*	20.27
						58710.59	*z*	19.95
Pan-STARRS	7	0.174	0.085	14.745580	−26.995480	58710.58	*i*	20.44
						58710.59	*z*	20.08
Pan-STARRS	8	0.155	0.074	14.303600	−27.802590	58710.59	*z*	19.87
Pan-STARRS	9	0.058	0.064	15.181320	−26.186890	58710.58	*z*	20.06
						58710.59	*i*	20.38
Pan-STARRS	10	0.013	0.000	15.564210	−25.383940	58710.58	*i*	20.20
						58710.58	*z*	20.03
Pan-STARRS	11	0.218	0.301	14.740170	−26.593980	58710.58	*i*	20.51
						58710.59	*z*	20.23
Pan-STARRS	12	0.057	0.000	13.898950	−28.191420	58710.58	*z*	19.93
Pan-STARRS	13	0.165	0.014	14.299680	−27.401250	58710.58	*z*	19.90
Pan-STARRS	14	0.106	0.003	15.174460	−25.785400	58710.58	*i*	20.55
						58710.59	*z*	20.26
Pan-STARRS	15	0.013	0.000	15.570980	−24.982530	58710.58	*i*	20.26
						58710.59	*z*	20.10
Pan-STARRS	16	0.252	0.045	14.295780	−26.999770	58710.58	*i*	20.34
						58710.59	*z*	20.20
Pan-STARRS	17	0.158	0.101	14.734800	−26.192410	58710.58	*i*	20.63
						58710.58	*z*	20.46
Pan-STARRS	18	0.168	0.018	13.850540	−27.805550	58710.58	*z*	20.03
Pan-STARRS	19	0.078	0.247	15.167650	−25.383940	58710.58	*i*	20.54
						58710.59	*z*	20.43
Pan-STARRS	20	0.004	0.000	13.441750	−28.593110	58710.57	*z*	19.83
Pan-STARRS	21	0.016	0.000	15.577690	−24.581220	58710.57	*z*	19.74
						58710.58	*i*	19.79
Pan-STARRS	22	0.370	0.142	14.291920	−26.598190	58710.58	*i*	20.67
						58710.59	*z*	20.48
Pan-STARRS	23	0.189	0.015	14.729460	−25.790820	58710.58	*i*	20.73
						58710.59	*z*	20.48
Pan-STARRS	24	0.343	0.318	13.848190	−27.404160	58710.58	*z*	20.08
Pan-STARRS	25	0.050	0.000	13.442660	−28.191420	58710.58	*z*	20.14
Pan-STARRS	26	0.052	0.000	15.160890	−24.982530	58710.58	*i*	20.64
						58710.58	*z*	20.54
Pan-STARRS	27	0.012	0.000	15.584370	−24.180040	58710.58	*z*	19.75
						58710.59	*i*	20.19
Pan-STARRS	28	0.373	0.363	14.288080	−26.196550	58710.58	*i*	20.76
						58710.58	*z*	20.50

Table B.2. continued.

Facility	Tile ID	$\int_{\rm tile} P_{\rm 2D}\,{\rm d}\Omega$ [%]	$\sum_{\rm tile} P_{\rm gal}$ [%]	RA [deg]	Dec [deg]	MJD	Filter	Limiting mag [AB]
Pan-STARRS	29	0.554	0.009	13.845850	−27.002630	58710.58	*i*	20.51
						58710.59	*z*	20.28
Pan-STARRS	30	0.213	0.178	14.724160	−25.389260	58710.58	*i*	20.79
						58710.59	*z*	20.66
Pan-STARRS	31	0.134	0.188	13.397400	−27.807030	58710.58	*z*	20.10
Pan-STARRS	32	0.025	0.000	15.154170	−24.581210	58710.58	*i*	20.47
						58710.58	*z*	20.58
Pan-STARRS	33	0.002	0.000	12.983670	−28.591570	58710.58	*z*	19.60
Pan-STARRS	34	0.520	0.007	14.284260	−25.794890	58710.58	*i*	20.89
						58710.59	*z*	20.70
						58713.54	*z*	21.03
						58716.55	*z*	22.02
Pan-STARRS	35	0.646	0.201	13.843530	−26.601000	58710.58	*i*	20.86
						58710.58	*z*	20.50
Pan-STARRS	36	0.174	0.000	14.718890	−24.987750	58710.58	*i*	20.80
						58710.59	*z*	20.74
Pan-STARRS	37	0.215	0.333	13.396610	−27.405610	58710.57	*i*	20.03
						58710.59	*z*	20.11
Pan-STARRS	38	0.019	0.000	15.147490	−24.180040	58710.58	*z*	20.37
						58710.59	*i*	20.41
Pan-STARRS	39	0.021	0.009	12.986410	−28.189910	58710.58	*z*	20.00
Pan-STARRS	40	0.751	2.351	13.841230	−26.199310	58710.58	*i*	20.95
						58710.58	*z*	20.68
						58713.54	*z*	21.43
						58716.54	*z*	22.53
Pan-STARRS	41	0.527	0.037	14.280480	−25.393250	58710.58	*i*	21.03
						58710.59	*z*	20.87
						58713.55	*z*	21.65
						58716.54	*z*	22.71
Pan-STARRS	42	0.121	0.000	14.713660	−24.586340	58710.58	*i*	20.82
						58710.59	*z*	20.82
Pan-STARRS	43	0.561	0.000	13.395830	−27.004060	58710.57	*i*	20.53
						58710.59	*z*	20.26
Pan-STARRS	44	0.007	0.000	15.163950	−23.793450	58710.57	*z*	20.10
						58710.59	*i*	20.33
Pan-STARRS	45	0.110	0.262	12.944230	−27.807030	58710.58	*z*	20.17
Pan-STARRS	46	1.053	0.000	13.838940	−25.797610	58710.58	*i*	21.05
						58710.59	*z*	20.79
						58713.54	*z*	21.76
						58716.54	*z*	22.97
Pan-STARRS	47	0.422	0.001	14.276710	−24.991670	58710.58	*i*	21.08
						58710.58	*z*	20.91
						58713.54	*z*	21.82
						58716.54	*z*	22.81
Pan-STARRS	48	0.824	0.587	13.395060	−26.602410	58710.58	*i*	20.96
						58710.59	*z*	20.44
						58713.53	*z*	20.96
						58716.53	*z*	21.73
Pan-STARRS	49	0.098	0.308	14.708470	−24.185070	58710.58	*i*	20.71
						58710.59	*z*	20.69
Pan-STARRS	50	0.001	0.000	15.169610	−23.392540	58710.57	*z*	19.93
						58710.58	*i*	20.14
Pan-STARRS	51	0.234	0.207	12.945010	−27.405610	58710.57	*i*	20.18
						58710.59	*z*	20.16
Pan-STARRS	52	0.014	0.000	12.530240	−28.186880	58710.58	*z*	20.06
Pan-STARRS	53	0.037	0.000	14.836120	−23.793450	58710.58	*z*	20.40
						58710.59	*i*	20.46
Pan-STARRS	54	1.156	1.253	13.836660	−25.395920	58710.58	*i*	21.18
						58710.59	*z*	20.97
						58713.54	*z*	21.94
						58716.54	*z*	23.05
Pan-STARRS	55	0.370	0.051	14.272980	−24.590190	58710.58	*z*	20.89
						58710.58	*i*	20.96
						58713.54	*z*	21.77
						58716.54	*z*	22.69
Pan-STARRS	56	1.158	1.492	13.394290	−26.200690	58710.58	*i*	20.96
						58710.59	*z*	20.67
						58713.55	*z*	21.69
						58716.54	*z*	22.94
Pan-STARRS	57	0.487	1.146	12.945790	−27.004060	58710.58	*i*	20.51
						58710.59	*z*	20.26

Table B.2. continued.

Facility	Tile ID	$\int_{\rm tile} P_{\rm 2D}\,{\rm d}\Omega$ [%]	$\sum_{\rm tile} P_{\rm gal}$ [%]	RA [deg]	Dec [deg]	MJD	Filter	Limiting mag [AB]
Pan-STARRS	58	0.048	0.000	12.491080	−27.805550	58710.58	z	20.13
Pan-STARRS	59	0.010	0.000	14.830470	−23.392540	58710.58	z	20.27
						58710.59	i	20.38
Pan-STARRS	60	0.950	1.176	13.834410	−24.994290	58710.58	i	21.13
						58710.59	z	20.98
						58713.54	z	22.05
						58716.54	z	23.03
Pan-STARRS	61	1.709	3.652	13.393530	−25.798960	58710.58	i	21.05
						58710.59	z	20.77
						58713.54	z	21.81
						58716.54	z	23.12
Pan-STARRS	62	0.350	0.399	14.269270	−24.188850	58710.58	i	20.90
						58710.59	z	20.85
						58713.53	z	21.20
						58716.53	z	22.15
Pan-STARRS	63	0.866	0.929	12.946560	−26.602410	58710.58	z	20.35
						58710.58	i	20.80
						58713.54	z	21.50
						58716.54	z	22.56
Pan-STARRS	64	0.180	0.377	14.396600	−23.798430	58710.58	z	20.68
						58710.58	i	20.72
Pan-STARRS	65	0.148	0.133	12.493430	−27.404160	58710.57	i	19.80
						58710.58	z	20.16
Pan-STARRS	66	0.001	0.000	14.824850	−22.991490	58710.57	z	19.79
						58710.58	i	20.13
Pan-STARRS	67	0.003	0.000	12.074210	−28.182340	58710.58	z	19.99
Pan-STARRS	68	0.779	0.000	13.832160	−24.592760	58710.58	i	21.12
						58710.59	z	20.91
						58713.54	z	22.01
						58716.54	z	23.00
Pan-STARRS	69	1.912	3.586	13.392770	−25.397250	58710.59	i	21.05
						58710.59	z	20.94
						58713.54	z	22.02
						58716.54	z	23.12
Pan-STARRS	70	1.337	3.513	12.947330	−26.200690	58710.58	i	21.03
						58710.59	z	20.69
						58713.54	z	21.85
						58716.54	z	23.04
Pan-STARRS	71	0.403	0.529	12.495770	−27.002630	58710.58	i	20.06
						58710.59	z	20.24
Pan-STARRS	72	0.061	0.000	14.392200	−23.397430	58710.59	i	20.70
						58710.59	z	20.50
Pan-STARRS	73	1.567	0.422	13.392020	−24.995600	58710.58	i	21.09
						58710.59	z	20.93
						58713.54	z	22.06
						58716.54	z	23.07
Pan-STARRS	74	0.040	0.014	12.038020	−27.802590	58710.58	z	20.11
Pan-STARRS	75	0.593	1.017	13.829940	−24.191370	58710.58	i	20.98
						58710.59	z	20.94
						58713.54	z	21.93
						58716.54	z	22.95
Pan-STARRS	76	1.958	3.408	12.948090	−25.798960	58710.58	i	20.92
						58710.59	z	20.69
						58713.54	z	22.00
						58716.54	z	23.14
Pan-STARRS	77	0.883	2.847	12.498090	−26.601000	58710.58	i	20.68
						58710.59	z	20.32
						58713.55	z	21.45
						58716.54	z	22.53
Pan-STARRS	78	0.408	0.506	13.956890	−23.802170	58710.59	i	20.90
						58710.59	z	20.88
						58713.53	z	21.26
						58716.53	z	22.14
Pan-STARRS	79	0.011	0.000	14.387820	−22.996290	58710.58	z	20.31
						58710.58	i	20.44
Pan-STARRS	80	0.104	0.035	12.041940	−27.401250	58710.57	i	19.99
						58710.59	z	20.16
Pan-STARRS	81	1.578	1.734	13.391270	−24.594050	58710.58	i	21.25
						58710.59	z	20.98
						58713.54	z	22.01
						58716.54	z	23.04

Table B.2. continued.

Facility	Tile ID	$\int_{\text{tile}} P_{\text{2D}}\,\mathrm{d}\Omega$ [%]	$\sum_{\text{tile}} P_{\text{gal}}$ [%]	RA [deg]	Dec [deg]	MJD	Filter	Limiting mag [AB]
Pan-STARRS	82	2.434	0.291	12.948850	−25.397250	58710.58	*i*	21.09
						58710.59	*z*	20.95
						58713.54	*z*	21.95
						58716.54	*z*	23.19
Pan-STARRS	83	1.205	1.573	12.500390	−26.199310	58710.58	*i*	20.92
						58710.59	*z*	20.56
						58713.54	*z*	21.92
						58716.54	*z*	23.05
Pan-STARRS	84	0.202	0.295	13.953750	−23.401100	58710.59	*i*	20.85
						58710.59	*z*	20.67
Pan-STARRS	85	0.257	0.211	12.045840	−26.999770	58710.58	*i*	20.01
						58710.60	*z*	20.17
Pan-STARRS	86	0.000	0.000	14.383480	−22.595060	58710.57	*z*	19.93
Pan-STARRS	87	1.174	0.487	13.390530	−24.192630	58710.58	*i*	21.07
						58710.59	*z*	20.91
						58713.54	*z*	22.04
						58716.54	*z*	23.06
Pan-STARRS	88	2.090	0.001	12.949600	−24.995600	58710.58	*i*	21.16
						58710.59	*z*	20.97
						58713.54	*z*	22.10
						58716.54	*z*	23.12
Pan-STARRS	89	1.708	2.546	12.502680	−25.797610	58710.58	*i*	21.04
						58710.59	*z*	20.68
						58713.54	*z*	22.12
						58716.54	*z*	23.10
Pan-STARRS	90	0.004	0.000	11.585110	−27.798160	58710.58	*z*	19.86
Pan-STARRS	91	0.585	0.197	13.517060	−23.804660	58710.58	*i*	20.99
						58710.59	*z*	20.91
						58713.54	*z*	21.83
						58716.54	*z*	22.89
Pan-STARRS	92	0.084	0.000	13.950630	−22.999890	58710.59	*i*	20.90
						58710.59	*z*	20.69
Pan-STARRS	93	0.578	0.237	12.049700	−26.598190	58710.58	*i*	20.46
						58710.60	*z*	20.27
						58713.56	*z*	20.92
						58716.56	*z*	21.73
Pan-STARRS	94	2.162	2.823	12.950350	−24.594050	58710.58	*i*	21.23
						58710.59	*z*	20.99
						58713.54	*z*	22.11
						58716.54	*z*	23.16
Pan-STARRS	95	2.117	0.171	12.504960	−25.395920	58710.58	*i*	21.05
						58710.59	*z*	20.82
						58713.54	*z*	22.21
						58716.54	*z*	23.20
Pan-STARRS	96	0.056	0.170	11.590590	−27.396890	58710.58	*i*	19.93
						58710.59	*z*	19.95
Pan-STARRS	97	0.396	0.213	13.515170	−23.403550	58710.59	*i*	21.01
						58710.59	*z*	20.77
						58716.52	*z*	21.37
Pan-STARRS	98	0.933	0.061	12.053540	−26.196550	58710.58	*i*	20.80
						58710.59	*z*	20.37
						58713.54	*z*	21.86
						58716.54	*z*	22.97
Pan-STARRS	99	0.018	0.000	13.947520	−22.598590	58710.58	*i*	20.41
						58710.59	*z*	20.27
Pan-STARRS	100	1.936	0.000	12.951090	−24.192630	58710.58	*i*	21.19
						58710.59	*z*	21.00
						58713.54	*z*	22.09
						58716.54	*z*	23.15
Pan-STARRS	101	0.137	0.135	11.596040	−26.995480	58710.59	*i*	20.03
						58710.60	*z*	20.07
Pan-STARRS	102	2.033	1.379	12.507210	−24.994290	58710.58	*i*	21.15
						58710.59	*z*	20.93
						58713.54	*z*	22.09
						58716.54	*z*	23.14
Pan-STARRS	103	1.038	0.000	13.077150	−23.805910	58710.58	*i*	21.11
						58710.59	*z*	20.95
						58713.54	*z*	22.06
						58716.54	*z*	23.13
Pan-STARRS	104	1.366	1.738	12.057350	−25.794890	58710.58	*i*	21.01
						58710.59	*z*	20.53

Table B.2. continued.

Facility	Tile ID	$\int_{\rm tile} P_{\rm 2D}\,{\rm d}\Omega$ [%]	$\sum_{\rm tile} P_{\rm gal}$ [%]	RA [deg]	Dec [deg]	MJD	Filter	Limiting mag [AB]
						58713.54	z	22.09
						58716.54	z	23.11
Pan-STARRS	105	0.234	0.694	13.513300	−23.002300	58710.59	i	21.00
						58710.59	z	20.71
Pan-STARRS	106	0.001	0.000	13.944430	−22.197220	58710.57	z	20.09
Pan-STARRS	107	0.310	0.163	11.601450	−26.593980	58710.59	i	20.38
						58710.59	z	20.17
Pan-STARRS	108	2.143	0.940	12.509450	−24.592760	58710.59	i	21.22
						58710.59	z	20.95
						58713.54	z	22.24
						58716.54	z	23.20
Pan-STARRS	109	1.759	1.316	12.061140	−25.393260	58710.58	i	20.89
						58710.59	z	20.47
						58713.54	z	21.89
						58716.54	z	22.79
Pan-STARRS	110	0.584	0.000	13.076520	−23.404770	58710.59	i	21.07
						58710.59	z	20.84
						58713.54	z	21.38
						58716.54	z	22.48
Pan-STARRS	111	0.132	0.190	13.511430	−22.600940	58710.59	i	20.56
						58710.60	z	20.33
Pan-STARRS	112	0.006	0.000	11.139440	−27.391080	58710.60	z	19.86
Pan-STARRS	113	0.403	0.445	11.606820	−26.192410	58710.59	i	20.91
						58710.59	z	20.32
						58713.54	z	21.49
						58716.53	z	22.55
Pan-STARRS	114	2.086	0.000	12.511680	−24.191370	58710.59	i	21.27
						58710.59	z	20.93
						58713.54	z	22.17
						58716.54	z	23.17
Pan-STARRS	115	1.731	3.800	12.064900	−24.991680	58710.59	i	21.04
						58710.59	z	20.80
						58713.54	z	22.15
						58716.54	z	23.16
Pan-STARRS	116	1.479	1.546	12.637210	−23.805910	58710.59	i	21.15
						58710.59	z	20.92
						58713.54	z	22.14
						58716.54	z	23.18
Pan-STARRS	117	0.051	0.021	11.146440	−26.989770	58710.60	i	19.96
						58710.60	z	19.87
Pan-STARRS	118	0.237	0.778	13.075890	−23.003500	58710.59	i	20.93
						58710.59	z	20.67
Pan-STARRS	119	0.028	0.000	13.509580	−22.199530	58710.58	i	20.34
						58710.59	z	20.29
Pan-STARRS	120	0.723	0.978	11.612160	−25.790830	58710.59	i	21.01
						58710.59	z	20.55
						58713.54	z	21.96
						58716.54	z	23.06
Pan-STARRS	121	1.702	0.112	12.068640	−24.590190	58710.59	i	21.09
						58710.59	z	20.82
						58713.54	z	22.24
						58716.54	z	23.17
Pan-STARRS	122	0.091	0.090	11.153390	−26.588360	58710.60	i	20.10
						58710.60	z	19.89
Pan-STARRS	123	0.900	3.294	12.637840	−23.404770	58710.59	i	20.98
						58710.59	z	20.78
						58713.54	z	21.55
						58716.54	z	22.73
Pan-STARRS	124	0.152	0.387	13.075270	−22.602120	58710.59	i	20.65
						58710.59	z	20.37
Pan-STARRS	125	1.072	0.514	11.617460	−25.389260	58710.59	i	20.97
						58710.59	z	20.59
						58713.54	z	22.00
						58716.54	z	22.95
Pan-STARRS	126	0.001	0.000	13.507730	−21.798100	58710.58	z	20.13
Pan-STARRS	127	0.142	0.044	11.160300	−26.186890	58710.59	i	20.63
						58710.60	z	20.07
Pan-STARRS	128	1.472	0.000	12.072350	−24.188850	58710.59	i	21.13
						58710.59	z	20.81
						58713.54	z	22.19
						58716.54	z	23.16

Table B.2. continued.

Facility	Tile ID	$\int_{\rm tile} P_{\rm 2D}\,{\rm d}\Omega$ [%]	$\sum_{\rm tile} P_{\rm gal}$ [%]	RA [deg]	Dec [deg]	MJD	Filter	Limiting mag [AB]
Pan-STARRS	129	0.007	0.000	10.804940	−26.989770	58710.60	*i*	20.08
						58710.60	*z*	19.78
Pan-STARRS	130	0.391	0.585	12.638470	−23.003500	58710.59	*i*	20.92
						58710.59	*z*	20.60
Pan-STARRS	131	1.403	0.266	11.622730	−24.987750	58710.59	*i*	21.02
						58710.59	*z*	20.71
						58713.54	*z*	22.17
						58716.54	*z*	23.14
Pan-STARRS	132	1.305	4.121	12.197300	−23.804670	58710.58	*i*	21.12
						58710.59	*z*	20.76
						58713.54	*z*	22.15
						58716.54	*z*	23.16
Pan-STARRS	133	0.086	0.047	13.074650	−22.200690	58710.58	*i*	20.47
						58710.59	*z*	20.39
Pan-STARRS	134	0.231	0.506	11.167160	−25.785410	58710.59	*i*	20.82
						58710.59	*z*	20.45
						58713.54	*z*	21.42
						58716.53	*z*	22.48
Pan-STARRS	135	0.032	0.001	10.797980	−26.588360	58710.60	*i*	20.17
						58710.61	*z*	19.74
Pan-STARRS	136	1.291	1.461	11.627950	−24.586350	58710.59	*i*	20.96
						58710.59	*z*	20.74
						58713.54	*z*	22.21
						58716.54	*z*	23.13
Pan-STARRS	137	0.160	0.000	12.639090	−22.602120	58710.59	*i*	20.65
						58710.59	*z*	20.37
Pan-STARRS	138	1.066	3.200	12.199190	−23.403550	58710.58	*i*	21.00
						58710.59	*z*	20.59
						58713.54	*z*	21.11
						58716.53	*z*	22.22
Pan-STARRS	139	0.020	0.045	13.074040	−21.799230	58710.58	*i*	20.05
						58710.59	*z*	20.35
Pan-STARRS	140	0.448	0.347	11.173970	−25.383940	58710.59	*i*	20.89
						58710.59	*z*	20.54
						58713.54	*z*	21.86
						58716.54	*z*	22.95
Pan-STARRS	141	0.035	0.072	10.791080	−26.186890	58710.59	*i*	20.49
						58710.60	*z*	20.08
Pan-STARRS	142	1.210	1.096	11.633150	−24.185070	58710.59	*i*	20.97
						58710.59	*z*	20.74
						58713.54	*z*	22.16
						58716.54	*z*	23.08
Pan-STARRS	143	0.535	0.000	12.201060	−23.002300	58710.59	*i*	20.81
						58710.59	*z*	20.39
Pan-STARRS	144	0.061	0.064	12.639710	−22.200690	58710.58	*i*	20.67
						58710.59	*z*	20.31
Pan-STARRS	145	0.886	0.042	11.757470	−23.802170	58710.59	*i*	21.07
						58710.59	*z*	20.74
						58713.54	*z*	21.93
						58716.54	*z*	22.90
Pan-STARRS	146	0.634	0.855	11.180730	−24.982530	58710.59	*z*	20.59
						58710.59	*i*	20.84
						58713.54	*z*	21.98
						58716.54	*z*	23.00
Pan-STARRS	147	0.061	0.100	10.784220	−25.785400	58710.59	*i*	20.71
						58710.60	*z*	20.39
Pan-STARRS	148	0.246	0.017	12.202930	−22.600940	58710.58	*i*	20.65
						58710.59	*z*	20.27
Pan-STARRS	149	0.042	0.078	12.640320	−21.799230	58710.58	*i*	20.52
						58710.59	*z*	20.28
Pan-STARRS	150	0.003	0.000	10.349920	−26.593980	58710.60	*i*	20.13
						58710.61	*z*	19.58
Pan-STARRS	151	0.711	0.000	11.760610	−23.401100	58710.58	*i*	20.88
						58710.59	*z*	20.46
Pan-STARRS	152	0.693	0.272	11.187450	−24.581220	58710.59	*z*	20.67
						58710.59	*i*	20.80
						58713.54	*z*	21.98
						58716.54	*z*	22.92
Pan-STARRS	153	0.175	0.271	10.777410	−25.383940	58710.59	*i*	20.76
						58710.60	*z*	20.45
Pan-STARRS	154	0.014	0.000	10.344550	−26.192410	58710.60	*i*	20.12
						58710.61	*z*	19.52

Table B.2. continued.

Facility	Tile ID	$\int_{\rm tile} P_{\rm 2D}\,{\rm d}\Omega$ [%]	$\sum_{\rm tile} P_{\rm gal}$ [%]	RA [deg]	Dec [deg]	MJD	Filter	Limiting mag [AB]
Pan-STARRS	155	0.096	0.074	12.204780	−22.199530	58710.58	*i*	20.62
						58710.59	*z*	20.24
Pan-STARRS	156	0.839	0.484	11.194130	−24.180040	58710.59	*i*	20.76
						58710.59	*z*	20.61
						58713.54	*z*	21.60
						58716.54	*z*	22.46
Pan-STARRS	157	0.571	0.969	11.763740	−22.999890	58710.58	*i*	20.64
						58710.59	*z*	20.39
Pan-STARRS	158	0.022	0.223	12.640930	−21.397800	58710.58	*z*	20.14
Pan-STARRS	159	0.658	1.166	11.317760	−23.798430	58710.59	*i*	20.92
						58710.59	*z*	20.60
						58713.53	*z*	21.15
						58716.54	*z*	21.75
Pan-STARRS	160	0.300	0.146	10.770640	−24.982530	58710.60	*i*	20.79
						58710.60	*z*	20.48
						58713.54	*z*	20.26
						58716.52	*z*	21.51
Pan-STARRS	161	0.023	0.000	10.339210	−25.790820	58710.59	*i*	20.43
						58710.60	*z*	20.11
Pan-STARRS	162	0.025	0.000	12.206630	−21.798100	58710.58	*i*	20.56
						58710.59	*z*	20.13
Pan-STARRS	163	0.266	0.000	11.766840	−22.598590	58710.58	*i*	20.62
						58710.60	*z*	20.29
Pan-STARRS	164	0.365	0.177	11.322160	−23.397430	58710.59	*i*	20.83
						58710.59	*z*	20.38
Pan-STARRS	165	0.298	0.611	10.763920	−24.581210	58710.59	*i*	20.75
						58710.60	*z*	20.52
Pan-STARRS	166	0.035	0.053	10.333910	−25.389260	58710.59	*i*	20.65
						58710.60	*z*	20.37
Pan-STARRS	167	0.096	0.062	11.769930	−22.197220	58710.58	*i*	20.67
						58710.59	*z*	20.16
Pan-STARRS	168	0.019	0.000	12.208460	−21.396690	58710.56	*i*	20.27
Pan-STARRS	169	0.422	0.625	11.326540	−22.996290	58710.58	*i*	20.69
						58710.60	*z*	20.26
Pan-STARRS	170	0.357	0.303	10.757250	−24.180040	58710.59	*i*	20.74
						58710.60	*z*	20.53
Pan-STARRS	171	0.001	0.000	9.897830	−26.196550	58710.62	*z*	19.31
Pan-STARRS	172	0.456	0.493	10.878240	−23.793450	58710.58	*i*	20.67
						58710.59	*z*	20.49
Pan-STARRS	173	0.084	0.014	10.328650	−24.987750	58710.59	*i*	20.78
						58710.60	*z*	20.46
Pan-STARRS	174	0.052	0.073	11.773010	−21.795840	58710.57	*i*	20.43
						58710.58	*z*	20.04
Pan-STARRS	175	0.282	0.000	11.330880	−22.595060	58710.58	*i*	20.41
						58710.59	*z*	20.23
Pan-STARRS	176	0.007	0.000	9.894020	−25.794890	58710.60	*i*	20.24
						58710.62	*z*	19.53
Pan-STARRS	177	0.239	0.071	10.883890	−23.392540	58710.58	*i*	20.67
						58710.58	*z*	20.36
Pan-STARRS	178	0.148	0.211	10.323420	−24.586340	58710.59	*i*	20.70
						58710.60	*z*	20.51
Pan-STARRS	179	0.022	0.000	11.776060	−21.394470	58710.56	*i*	20.24
Pan-STARRS	180	0.096	0.365	11.335210	−22.193760	58710.58	*i*	20.51
						58710.59	*z*	20.03
Pan-STARRS	181	0.009	0.000	9.890230	−25.393250	58710.60	*i*	20.33
						58710.61	*z*	20.01
Pan-STARRS	182	0.269	0.133	10.550410	−23.793450	58710.58	*i*	20.54
						58710.59	*z*	20.48
Pan-STARRS	183	0.185	0.071	10.889510	−22.991490	58710.59	*i*	20.44
						58710.60	*z*	19.97
Pan-STARRS	184	0.203	0.295	10.318230	−24.185070	58710.59	*i*	20.60
						58710.59	*z*	20.45
Pan-STARRS	185	0.053	0.076	11.339510	−21.792450	58710.58	*i*	20.45
Pan-STARRS	186	0.008	0.000	9.886470	−24.991670	58710.59	*i*	20.34
						58710.60	*z*	20.04
Pan-STARRS	187	0.171	0.313	10.544750	−23.392540	58710.58	*i*	20.58
						58710.58	*z*	20.32
Pan-STARRS	188	0.135	0.028	10.895100	−22.590350	58710.58	*z*	19.91
						58710.58	*i*	20.49

Table B.2. continued.

Facility	Tile ID	$\int_{\text{tile}} P_{\text{2D}}\,\mathrm{d}\Omega$ [%]	$\sum_{\text{tile}} P_{\text{gal}}$ [%]	RA [deg]	Dec [deg]	MJD	Filter	Limiting mag [AB]
Pan-STARRS	189	0.000	0.000	9.448690	−25.797610	58710.61	*z*	19.02
Pan-STARRS	190	0.018	0.215	9.882730	−24.590190	58710.59	*i*	20.45
						58710.60	*z*	20.24
Pan-STARRS	191	0.078	0.229	10.539130	−22.991490	58710.58	*z*	19.86
						58710.58	*i*	20.40
Pan-STARRS	192	0.063	0.380	10.900660	−22.189150	58710.58	*i*	20.28
Pan-STARRS	193	0.105	0.230	10.110880	−23.798430	58710.58	*i*	20.23
						58710.59	*z*	20.27
Pan-STARRS	194	0.000	0.000	9.446420	−25.395920	58710.59	*i*	20.08
						58710.60	*z*	20.02
Pan-STARRS	195	0.051	0.035	9.879020	−24.188850	58710.59	*i*	20.38
						58710.60	*z*	20.18
Pan-STARRS	196	0.085	0.156	10.533540	−22.590350	58710.58	*i*	20.48
Pan-STARRS	197	0.032	0.017	10.906190	−21.787920	58710.59	*i*	19.96
Pan-STARRS	198	0.055	0.171	10.106490	−23.397430	58710.58	*i*	20.31
						58710.59	*z*	20.21
Pan-STARRS	199	0.000	0.000	9.444160	−24.994290	58710.59	*i*	20.01
						58710.60	*z*	19.95
Pan-STARRS	200	0.040	0.000	10.527980	−22.189150	58710.58	*i*	20.28
Pan-STARRS	201	0.040	0.000	10.102110	−22.996290	58710.58	*i*	20.20
Pan-STARRS	202	0.003	0.000	9.441920	−24.592760	58710.59	*i*	20.23
						58710.60	*z*	20.04
Pan-STARRS	203	0.021	0.015	9.671180	−23.802170	58710.59	*i*	20.16
						58710.60	*z*	20.09
Pan-STARRS	204	0.012	0.000	9.439690	−24.191370	58710.58	*i*	19.97
						58710.60	*z*	20.18
Pan-STARRS	205	0.030	0.000	10.097760	−22.595060	58710.58	*i*	20.29
Pan-STARRS	206	0.007	0.000	9.668040	−23.401100	58710.60	*z*	20.11
Pan-STARRS	207	0.035	0.148	10.093440	−22.193760	58710.58	*i*	20.23
Pan-STARRS	208	0.000	0.000	9.001020	−24.594050	58710.60	*z*	19.98
Pan-STARRS	209	0.011	0.000	9.231350	−23.804660	58710.60	*z*	19.98
Pan-STARRS	210	0.008	0.000	9.000280	−24.192630	58710.60	*z*	20.00
ATLAS	0	0.255	0.000	28.894690	−35.720480	58710.60	*o*	17.99
						58710.61	*o*	18.05
						58710.61	*o*	18.06
						58710.61	*o*	18.18
						58710.62	*o*	18.06
						58710.63	*o*	17.87
						58710.64	*o*	17.15
						58711.49	*o*	17.73
						58711.49	*o*	17.62
						58711.50	*o*	17.82
						58711.51	*o*	17.61
						58715.63	*o*	17.77
						58715.63	*o*	17.57
						58715.64	*o*	16.81
						58717.51	*o*	19.08
						58717.52	*o*	19.09
						58717.52	*o*	19.12
						58717.53	*o*	19.12
						58717.58	*o*	19.23
						58717.59	*o*	19.29
						58717.59	*o*	19.24
						58717.60	*o*	19.20
						58719.55	*o*	18.99
						58719.56	*o*	18.98
						58719.56	*o*	19.08
						58719.57	*o*	19.11
						58719.58	*o*	18.94
						58719.59	*o*	19.04
						58719.60	*o*	19.18
						58719.61	*o*	19.11
						58721.50	*c*	18.38
						58721.51	*c*	17.72
						58721.52	*c*	16.97
						58721.52	*c*	17.35
						58721.52	*c*	16.43
						58721.52	*c*	18.28
						58721.53	*c*	18.59
						58721.54	*c*	18.10
						58723.51	*o*	19.68

Table B.2. continued.

Facility	Tile ID	$\int_{\text{tile}} P_{\text{2D}}\, d\Omega$ [%]	$\sum_{\text{tile}} P_{\text{gal}}$ [%]	RA [deg]	Dec [deg]	MJD	Filter	Limiting mag [AB]
						58723.51	*o*	19.61
						58723.52	*o*	19.65
						58723.53	*o*	19.70
						58729.51	*c*	19.58
						58729.52	*c*	19.62
						58729.52	*c*	19.61
						58729.54	*c*	19.61
ATLAS	1	1.539	0.803	27.030780	−30.463550	58710.60	*o*	17.97
						58710.61	*o*	18.11
						58710.61	*o*	18.16
						58710.61	*o*	18.29
						58710.62	*o*	18.18
						58710.63	*o*	18.05
						58710.64	*o*	17.45
						58711.49	*o*	17.80
						58711.49	*o*	17.90
						58711.49	*o*	17.73
						58711.51	*o*	17.75
						58723.52	*o*	19.69
						58723.53	*o*	19.74
						58723.53	*o*	19.76
						58723.54	*o*	19.70
						58729.53	*c*	19.67
						58729.53	*c*	19.64
						58729.54	*c*	19.65
						58729.55	*c*	19.54
ATLAS	2	3.346	2.593	22.579410	−35.715450	58710.61	*o*	17.97
						58710.61	*o*	17.97
						58710.61	*o*	17.95
						58710.61	*o*	18.05
						58710.62	*o*	18.06
						58710.63	*o*	17.95
						58710.63	*o*	17.61
						58710.64	*o*	16.87
						58711.47	*o*	17.10
						58711.48	*o*	17.43
						58711.48	*o*	17.66
						58711.50	*o*	17.77
						58715.62	*o*	18.40
						58715.62	*o*	18.36
						58715.63	*o*	18.38
						58715.63	*o*	18.09
						58715.64	*o*	16.39
						58715.64	*o*	16.39
						58717.56	*o*	19.24
						58717.56	*o*	19.29
						58717.57	*o*	19.26
						58717.58	*o*	19.15
						58719.57	*o*	19.21
						58719.57	*o*	19.17
						58719.58	*o*	19.14
						58719.60	*o*	19.11
						58721.47	*c*	17.44
						58721.47	*c*	16.64
						58721.48	*c*	16.79
						58721.49	*c*	17.36
						58723.51	*o*	19.75
						58723.51	*o*	19.71
						58723.52	*o*	19.67
						58723.53	*o*	19.76
						58729.52	*c*	19.62
						58729.52	*c*	19.57
						58729.53	*c*	19.64
						58729.54	*c*	19.60
ATLAS	3	5.950	8.104	21.127280	−30.465150	58710.60	*o*	17.98
						58710.60	*o*	17.98
						58710.61	*o*	18.06
						58710.61	*o*	18.16
						58710.62	*o*	18.12
						58710.63	*o*	18.02
						58710.63	*o*	17.50

Table B.2. continued.

Facility	Tile ID	$\int_{\text{tile}} P_{\text{2D}}\, d\Omega$ [%]	$\sum_{\text{tile}} P_{\text{gal}}$ [%]	RA [deg]	Dec [deg]	MJD	Filter	Limiting mag [AB]
						58711.48	*o*	17.86
						58711.49	*o*	17.86
						58711.49	*o*	17.94
						58711.50	*o*	17.68
						58715.63	*o*	17.91
						58715.63	*o*	17.74
						58715.64	*o*	16.76
						58717.56	*o*	19.25
						58717.57	*o*	19.28
						58717.57	*o*	19.30
						58717.58	*o*	19.28
						58719.57	*o*	19.16
						58719.57	*o*	19.19
						58719.58	*o*	19.13
						58719.60	*o*	19.15
						58721.54	*c*	19.41
						58721.54	*c*	19.39
						58721.54	*c*	19.48
						58721.56	*c*	17.92
						58723.51	*o*	19.72
						58723.52	*o*	19.75
						58723.53	*o*	19.78
						58723.54	*o*	19.76
						58729.41	*c*	19.44
						58729.41	*c*	19.45
						58729.42	*c*	19.48
						58729.43	*c*	19.49
ATLAS	4	0.779	0.940	16.612370	−21.115100	58717.56	*o*	19.32
						58717.57	*o*	19.29
						58717.57	*o*	19.37
						58717.58	*o*	19.31
						58721.56	*c*	18.48
						58721.56	*c*	19.35
						58721.58	*c*	19.52
						58721.59	*c*	18.83
ATLAS	5	74.316	70.325	14.688290	−25.215570	58710.60	*o*	18.03
						58710.61	*o*	18.07
						58710.61	*o*	18.07
						58710.61	*o*	17.95
						58710.61	*o*	18.07
						58710.61	*o*	18.09
						58710.62	*o*	18.16
						58710.62	*o*	18.04
						58710.63	*o*	18.06
						58710.63	*o*	17.94
						58710.63	*o*	17.65
						58710.63	*o*	17.50
						58710.64	*o*	16.86
						58710.64	*o*	16.60
						58711.47	*o*	17.43
						58711.48	*o*	17.57
						58711.48	*o*	17.92
						58711.49	*o*	17.99
						58711.49	*o*	17.91
						58711.49	*o*	17.80
						58711.50	*o*	17.77
						58711.51	*o*	17.87
						58715.62	*o*	18.37
						58715.62	*o*	18.40
						58715.63	*o*	18.24
						58715.63	*o*	17.79
						58717.54	*o*	19.31
						58717.55	*o*	19.40
						58717.55	*o*	19.36
						58717.56	*o*	19.29
						58719.57	*o*	19.29
						58719.57	*o*	19.08
						58719.58	*o*	19.22
						58719.60	*o*	19.19
						58721.54	*c*	19.40
						58721.54	*c*	19.48

Table B.2. continued.

Facility	Tile ID	$\int_{\text{tile}} P_{\text{2D}}\, d\Omega$ [%]	$\sum_{\text{tile}} P_{\text{gal}}$ [%]	RA [deg]	Dec [deg]	MJD	Filter	Limiting mag [AB]
						58721.56	*c*	18.36
						58721.56	*c*	19.34
						58723.51	*o*	19.71
						58723.52	*o*	19.78
						58723.53	*o*	19.83
						58723.53	*o*	19.80
						58729.52	*c*	19.67
						58729.53	*c*	19.67
						58729.53	*c*	19.63
						58729.55	*c*	19.50
ATLAS	6	1.383	1.044	14.211200	−19.966080	58710.61	*o*	18.14
						58710.62	*o*	18.21
						58710.62	*o*	18.19
						58710.63	*o*	18.08
						58710.63	*o*	17.57
						58710.64	*o*	16.76
						58710.64	*o*	16.76
						58711.49	*o*	17.96
						58711.49	*o*	17.91
						58711.50	*o*	17.91
						58711.51	*o*	17.97
						58717.54	*o*	19.34
						58717.55	*o*	19.35
						58717.55	*o*	19.41
						58717.56	*o*	19.29
						58719.57	*o*	19.25
						58719.58	*o*	19.31
						58719.60	*o*	19.22
						58719.60	*o*	19.22
						58721.54	*c*	19.52
						58721.55	*c*	18.66
						58721.56	*c*	18.73
						58721.56	*c*	19.30
						58723.53	*o*	19.81
						58723.53	*o*	19.87
						58723.54	*o*	19.76
						58723.54	*o*	19.87
						58723.55	*o*	19.80
						58723.55	*o*	19.80
						58723.56	*o*	19.66
						58723.56	*o*	19.72
						58729.53	*c*	19.61
						58729.53	*c*	19.67
						58729.55	*c*	19.53
						58729.55	*c*	19.61
						58729.55	*c*	19.61
						58729.56	*c*	19.63
						58729.56	*c*	19.54
						58729.56	*c*	19.62
ATLAS	7	20.026	16.401	8.971660	−25.216580	58710.60	*o*	17.91
						58710.61	*o*	17.95
						58710.61	*o*	18.01
						58710.62	*o*	18.03
						58710.62	*o*	17.95
						58710.63	*o*	17.66
						58710.64	*o*	16.95
						58715.62	*o*	18.48
						58715.62	*o*	18.35
						58715.63	*o*	18.30
						58715.63	*o*	18.19
						58719.54	*o*	19.17
						58719.54	*o*	19.18
						58719.55	*o*	19.18
						58719.56	*o*	19.13
						58729.49	*c*	19.63
						58729.49	*c*	19.63
						58729.50	*c*	19.59
						58729.51	*c*	19.61
ATLAS	8	0.893	1.101	8.675490	−19.966510	58710.60	*o*	18.02
						58710.61	*o*	18.00
						58710.61	*o*	17.97

Table B.2. continued.

Facility	Tile ID	$\int_{\text{tile}} P_{\text{2D}}\, d\Omega$ [%]	$\sum_{\text{tile}} P_{\text{gal}}$ [%]	RA [deg]	Dec [deg]	MJD	Filter	Limiting mag [AB]
						58710.61	*o*	18.17
						58710.62	*o*	18.09
						58710.63	*o*	17.84
						58710.64	*o*	17.14
						58719.53	*o*	19.15
						58719.53	*o*	19.23
						58719.54	*o*	19.08
						58719.55	*o*	19.14
						58723.52	*o*	19.80
						58723.53	*o*	19.83
						58723.53	*o*	19.83
						58723.54	*o*	19.83
						58723.55	*o*	19.74
						58729.49	*c*	19.67
						58729.49	*c*	19.63
						58729.49	*c*	19.64
						58729.49	*c*	19.67
						58729.50	*c*	19.65
						58729.50	*c*	19.64
						58729.51	*c*	19.67
						58729.51	*c*	19.65
GOTO	T0688	0.469	0.706	11.489360	−30.000000	58710.20	*L*	18.20
						58711.15	*L*	18.20
GOTO	T0689	0.983	0.535	15.319150	−30.000000	58711.16	*L*	18.10
GOTO	T0691	3.954	3.162	22.978720	−30.000000	58710.18	*L*	18.50
						58710.23	*L*	18.80
						58711.18	*L*	18.30
GOTO	T0692	0.241	0.064	26.808510	−30.000000	58711.19	*L*	18.40
GOTO	T0782	54.585	54.460	11.020410	−25.714290	58710.13	*L*	19.00
						58710.13	*L*	18.50
						58710.15	*L*	19.10
						58710.17	*L*	18.40
						58711.12	*L*	17.90
GOTO	T0783	44.873	39.755	14.693880	−25.714290	58710.16	*L*	19.10
						58710.16	*L*	19.10
						58710.17	*L*	18.70
						58710.18	*L*	18.40
						58710.19	*L*	19.10
						58710.22	*L*	19.10
						58711.14	*L*	18.30
GOTO	T0880	10.427	16.027	10.693070	−21.428570	58710.09	*L*	18.50
						58710.20	*L*	18.50
						58710.21	*L*	18.80
						58711.09	*L*	18.30
GOTO	T0881	7.210	9.963	14.257430	−21.428570	58710.10	*L*	18.50
						58710.10	*L*	18.20
						58710.21	*L*	18.80
						58711.10	*L*	17.90

Appendix C: Candidate counterparts

The list of publicly reported candidate counterparts for S190814bv is given in Table C.1. All photometry of the candidates discovered by our search is available at the CDS. Some detailed comments on specific candidates follow:

- AT2019nor: Pan-STARRS lightcurve lasts for at least 70 days from discovery, with a slow decline of 1.2 mag per 100 days in w consistent with a Type IIP SN on the plateau.
- AT2019npd: Likely associated with the foreground galaxy NGC 253.
- AT2019npe: No detection in Pan-STARRS images taken on 58710.58 (7 h after the GROWTH detection) to a limiting magnitude of $w = 21.2$.
- AT2019npj: Ruled out by Pan-STARRS detection on 2019-08-04, ten days before GW event.
- AT2019npz: Consistent with the nucleus of a compact galaxy, could be AGN or other nuclear transient. Flat lightcurve around $w = 21.5$ in Pan-STARRS images taken between 20 and 70 days after the GW.
- AT2019nqe: Reported to the TNS with $i = 21.2$ on 08/16, there are no historic detections in Pan-STARRS, ATLAS or reported by ZTF.
- AT2019nqp: Archival Pan-STARRS detections from 2018.
- AT2019nqw: Still present in GRAWITA images two weeks after GW event.
- AT2019nra: A J-band spectrum taken 3 days after discovery was reported in GCN 25395 to be featureless.
- AT2019nsm: Seen in PS1 images prior to GW event.
- AT2019nte: The transient fades by 1 mag in i-band over two consecutive nights (from 20.95 on 08/16 to 21.92 on 08/17. However, the transient is still visible at $i = 22.3$ (GCN 25598) ten days later on 08/27.The source is consistent with the nucleus of it's host galaxy.
- AT2019ntm: An 1800s spectrum of the host was taken on 2019-09-09 with the *William Herschel* Telescope

(WHT)+ACAM using the V400 grism. The spectrum reveals a single emission feature, that if associated with Hα corresponds to a redshift of 0.116.
- AT2019ntp: Spectrum in GCN 25596 is reported to be that of a broad-lined Type Ic SN, no redshift is listed in GCN.
- AT2019nts: $z = 20.9$ on 8/17, and $i = 20.3$ on 8/18 (DECAM photometry via TNS) implies that the transient is either rising or has a blue $i-z$ colour 4 days after the GW event.
- AT2019nuj: A detection at $w = 22$ on MJD 58699 was recovered in Pan-STARRS data. The lightcurve is consistent with a SN.
- AT2019nuk: Transient is not offset from its host galaxy. Spectroscopic redshift is consistent with GW, while DECAM photometry on TNS appears to show a rapid decline (2.6 mag over one day). However, if associated with S190814bv, then the absolute magnitude three days after the GW event would be $i = -18.1$.
- AT2019nul: An 1800s spectrum of the host was taken on 2019-09-12 with the *William Herschel* Telescope (WHT)+ACAM using the V400 grism.
- AT2019nun: An 1800s spectrum of the host was taken on 2019-09-11 with the *William Herschel* Telescope (WHT)+ACAM using the V400 grism.
- AT2019nuw: Likely SN, flat lightcurve in Pan-STARRS.
- AT2019nux: Likely SN, flat lightcurve in Pan-STARRS.
- AT2019nuy: Offset from faint host in Pan-STARRS.
- AT2019nuz: Likely SN, flat lightcurve in Pan-STARRS.
- AT2019nva: Likely SN, flat lightcurve in Pan-STARRS.
- AT2019nvb: Likely associated with the foreground galaxy NGC 253.
- AT2019nvd: Likely SN, flat lightcurve in Pan-STARRS.
- AT2019nve: Likely SN, flat lightcurve in Pan-STARRS.
- AT2019nvr: Likely SN, flat lightcurve in Pan-STARRS.
- AT2019nvs: Likely SN, flat lightcurve in Pan-STARRS.
- AT2019nys: The DES photometric redshift catalogue reports $z = 0.41 \pm 0.06$ for the host.
- AT2019nzd: Brightens by 0.4 mag between two DECAM i-band images taken 0.7 h apart on 08/21.
- AT2019nzr: An 1800s spectrum of the host was taken on 2019-09-09 with the *William Herschel* Telescope (WHT)+ACAM using the V400 grism. The spectrum revealed a featureless continuum with no clear emission features, and we were unable to secure a redshift. While the DES colours for the host are consistent with an AGN (GCN 25486), the spectrum does not show Seyfert features.
- AT2019oab: While the reported photometric redshift appears grossly inconsistent with the distance to the GW event, we note that the reported lightcurve fades by 0.8 mag over two days.
- AT2019oac: Rises by 0.2 mag in z between 08/18 and 08/21
- AT2019odc: The host redshift is consistent with S190814bv. GTC spectroscopy (reported in GCN 25588) with the slit covering the position of the transient reveals no broad features in the spectrum.
- AT2019oer: Detection in VISTA archive imaging (Arnaboldi et al. 2010), published in ENGRAVE GCN 25447.
- AT2019okr. Detection in VISTA archival imaging (Arnaboldi et al. 2010), published in ENGRAVE GCN 25526
- AT2019oks: No change in i-band magnitude over 4 days, suggests unrelated to GW event. An 1800s spectrum of the host was taken on 2019-09-09 with the *William Herschel* Telescope (WHT)+ACAM using the V400 grism. The spectrum reveals a single emission feature, that if associated with Hα corresponds to a redshift of 0.193.
- AT2019omu: i-band photometry reported by DES reveals a decline of only 0.3 mag over the five days after discovery. Moreover, the photometric redshift of the host from the DES photometric redshift catalogue is reported to be 0.66 ± 0.03
- AT2019omw: Flat lightcurve in i-band between 08/18 and 08/21 from DECAM photometry reported on TNS.
- AT2019onj. Detection in VISTA archival imaging (Arnaboldi et al. 2010), published in ENGRAVE GCN 25526
- AT2019opp: Lightcurve from DECAM reported on TNS shows a rise in magnitude one week after the GW event.
- AT2019osy. Radio transient found by the Australian Square Kilometre Array Pathfinder (ASKAP). Followup with HST and ALMA confirms peculiar transient unrelated to GW event.
- AT2019qbu: Non-detection to $r = 22.3$ on 8/16 (after GW event).
- AT2019qby: 0.5 mag decline in r-band over 6 days.
- AT2019qbz: Fades by 0.2 mag over 6 days. Apparently hostless.
- AT2019qca: Apparently hostless source that has a constant magnitude from discovery until at least 08/30.
- AT2019qcb: Fades by only 0.2 mag over two weeks from discovery.
- AT2019qcc: 0.2 mag decline over 10 days after discovery.
- AT2019aacd: Reported by Vieira et al. (2020) (with the identifier CFHT0054-2345zau) as a potential counterpart after the first submission of this manuscript, and subsequently added to Table C.1 upon revision. On 08/21 we observed a similar footprint with the Pan-STARRS2 telescope in the $i_{\rm P1}$ filter. We did not carry out an independent transient search in these data, since the facility was still in science commissioning mode, but we stored the data to provide additional photometry for any interesting source. We cross-checked these data to confirm the proposed i-band transient found by the CFHT search: we have a nearby 5σ detection on MJD 58716.573 (5 days after the CFHT discovery), but it is $0\farcs6$ from CFHT0054-2345zau, closer to the galaxy's core ($0\farcs48$ separation) and, if real, its measured $i_{\rm P1}$ magnitude is 22.2 ± 0.2. However, this is clearly offset from the CFHT object, and no excess flux is visible at the position of the CFHT object to $i_{\rm P1} < 22.3$. Vieira et al. find $i = 21.5$ just 1 day later, which is therefore incompatible with our PS2 images. There is no detection in the $z_{\rm P1}$ data of PS1 either, hence we consider both the CFHT object and the excess flux in the PS2 $i_{\rm P1}$-band to be bogus artefacts from image subtraction.

Table C.1. Candidate counterparts reported to the GW 190814bv.

IAU name	Survey name	Coordinates	Discovery date	Mag	Source	z	GCNs	Comments
AT2019nbp	PS19ekf	00:46:57.393 −24:21:42.70	8/09 13:58:04	$w = 20.0$	PS1	?		Pre.Det.
AT2019nmd	desgw-190814a	00:51:29.004 −22:28:16.96	8/15 06:40:19	$i = 20.6$	DESGW	–	25336,25348	Ast
AT2019nme	desgw-190814b	00:50:32.558 −22:13:33.70	8/15 06:40:19	$i = 19.3$	DESGW	–	25336,25355	Ast
AT2019noq	PS19epf, VSTJ004847.88-251823.5	00:48:47.882 −25:18:23.46	8/15 14:02:24	$i = 19.9$	PS1	0.07 25669	25356,25423,	SN
AT2019nor	PS19eph	00:49:51.992 −24:16:17.71	8/15 14:02:24	$i = 19.7$	PS1	?	25356	SN?*
AT2019npd	DG19hqpgc, PS19epw, VSTJ004656.70-252236	00:46:56.711 −25:22:36.43	8/15 06:43:12	$i = 19.1$	GROWTH	0.0008	25362,25669	Spec.Host-z*
AT2019npe	DG19prsgc, VSTJ004133.33-234432.0	00:41:33.330 −23:44:31.94	8/15 06:37:26	$z = 20.1$	GROWTH	–	25362	Non.Det.*
AT2019npj	DG19frdgc,PS19epv	00:46:11.590 −22:07:07.82	8/15 07:20:38	$z = 19.7$	GROWTH	?	25362	Pre.Det.*
AT2019npv	DG19wxnjc, PS19eqi, VSTJ005332.32-234958.5	00:53:32.309 −23:49:58.64	8/16 07:45:07	$i = 20.7$	GROWTH	0.056	25393,25454	SN
AT2019npw	DG19wgmjc, PS19eqj, VSTJ005552.40-254659.8	00:55:52.405 −25:46:59.80	8/16 07:39:21	$i = 20.6$	GROWTH	0.163	25362,25484	SN
AT2019npy	DG19sevhc,PS19epy	00:56:12.020 −25:29:24.28	8/16 05:48:28	$i = 20.4$	GROWTH	–	25362,25383, 25374,25386	HPM
AT2019npz	DG19tzyhc, VSTJ005305.56-242138.7	00:53:05.560 −24:21:38.71	8/16 05:57:07	$z = 20.6$	GROWTH	?	25362	AGN?*
AT2019nqc	DG19qabkc	01:29:03.673 −32:42:18.50	8/16 08:23:59	$i = 20.6$	GROWTH	0.078	25362,25571	SN
AT2019nqe	DG19etlkc	01:25:49.625 −34:07:10.49	8/16 08:52:48	$i = 21.2$	GROWTH	?	25398	?*
AT2019nqp	PS19epx	00:56:50.403 −24:20:49.95	8/15 14:05:16	$z = 20.7$	PS1	?	–	Pre.Det.*
AT2019nqq	desgw-190814c	01:23:49.217 −33:02:05.00	8/15 07:09:07	$i = 20.8$	DESGW	0.071	25373,25419	SN
AT2019nqr	desgw-190814d	01:34:17.649 −32:44:30.41	8/16 06:31:40	$i = 18.3$	DESGW	0.084	25373,25379	SN
AT2019nqs	desgw-190814e	01:33:35.164 −31:46:48.48	8/16 07:07:40	$i = 20.4$	DESGW	0.1263	25373,25384	Spec.Host-z
AT2019nqw	DG19xczjc, PS19eqk, VSTJ005646.69-250933.3	00:56:46.717 −25:09:33.42	8/16 08:18:14	$z = 20.0$	GROWTH	?	25748	SN?*

Notes. We only list candidates that were first reported to the TNS after 7 Aug (one week prior to the GW event), and that were discovered up to two weeks after the GW event. The "Comments" column lists the reason why candidates were discounted: Non.Det. = no subsequent detection after first report; Ast = asteroid, moving object; Spec.Host-z = spectroscopic redshift of host is inconsistent with GW; Phot.Host-z = photometric redshift of host is inconsistent with GW (we note that photometric redshifts are reported to one decimal place in the redshift column); SN = spectroscopically classified as a supernova; SN? = probable supernova; Pre.Det. = historical detection in survey data prior to S190814bv; HPM = high proper motion star; AGN/AGN? = active galactic nucleus flare or other nuclear transient (or probable nuclear transient); Andreoni = candidates which are reported and ruled out in Andreoni et al. (2020). Candidates which we are unable to classify are indicated with "?". Objects with an asterisk in the comment column are discussed in more detail in the text of Appendix C. [(a)]Not reported in GCN, candidate announced on TNS and in Andreoni et al. (2020). [(b)]References for GCNs listed in the table: Soares-Santos et al. (2019a), De et al. (2019b), Goldstein et al. (2019a), Huber et al. (2019), Andreoni et al. (2019a), Chen et al. (2019), Herner et al. (2019a), Dichiari et al. (2019), Tucker et al. (2019b), Rossi et al. (2019), Brunn et al. (2019), Smartt et al. (2019b), Goldstein et al. (2019b,c), Goldstein & Anand (2019), Dimitriadis et al. (2019), Herner et al. (2019b), Srivastas et al. (2019), Lopez-Cruz et al. (2019a), Rodriguez et al. (2019), Soares-Santos et al. (2019b,c), Ruan et al. (2019), Japelj et al. (2019a), Jonker et al. (2019), Smartt et al. (2019a), Tucker et al. (2019a), Soares-Santos et al. (2019d), Stewart et al. (2019), Andreoni et al. (2019b), Japelj et al. (2019b), Wiesner et al. (2019b), Castro-Tirado et al. (2019), Lopez-Cruz et al. (2019b), Hu et al. (2019), Wiesner et al. (2019a), Grado et al. (2019b), Yang et al. (2019), Cartier et al. (2019), Bauer et al. (2019)

Table C.1. continued.

IAU name	Survey name	Coordinates	Discovery date	Mag	Source	z	GCNs	Comments
AT2019nqz	DG19ayfjc	00:46:46.416 −24:20:12.06	8/16 07:22:04	$z = 21.1$	GROWTH	0.1076	25391,25571	Spec.Host-z
AT2019nra	DG19njmjc	00:55:10.705 −25:56:57.12	8/16 06:01:26	$i = 20.5$	GROWTH	?	25395	?*
AT2019nsm	DG19wlpmc, VSTJ004330.16-224329.4	00:43:30.111 −22:43:29.46	8/17 07:20:38	$z = 20.4$	GROWTH	?	25393	Pre.Det.*
AT2019nte	desgw-190814f	01:34:13.766 −31:43:18.12	8/16 07:07:40	$i = 21.0$	DESGW	0.0704	25398,25784	AGN?*
AT2019ntm	DG19jqzkc, VSTJ004804.40-234750.9	00:48:04.438 −23:47:50.91	8/17 04:58:04	$i = 19.7$	GROWTH	0.116?	25486	Spec.Host-z?
AT2019ntn	DG19rtekc, desgw-190814i	01:34:53.352 −31:22:49.74	8/16 07:07:40	$i = 21.6$	GROWTH	0.10	25393,25423	SN
AT2019ntp	DG19gcwjc, PS19eqq, VSTJ005012.07-261152.6	00:50:12.060 −26:11:52.81	8/16 07:35:02	$z = 21.1$	GROWTH	?	25393,25596	SN*
AT2019ntr	DG19sbzkc VSTJ010001.84-264251.3	01:00:01.879 −26:42:51.65	8/16 07:53:45	$z = 20.6$	GROWTH	0.2	25393,25540	SN
AT2019nts	DG19vodmc	00:48:31.378 −23:06:39.24	8/17 06:50:23	$z = 20.9$	GROWTH	?	25393	SN?*
AT2019nuj	DG19hqhjc, VSTJ004901.74-231404.9	00:49:01.738 −23:14:04.93	8/16 07:29:16	$z = 20.8$	GROWTH	?	25393	Pre.Det*
AT2019nuk	DG19dnjlc	00:54:57.827 −26:08:04.61	8/17 05:22:33	$i = 21.6$	GROWTH	0.076	25393,25394	?*
AT2019nul	DG19kpykc	00:55:16.443 −26:56:34.57	8/16 07:53:45	$z = 20.3$	GROWTH	0.098	25393	Spec.Host-z*
AT2019num	DG19rzhoc, VSTJ005531.60-225808.5	00:55:31.602 −22:58:08.48	8/18 06:41:45	$i = 21.1$	GROWTH	0.113	25393,25484	SN
AT2019nun	DG19tvtnc	00:56:48.599 −24:54:30.48	8/18 06:17:16	$i = 21.7$	GROWTH	0.131	25393	Spec.Host-z *
AT2019nuq	DG19kxdnc	01:32:36.497 −33:55:01.88	8/17 07:50:52	$z = 20.5$	GROWTH	0.104	25393	Spec.Host-z
AT2019nuw	PS19epz	00:50:26.340 −25:52:57.83	8/18 12:59:02	$z = 21.9$	PS1	?	25417	SN?*
AT2019nux	PS19eqa	00:50:21.019 −23:42:46.79	8/18 12:59:02	$z = 21.8$	PS1	?	25417	SN?*
AT2019nuy	PS19eqb	00:50:50.397 −25:29:29.55	8/18 12:59:02	$z = 21.1$	PS1	?	–	?*
AT2019nuz	PS19eqc	00:49:52.264 −25:31:25.62	8/18 12:59:02	$z = 21.9$	PS1	?	25417	SN?*
AT2019nva	PS19eqd, VSTJ005243.34-233753.6	00:52:43.395 −23:37:54.01	8/18 12:59:02	$z = 21.5$	PS1	?	25417	SN?*
AT2019nvb	PS19eqe	00:46:51.168 −25:25:39.31	8/18 12:59:02	$z = 21.7$	PS1	0.0008	25417	Spec.Host-z*
AT2019nvc	PS19eqf	00:52:18.326 −26:19:42.07	8/18 13:01:55	$z = 21.3$	PS1	0.07	25417	**SN?**
AT2019nvd	PS19eqg, VSTJ005542.30-244149.9	00:55:42.309 −24:41:50.28	8/18 12:59:02	$z = 21.5$	PS1	?	25417	SN?*
AT2019nve	PS19eqh, VSTJ005605.55-243826.4	00:56:05.510 −24:38:26.40	8/18 12:59:02	$z = 21.3$	PS1	?	25417,25669	SN?*
AT2019nvr	PS19eqo	00:48:16.088 −25:28:14.99	8/18 12:56:09	$z = 20.9$	PS1	?	25417	SN?*
AT2019nvs	PS19eqp	00:52:37.759 −26:11:41.40	8/18 13:10:33	$z = 21.4$	PS1	?	25417	SN?*
AT2019nxd	desgw-190814i	00:42:44.598 −24:57:20.34	8/17 04:52:19	$i = 21.8$	DESGW	1.3	25486	Phot.Host-z
AT2019nxe	desgw-190814j, VSTJ004616.81-242221.2	00:46:16.814 −24:22:21.19	8/16 07:29:16	$z = 22.1$	DESGW	0.0777	25425,25543	SN
AT2019nys	desgw-190814k, VSTJ005756.90-243400.5	00:57:56.903 −24:34:00.56	8/16 05:55:40	$i = 21.8$	DESGW	0.4	25486	Phot.Host-z*

Table C.1. continued.

IAU name	Survey name	Coordinates	Discovery date	Mag	Source	z	GCNs	Comments
AT2019nyv	DG19mulnc, VSTJ004659.45-230559.5	00:46:59.451 −23:05:59.50	8/18 06:01:26	$z = 20.6$	GROWTH		25669	Pre.Det.
AT2019nyy [(a)]	DG19zoonc	00:48:16.652 −26:38:26.97	8/18 06:08:38	$z = 21.1$	GROWTH	?	Andreoni et al. (2020)	Andreoni
AT2019nzd	DG19kzvqc, VSTJ005806.46-245014.3	00:58:06.435 −24:50:14.35	8/21 04:35:02	$i = 22.2$	GROWTH	?	25486	?*
AT2019nzr	desgw-190814m	00:47:21.410 −24:34:36.58	8/16 05:36:57	$i = 21.8$	DESGW	?	25425,25486	?*
AT2019oab	desgw-190814o	00:58:59.398 −25:46:12.66	8/16 08:18:14	$z = 21.7$	DESGW	0.5	25425,25486	Phot.Host-z*
AT2019oac	DG19zujoc	00:53:02.879 −21:39:04.57	8/18 06:43:12	$z = 21.4$	GROWTH	?	25486	SN?*
AT2019obc	desgw-190814q	00:58:16.023 −24:08:23.18	8/18 06:17:16	$i = 21.7$	DESGW	0.22	25438,25543	SN
AT2019odc	desgw-190814r	00:46:01.689 −25:27:32.94	8/17 04:52:19	$i = 21.6$	DESGW	0.0540	25486,25588	?*
AT2019oer	CFHT_cand, desgw-190814s	00:47:28.027 −25:26:14.15	8/18	$i = 22.9$	CFHT	?	25443,25447	Pre.Det.
AT2019ofb	PS19erd	00:55:19.237 −26:11:50.77	8/21 13:00:28	$z = 21.4$	PS1		25455	?
AT2019okr	desgw-190814t	00:47:23.696 −25:27:30.78	8/17 05:06:43	$z = 22.7$	DESGW	?	25486,25526	Pre.Det.*
AT2019oks	desgw-190814u	01:02:08.319 −24:54:21.70	8/17 05:47:02	$i = 22.8$	DESGW	0.193?	25486	Spec.Host-z?*
AT2019omt	desgw-190814v	00:59:26.742 −25:59:41.28	8/18 06:25:55	$z = 22.4$	DESGW	0.1564	25486,25588	SN
AT2019omu	desgw-190814w	01:33:58.890 −34:20:20.01	8/16 06:37:26	$i = 21.3$	DESGW	0.7	25486	Phot.Host-z*
AT2019omv	desgw-190814x	01:39:54.812 −33:23:01.39	8/16 06:38:52	$z = 22.0$	DESGW	0.4	25486	Phot.Host-z
AT2019omw	desgw-190814y	00:48:56.255 −23:10:12.49	8/18 06:01:26	$z = 22.6$	DESGW	?	25486	SN?*
AT2019omx	desgw-190814z	01:36:44.246 −33:18:09.64	8/16 07:13:26	$i = 22.6$	DESGW	0.275	25486,25540	Spec.Host-z
AT2019onj	desgw-190814ab	00:47:26.006 −25:26:55.13	8/17 04:55:12	$z = 21.7$	DESGW	?	25486,25526	Pre.Det.*
AT2019opp	desgw-190814ac	00:57:38.254 −25:16:45.00	8/17 05:48:28	$z = 22.5$	DESGW	?	25486	SN?*
AT2019osy	ASKAP 005547-270433	00:55:47.000 −27:04:33.00	8/23 13:44:59	$i = 22.3$	ASKAP	–	25488,25801, 25487	AGN?*
AT2019paw [(a)]	DG19ggesc	00:48:34.270 −25:05:25.81	8/21 06:00:00	$i = 22.2$	GROWTH	?	Andreoni et al. (2020)	Andreoni
AT2019qbu	VSTJ005109.17-221740.7	00:51:09.173 −22:17:40.69	8/20 03:47:38	$r = 21.1$	GRAWITA	?	–	Non.det.*
AT2019qby	VSTJ004414.33-250744.3	00:44:14.334 −25:07:44.32	8/16 06:36:00	$r = 21.4$	GRAWITA	?	–	SN?*
AT2019qbz	VSTJ005653.99-275921.4	00:56:53.980 −27:59:21.37	8/16 07:10:33	$r = 20.9$	GRAWITA	?		SN?*
AT2019qca	VSTJ004548.54-264939.0	00:45:48.540 −26:49:39.01	8/22 04:01:55	$r = 21.8$	GRAWITA	?	–	SN?*
AT2019qcb	VSTJ004619.06-260843.2, PS19gaz	00:46:19.038 −26:08:43.61	8/16 05:31:12	$r = 21.6$	GRAWITA	?	–	SN?*
AT2019qcc	VSTJ005349.82-244549.6, PS19gba	00:53:49.844 −24:45:49.40	8/20 04:16:19	$r = 22.0$	GRAWITA	?	–	SN?*
AT2019thm [(a)]	DG19gyvx	00:47:56.625 −26:54:02.80	8/15 07:00:28	?	GROWTH	?	Andreoni et al. (2020)	Andreoni
AT2019tih [(a)]	DG19ilqnc	00:47:26.675 −27:36:02.82	8/18 06:05:45	$i = 21.3$	GROWTH	?	Andreoni et al. (2020)	Andreoni
AT2019tii [(a)]	DG19tedsc	00:49:35.203 −27:02:09.33	8/21 05:52:48	$i = 21.9$	GROWTH	?	Andreoni et al. (2020)	Andreoni
AT2019tix [(a)]	PS19gjp, DG19bown	00:48:45.660 −24:38:50.56	8/21 04:11:51	$i = 22.9$	GROWTH	?	Andreoni et al. (2020)	Andreoni
AT2019aacd	CFHT0054-2456zau	00:54:11.280 −24:56:17.66	8/18 12:39:22	$i = 20.8$	CFHT	?	Vieira et al. (2020)	Bogus?*

Appendix D: Author contributions

In what follows, we describe briefly the individual contribution of each author, in alphabetical order.

KA contributed to GOTO candidate vetting. LA contributed to data interpretation and discussion. CB produced the kilonova light curve tables used to put limits on the progenitor binary properties. FEB helped with the interpretation and contributed to the manuscript. SB served on the on-call operations team triggering VLT observations and is the EFOSC2 Instrument Scientist. MGB coordinated the working group that interfaces with external facilities. KB contributed to HST follow-up observations. MTB obtained difference images and magnitude limits for the targeted galaxy search. MBr contributed to governance as a member of the ENGRAVE Governing Council (GC), provided comments on the manuscript and contributed to editing the manuscript. EB contributed to governance as a GC member. SHB served on the on-call operations team triggering VLT observations. MBu contributed to modelling discussions and provided comments on the manuscript. SCh contributed with comments on the manuscript. EC contributed to the VST transient search and galaxy targeted search. AJCT used complementary data to study many galaxies inside the 90% probability contour. KCC co-leads the Pan-STARRS science surveys. SCa provided comments on the manuscript. TWC is the PI of the GROND GW project, provided GROND images and served on the on-call operations team. RCi contributed to theoretical modelling and interpretation. AC served on the on-call operations team triggering VLT observations, is the contact person for INTEGRAL and neutrino telescopes and provided comments on the manuscript. CMC obtained and reduced the data obtained with the Liverpool Telescope. SCo contributed to governance as an Executive Committee (EC) member and supervised the development of the manuscript. RCu collected, mined, and analysed the GOTO data. FDA provided comments on the manuscript. PDA contributed to governance as a GC member, served on the on-call operations team and obtained and reduced TNG images. GDC is a member of the infrastructure and outreach working groups. MDV provided comments on the manuscript. LD co-leads the ATLAS science surveys. MDP provided comments on and edited the manuscript. VD served on the on-call operations and writing teams and provided comments on the manuscript. VSD is a core member of the GOTO collaboration. MJD is a member of the GOTO operations team and assisted with the GOTO contribution. NER searched for transients with the VST. PAE contributed to infrastructure and provided an interface to the *Neil Gehrels Swift* Observatory team. RAJEF served on the on-call operations team triggering VLT observations. AF served on the on-call operations and writing teams. MF was the event advocate for S190814bv and contributed to obtaining observations, analysis, and paper writing. ASF led HST follow-up of AT2019osy. JPUF served on the on-call operations team. LG served on the on-call operations team triggering VLT observations and provided comments on the manuscript. CG served on the on-call operations team. DKG is a PI of the GOTO project and contributed to the observations and data analysis. FG has contributed to reduction and calibration of VST images. GGh contributed to Sect. 4. JHG served on the on-call operations team. AGo commented on the manuscript. BPG is a member of the GOTO team, and provided the AT2017gfo model fits, analysis comparing them to S190814bv (Sect. 4.1), and Figs. 9 and 10. CGF managed the rapid reduction pipeline for the VISTA imaging. SGG served on the on-call operations team triggering VLT observations and EPO team. AGr was the GRAWITA contact person and PI and image reducer of VST data. GGr provided Fig. 1 and the VST coverage. MG contributed to HAWK-I observations. PJG coordinated observations with MeerLICHT and contributed to the manuscript. CPG served on the on-call operations team. TH contributed to GOTO candidate vetting. KEH contributed to the observations, data analysis and manuscript editing. JH contributed to governance as a GC member, served on the on-call operations team and contributed to editing the manuscript. YDH used complementary data to study many galaxies inside the 90% probability contour. MEH manages and leads the Pan-STARRS data reductions. CI is FORS2 instrument scientist and provided comments on the manuscript. LI served on the on-call operations team triggering VLT observations and contributed to the observation strategy. JJ served on the on-call operations team triggering VLT observations and contributed to data reduction. AJ contributed to discussion and analysis. ZPJ served on the on-call operations team triggering VLT observations and contributed to discussions and analysis. PGJ contributed to governance as a GC member and is the PI and a coordinator and observer of the WHT. EK contributed to the reduction and analysis of the HAWK-I data. DAK created the GCN BibTeX entries, performed the study comparison in Sect. 4.3, and wrote part of the introduction. SKi contributed with data analysis of a candidate counterpart. SKl was involved in the GROND data reduction and analysis. ECK carried out image subtraction of HAWK-I and TNG data and served on the on-call operations team triggering VLT observations. MK contributed to GOTO candidate vetting. RK provided comments on the manuscript and served on the on-call operations and writing teams. HK reduced FORS2 imaging data. GPL contributed the GRB prompt and afterglow emission theory, modelling, text and a figure. GL scanned FORS2 images and coordinated the polarimetry working group. AJL contributed to management as the chair of the EC, coordinated observations with VLT/WHT and contributed to analysis and writing. FL is a member of the EPO working group. TBL carried out observations with Pan-STARRS. JDL served on the on-call operations team and enacted GOTO observations. EMag manages and leads the Pan-STARRS data reductions. KM contributed to management as an EC member, served on the on-call operations team, coordinated part of the VLT observations, contributed to data reduction and analysis, and provided comments on the manuscript. EMai contributed observations within the GRAWITA context. IM contributed to astrophysical modelling and interpretation. MM contributed to paper writing and host galaxy interpretation. SMa contributed to the analysis of HAWK-I data. ORMB provided limiting magnitudes of ATLAS and PS1 observations and the table of PS1 counterparts. AM is a member of the imaging working group and contributed to observations and data reduction. MJM performed SED fitting and contributed to interpretation of ALMA results. BMJ worked on infrastructure, data (notably VISTA) and analysis. SMo was an observer at the WHT and served on the on-call operations team. LNi contributed to VST and TNG data management and analysis. MN served on the on-call operations team. ANG performed GROND data reduction and analysis. LNu is a core member of the GOTO collaboration. PTOB contributed to GOTO discussion and interpretation. SRO served on the on-call operations team. FO served on the on-call operations team. EPa contributed follow-up observations with VST and TNG. BP contributed to the activities of the working group that interfaces with external facilities (LVC). PA contributed to the development of the NS–BH kilonova model and provided text for the manuscript. DAP contributed to gathering and analysis of Liverpool Telescope observations. EPi

contributed to governance as a GC member provided comments on the manuscript. GP served on the on-call operations team. SPi is a member of the spectroscopy team and coordinator of the EPO working group. SPo is a core member of the GOTO collaboration. AP provided comments on the manuscript. MAPT contributed WHT observations. MLP provided comments on the manuscript. JQV provided comments on the manuscript. FR contributed obtaining limiting magnitudes of difference images. GR contributed to the GOTO observations. ARa is the PI of the GROND ToO time project. ARe provided Pan-STARRS and ATLAS science analysis. TMR contributed to the reduction and analysis of the HAWK-I data. SSR created and ran the subtraction pipeline for the VISTA imaging. ARo contributed to follow-up with TNG and VST. SR contributed to editing the introduction and Sect. 4.1. NBS contributed to FORS and HAWK-I observations and data reduction and served on the on-call operations team triggering VLT observations. ASC served on the on-call operations team triggering VLT observations. OSS developed and implemented the framework for the comparison of observational limits and theoretical models, led the writing of Sects. 3.7, 4, and Appendix A, produced Figs. 7, 8, 11–14 and B.1, and compiled Tables B.1 and B.2. LSa contributed the ranked galaxy lists from the HOGWARTs algorithm and web application. RS discussed the results and commented on the manuscript. SS provided comments on the manuscript. LSb contributed to the design of X-shooter observations. PScha was a member of the writing team on-call for this event and contributed to editing the manuscript. PSchi is the VST PI and provided guaranteed time VST observations. ASBS carried out observations with Pan-STARRS. TS is a GROND team member and reduced GROND images. SJS contributed to governance as the chair of the GC, co-leads the Pan-STARRS and ATLAS surveys, and contributed manuscript text. MS served on the on-call operations team. KWS developed and ran the Pan-STARRS and ATLAS transient science servers at QUB. JS contributed to governance as a GC member and provided comments on the manuscript. SS helped compile the table of PS1 candidates. ERS contributed as a member of the GOTO team. RLCS was a member of the writing team. DS contributed to governance as a GC member, is the GOTO PI & liason, was the WHT UK PI, contributed data analysis and provided content. GS served on the on-call writing team. CWS provided Pan-STARRS and ATLAS science analysis. NRT is PI of VINROUGE and contributed to governance as a GC member, contributed to VISTA analysis and paper writing. VT contributed to data analysis. JLT co-leads the ATLAS science surveys. MT served on the on-call operations triggering VLT observations and writing teams. KU processed GOTO data – image stacking and photometric calibration. AJvdH provided comments on the manuscript. SDV contributed to management as an EC member, served on the on-call operations team, and coordinated part of the VLT observations. NAW provided comments on the manuscript. DW served on the writing team on-call for this event, on the on-call operations team and contributed to the interpretation of the data. KWie served on the on-call operations team. KWii developed and maintained the computing environment and software for the imaging working group. LW served on the on-call operations team. SY contributed to transient detection in VST data. SXY provided comments on the manuscript. DRY built and helps manage much of the ENGRAVE communication infrastructure.